

# **ORDERING AND ELECTRODEPOSITION AT THE ALKANETHIOL/AU(111) INTERFACE**

THÈSE N° 1729 (1997)

PRÉSENTÉE AU DÉPARTEMENT DE PHYSIQUE

ÉCOLE POLYTECHNIQUE FÉDÉRALE DE LAUSANNE

POUR L'OBTENTION DU GRADE DE DOCTEUR ÈS SCIENCES

PAR

**Ornella CAVALLERI**

Laurea di Dottore in Fisica, Università degli Studi di Genova, Italie  
de nationalité italienne

acceptée sur proposition du jury:

Prof. K. Kern, directeur de thèse  
Dr H.A. Biebuyck, corapporteur  
Prof. A. Gilozzi, corapporteur  
Prof. H. Vogel, corapporteur

Lausanne, EPFL  
1997

## Version abrégée

A l'aide d'un microscope à effet tunnel (STM) à température variable, nous avons étudié les processus de réarrangement à l'interface alcanethiol/Au(111) ainsi que l'électrodéposition de cuivre à cette même interface.

A l'échelle mésoscopique la chimisorption de la monocouche d'alcanethiols sur la surface d'Au(111) est accompagnée par la formation de dépressions ayant une largeur de quelques nanomètres et une profondeur d'une monocouche d'or. Ces dépressions, distribuées au hasard sur la surface, sont en fait des îlots de lacunes dans la couche supérieure du substrat d'or. Leur origine est liée à des processus d'érosion chimique et de réarrangement de la surface d'or qui ont lieu pendant la formation de la monocouche.

A l'échelle microscopique les alcanethiols forment une monocouche dense avec une structure  $(\sqrt{3}\times\sqrt{3})R30^\circ$  sur l'Au(111). La monocouche présente des domaines de molécules ordonnés d'une taille de 10 à 20 nm. L'ordre moléculaire dépend de la longueur de chaîne des thiols ainsi que du traitement thermique subi par l'échantillon. Dans le cas de monocouches formées par des thiols à chaîne longue, le STM montre la coexistence de différents types de superstructures moléculaires dues aux différentes orientations des squelettes

de carbone. Les monocouches formées par des thiols courts présentent de plus une structure rayée qui correspond à une phase moins dense. Les monocouches formées par des thiols longs subissent, après recuit à 370 K, une transition vers la structure rayée.

Après avoir caractérisé la structure de l'interface alcanethiol/Au(111) à température ambiante, nous avons étudié sa stabilité thermique par des mesures STM à haute température (jusqu'à 390 K) qui nous ont permis de suivre in-situ les processus de réorganisation ayant lieu à l'interface pendant le recuit. L'augmentation de la taille moyenne des dépressions (bien décrite par un mécanisme de "Ostwald ripening") suivie par des processus de coalescence et d'annihilation aux marches des terrasses de la surface d'or conduit à la disparition des dépressions. A l'échelle moléculaire, cette réorganisation produit une augmentation de la taille moyenne des domaines ordonnés jusqu'à 50-60 nm. Un recuit ultérieur provoque la désorption des thiols.

Dans une deuxième étape, nous avons exploité les connaissances obtenues sur la structure moléculaire et la stabilité thermique de ces monocouches pour préparer des électrodes recouvertes par des monocouches de thiols, que nous avons ensuite utilisées comme substrats pour étudier l'électrodéposition de cuivre. Des mesures de voltampérométrie cyclique ainsi qu'une étude in-situ par STM électrochimique ont montré que la couche organique a une profonde influence sur le processus d'électrodéposition et permet en fait de contrôler le mécanisme de croissance du cuivre. En variant la longueur de chaîne des thiols ainsi que le potentiel de l'électrode et la température, nous avons pu produire des îlots de cuivre bidimensionnels, des agrégats tridimensionnels ou obtenir une croissance du cuivre couche par couche.

# Abstract

Ordering phenomena and copper electrodeposition at the alkanethiol/Au(111) interface have been investigated in-situ by variable temperature Scanning Tunneling Microscopy (STM).

On the mesoscopic scale the chemisorption of the alkanethiol monolayer on the Au(111) surface is accompanied by the formation of pits a few nanometers in size, one monoatomic gold layer in depth, randomly distributed on the surface. These depressions are found to be vacancy islands in the topmost layer of the gold substrate. Chemical etching and restructuring of the gold surface are the mechanisms involved in the pit formation.

On the microscopic scale alkanethiols are densely packed and form a  $(\sqrt{3} \times \sqrt{3})R30^\circ$  adlattice on Au(111). Ordered molecular domains, 10-20 nm in size, characterize the alkanethiol monolayers. The molecular order is found to depend on the thiol chain length as well as on the thermal treatment. In the long chain monolayers, STM reveals the coexistence of different kinds of molecular superlattices resulting from the orientational order of the carbon backbones. Short chain monolayers present an additional striped structure due

to a less dense molecular packing. Upon heating above 370 K, long chain monolayers show a transition to the striped structure.

Isothermal STM measurements at elevated temperatures (up to 390 K) allowed to study the thermal behavior of the alkanethiol/gold interface in-situ. Annealing the samples induces a reorganization at the interface. Hole coarsening (well described by an Ostwald ripening mechanism) followed by coalescence and annihilation of pits at gold steps is the way to the healing of the vacancy islands. On the molecular scale, this reorganization process results in the increase of the ordered domain size up to 50-60 nm. Upon further heating, the thiol desorption sets in.

In a second step, the information gained about the molecular structure and the thermal behavior of these monolayers has been exploited to prepare well defined, thiol modified gold electrodes. Cyclic voltammetry and in-situ electrochemical STM have been used to characterize the electrochemical deposition of Cu on the alkanethiol/Au(111) surface. The organic layer has a profound influence of the electrodeposition process and allows to control the Cu growth mode. By varying the thiol chain length, as well as the electrode potential and the temperature, it is possible to deposit 2D islands, 3D clusters or induce a layer-by-layer copper growth.

# Table of contents

<b>1</b>	<b>Introduction</b>	<b>1</b>
1.1	Self-assembled monolayers . . . . .	4
1.2	The electrode/electrolyte interface . . . . .	8
<b>2</b>	<b>Experimental</b>	<b>15</b>
<b>3</b>	<b>The alkanethiol/Au(111) interface</b>	<b>25</b>
3.1	Introduction . . . . .	25
3.2	The “holes” at the alkanethiol/Au(111) surface . . . . .	26
3.3	Molecular order at the alkanethiol/Au(111) interface . . . . .	35
3.4	Conclusions . . . . .	55
<b>4</b>	<b>Thermal mass transport at the alkanethiol/Au(111) interface</b>	<b>57</b>
4.1	Introduction . . . . .	57
4.2	Initial stage of the annealing: the Ostwald ripening mechanism . . . . .	58
4.3	Final stage of the annealing: coalescence and annihilation . . . . .	69
4.4	Towards desorption . . . . .	71
4.5	Conclusions . . . . .	73

<b>5</b>	<b>Cu electrodeposition on alkanethiol-covered Au(111) electrodes</b>	<b>75</b>
5.1	Introduction . . . . .	75
5.2	Thin film growth: thermodynamics vs. kinetics . . . . .	77
5.3	Cu electrodeposition on Au(111) . . . . .	81
5.4	Cu electrodeposition on alkanethiol/Au(111) in the underpotential regime . . . . .	89
5.5	Cu electrodeposition on alkanethiol/Au(111) in the overpotential regime . . . . .	97
5.6	Cu electrodeposition at elevated temperature . . . . .	105
5.7	Anodic Cu dissolution . . . . .	112
5.8	Mechanistic and structural models . . . . .	113
5.9	Conclusions . . . . .	120
<b>6</b>	<b>Conclusion and outlook</b>	<b>121</b>
	<b>Bibliography</b>	<b>123</b>

# Chapter 1

## Introduction

Surface science studies are usually associated with ultra high vacuum (UHV) conditions. Working in UHV environment provides the possibility to prepare and study clean, well characterized systems. From this point of view, another environment which presents some similarities to UHV is the electrochemical one. By the choice of proper experimental conditions (pure electrolytes and careful preparation and transfer of the sample into the electrolyte) impurity free surfaces can be prepared in the electrochemical environment: the liquid phase represents a good protection against the adsorption of atmospheric contaminants. A substantial difference exists, however, between the UHV and the electrochemical environment: it concerns their complexity. UHV systems are highly simplified model systems. Their relative "simplicity" facilitates the study of the fundamental processes occurring at a surface, but at the same time confines them rather far away from reality. When the solid/vacuum interface is replaced by the solid/liquid interface, the complexity of the system increases substantially. The relatively simple scenario of isolated atoms impinging, diffusing and reacting on a clean, well defined surface evolves into the much



more "crowded" world of solvent molecules in Brownian motion, neutral molecules adsorbing on the surface, hydrated ions migrating and diffusing towards the surface together with coadsorbing counterions. Despite this increased complexity, the electrochemical environment offers the possibility to control the behavior of the system by changing some external parameters. Similar to temperature and flux in molecular beam epitaxy in UHV, electrode potential, electrolyte additives and, to some extent, temperature can be varied to control surface processes under electrolyte. Obviously, the increased complexity renders the study of these events more difficult. However, even if more complex to investigate, the solid/liquid interface is the object of an increasing interest as the understanding of the processes occurring at this interface is of relevance for many real systems and applications, ranging from biology to industrial chemistry. Examples include cell membranes in physiological environment which are a special kind of solid/liquid interface regulating all the functions of living beings. From the technological point of view, corrosion and electroplating are two examples of processes in which the solid/liquid interface plays a crucial role.

The subject of this thesis shares some aspects with the above-mentioned processes even if the work was not aimed at technological applications, but mainly addressed to the understanding of the microscopic mechanisms governing the solid/liquid interface.

The first part of the work deals with the study of the modification of the structure and properties of crystalline metal surfaces induced by self-assembly of organic monolayers from a solution. Self-assembled monolayers (SAMs) [Ulm91A] are the object of an increasing interest in different research fields. They can be used to prepare model systems for fundamental studies dealing with structure and properties of biological membranes [Pla93] or to prepare functionalized organic surfaces bearing selective binding sites for biosensor

design [Dus94, Spi93]. Among the other applications, SAMs can be advantageously used to ensure protection against oxidation [Lai92] and corrosion [YLi95]. In the second part of this work, the knowledge gained about the structure of these coated metal surfaces is exploited to control the mechanism of the metal electrodeposition on such special electrodes.

Scanning Tunneling Microscopy (STM) has been used to obtain a direct microscopic real space view of the structural modifications accompanying the mentioned processes. The experimental details of the study, especially concerning the STM setup, are presented in chapter 2.

The self-assembled monolayers studied in this work are alkanethiol monolayers on Au(111). The modification of the morphology of the gold surface due to the thiol chemisorption as well as the details of the molecular order of these monolayers, and the dependence of the order on the alkyl chain length, are discussed in chapter 3.

Having analyzed the molecular structure of these organic films, the attention is focused on their thermal stability. Chapter 4 describes the results of an in-situ STM investigation of the reorganization processes occurring at the thiol/gold interface during thermal annealing.

The results concerning the molecular structure and the thermal behavior of the thiol/gold interface have then been exploited to prepare well characterized, thiol-covered gold electrodes. In chapter 5, the electrodeposition of copper on these electrodes is described and compared to the deposition on bare gold. It will be shown how, in the presence of the organic layer, the growth mode of the electrodeposited copper can be manipulated and varied from a three-dimensional to a layer-by-layer mechanism by controlling the thiol chain length, the electrode potential and the temperature.

In the following, some basic concepts about the SAMs and the electrode/electrolyte interface, which are important to understand the motivations behind the experiments as well as to interpret their results, will be reviewed.

## 1.1 Self-assembled monolayers

The formation of monolayers by self-assembly of organic molecules at surfaces is just one example of a wide class of self-assembly phenomena, including the aggregation of amphiphilic molecules into micelles and bilayers, up to the assembling of biological membranes. SAMs represent a relatively simple case which can be used as a model system in order to gain a fundamental understanding of the self-organization as well as of the structure/properties relationship of these systems. The possibility to tailor both the head and tail group of the adsorbing molecules allows one to investigate the competing intermolecular, molecule/substrate and molecule/solvent interactions which control the formation, structure and properties of such systems. Moreover, the possibility to control macroscopic surface properties, like wetting, adhesion, lubrication or corrosion, by the modification of the chain end-group makes these layers interesting also from the point of view of applied physics and chemistry.

The peculiar feature of SAMs is the strong and specific bonding between one part of the adsorbing molecule, the head group, and the substrate. It is this strong and selective interaction that is at the basis of the self-assembly process. By the proper choice of the surface and of the molecule head group different kinds of SAMs can be prepared. SAM formation includes the adsorption of alkanolic acids on metal oxides, of organosilicon derivatives on hydroxylated surfaces and of sulfur-bearing molecules on gold, silver, platinum or copper.

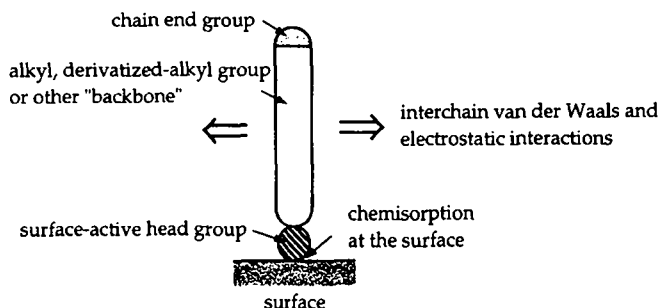


Fig. 1.1. Schematic view of a self-assembling molecule.

As shown in Fig. 1.1, in a self-assembling molecule one can distinguish three parts which give complementary contributions to the monolayer structure: the surface-active head group, which is responsible for the molecule/substrate interaction, the alkyl or alkyl-derivatized chain or other (e.g. aromatic) "backbones" and the end group.

In the case of alkanethiol ( $\text{CH}_3(\text{CH}_2)_{n-1}\text{SH}$ ) monolayers on gold, a strong bond, which has a strength of  $\sim 180$  kJ/mol [Dub92], forms between sulfur and gold. The results of different spectroscopic studies, like X-ray photoelectron spectroscopy investigations [Bai89A, Lai91, Nuz87] and surface Raman spectroscopy measurements [Bry91], led to the conclusion that the thiol chemisorption occurs via the formation of a gold thiolate species (with the cleavage of the S - H bond).

The second part of the molecule is the alkyl chain. Van der Waals interactions are the main interchain forces in the case of simple alkyl chains. In the case of more complex molecules with a polar or charged group substituted in the chain, dipole or long-range electrostatic forces play a role in the interchain interactions. In thiol monolayers, at least in the case of simple molecules without bulky groups, molecules are usually ordered in a closely packed

arrangement with the chains in a nearly *all-trans* conformation. When the intermolecular distance imposed by the surface/head group interaction is larger than the van der Waals diameter of the chains, molecules can assemble with their axes tilted with respect to the normal to the substrate in order to maximize interchain interactions. In the case of alkanethiols on Au(111), a tilt of about 30° was found in experimental as well as theoretical studies.

Finally, the third part of the molecule is the chain terminal group. The strong Au/S interaction often allows to vary the end group without problems of competing effects in the chemisorption between sulfur/gold and chain end group/gold. The chain terminal functionality dominates the interactions between the monolayer and a contacting phase and determines macroscopic surface properties like wettability or lubrication. The most widely studied chains are those terminated by CH<sub>3</sub> groups which produce hydrophobic surfaces, but monolayers with, e.g., OH, COOH, CONH<sub>2</sub>, CN or pyrrole containing end groups up to more complex functionalities like ferrocene or ruthenium redox couples and metalloporphyrins have been prepared and investigated [Chi91A, Fin92, Lee94, Nuz90A, Wil95, Zak93]. It is indeed the possibility to prepare monolayers with very specific chemical reactivity and surface properties which is at the basis of the current interest in this research field.

An interesting characteristic of SAM thiol monolayers is their ease of preparation. The first and most widely used preparation method is schematically represented in Fig. 1.2. The metal substrate is immersed in a solution of thiol molecules, usually in ethanol, for a period which can vary from some seconds up to a few days. It must be noted that the transfer of a "clean" metal surface into solution is restricted to a very few (noble) metals, when one wants to avoid the complexity of a vacuum preparation followed by transfer through controlled atmosphere.

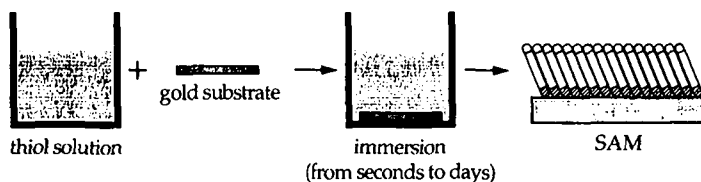


Fig. 1.2 Schematic representation of the “dipping technique” for the deposition of thiol SAMs from solution.

After some hours of immersion a high density, well ordered monolayer is formed. Studies of the adsorption kinetics of alkanethiols on gold from a solution [Bai89A, Buc91, Häh93, Kar94] have shown that, at least at relatively dilute solutions ( $10^{-3}$  M), two distinct adsorption kinetics characterize the monolayer formation. A very fast step, taking from a few seconds up to several minutes (depending on the thiol concentration) and resulting in an imperfect monolayer with a thickness which is about 80-90% of the final one and with contact angles approaching their limiting values, is followed by a slow step which lasts several hours, at the end of which the thickness and the contact angles reach their final values. The rapid step, which can be well described by a Langmuir adsorption isotherm, is mainly governed by the head group/gold interaction. The second step, which can be thought of as a surface crystallization process involving expulsion of contaminants and/or solvent from the monolayer, additional thiol adsorption and ordering of the initially entangled alkyl chains, mainly results from the different interchain interactions.

A second method to prepare thiol SAMs, which needs a more sophisticated experimental setup when compared to the “beaker approach” shown in Fig. 1.2, is the gas phase dosing in UHV. Vapor phase deposition allows an easier control of the deposition rate with respect to the dipping technique,

which has been advantageously exploited to investigate the very initial stage of the chemisorption [Poi96]. As discussed in chapter 3, monolayers characterized by lower density structures with larger tilt of the molecular axis, when compared to solution prepared SAMs, can be obtained.

An interesting alternative to the deposition from solution or gas dosing in vacuum has recently been proposed, based on a microcontact printing technique [Lar97]. An elastomeric stamp inked with a thiol solution is used to deliver molecules on the surface. Varying the concentration of the thiol solution allows to control the SAM structure from very low density, disordered monolayers up to high density, well ordered monolayers.

## 1.2 The electrode/electrolyte interface

In this paragraph some general concepts concerning the electrode/electrolyte interface are presented. In the first part, the “simple” case of the interface between a bare metal electrode and the electrolyte is discussed. In the second part, the analysis is extended to the case of an electrode covered by an organic layer: similarities and difference with respect to the first case will be discussed.

When an electrode and an electrolyte solution come into contact, a segregation of positive and negative charges develops in a direction normal to the phase boundary. The charge separation can result from the adsorption of positive or negative ions at the surface, from the transfer of charge across the interface, from the reorientation of dipolar molecules or the deformation of polarisable molecules by the asymmetrical force field at the interface.

A schematic representation of an electrified solid-liquid interface is shown in Fig. 1.3a. The interface can be divided into three regions: a metal layer, an inner

layer and a diffuse layer. The space charge region inside the metal electrode is a very narrow layer, at most a few angstroms thick, adjacent to the solution.

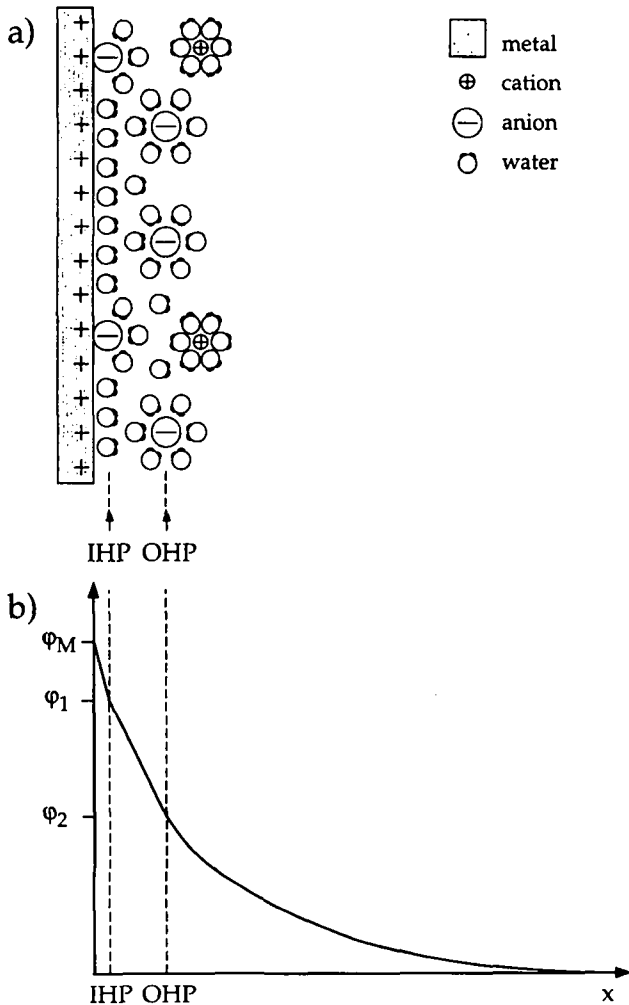


Fig. 1.3 Schematic models of the ion (a) and potential (b) distribution across the metal/electrolyte interface in the case of specific adsorption.



The inner layer contains solvent molecules and, in some cases, neutral molecules or specifically adsorbed ions. Specifically adsorbed ions are considered to be unsolvated or solvated only on the side pointing away from the metal. Actually, even if the mechanism for specific adsorption is not completely clarified, the occurrence of this phenomenon is related to the free energy change accompanying the loss of the hydration shell: larger ions, which are less strongly hydrated, undergo specific adsorption more easily [Boc70]. The centers of the specifically adsorbed ions define the position of the Inner Helmholtz Plane (IHP). The Outer Helmholtz Plane (OHP) is defined by the plane of closest approach of non-specifically adsorbed (hydrated) ions. The diffuse layer occupies the region between the OHP and the bulk of the solution. The properties of this layer can be explained in terms of an equilibrium between thermal motion and the long range electrostatic interaction of the ions with the charged electrode. The potential profile corresponding to this model representation of a charged interface is shown in Fig. 1.3b. Moving from the electrode surface towards the electrolyte, a linear potential decrease is observed between the metal surface and the OHP. If specific adsorption occurs, this region can be separated into two parts, the layer between the electrode surface and the IHP and the region between the IHP and the OHP. Both regions are characterized by a linear potential drop, but the slopes are in general different. Outside the OHP, the potential decays exponentially through the diffuse layer to the bulk value as described by the Gouy-Chapman model:  $\phi_x = \phi_2 e^{-k(x-x_2)}$ , where  $x$  indicates the distance from the electrode surface,  $\phi_2$  is the potential at the OHP,  $x_2$  indicates the position of the OHP and  $k$  is a constant proportional to the square root of the solution concentration. This means that the higher the concentration, the faster is the potential decay in the diffuse layer, i.e. the more compressed is the diffuse layer.

The modification of the interfacial structure by the deposition of an organic layer on the metal electrode requires some revisions of the picture in Fig. 1.3. The study of electrode/electrolyte interfaces in the presence of deposited organic layers is a relatively new subject compared to the bare metal/liquid

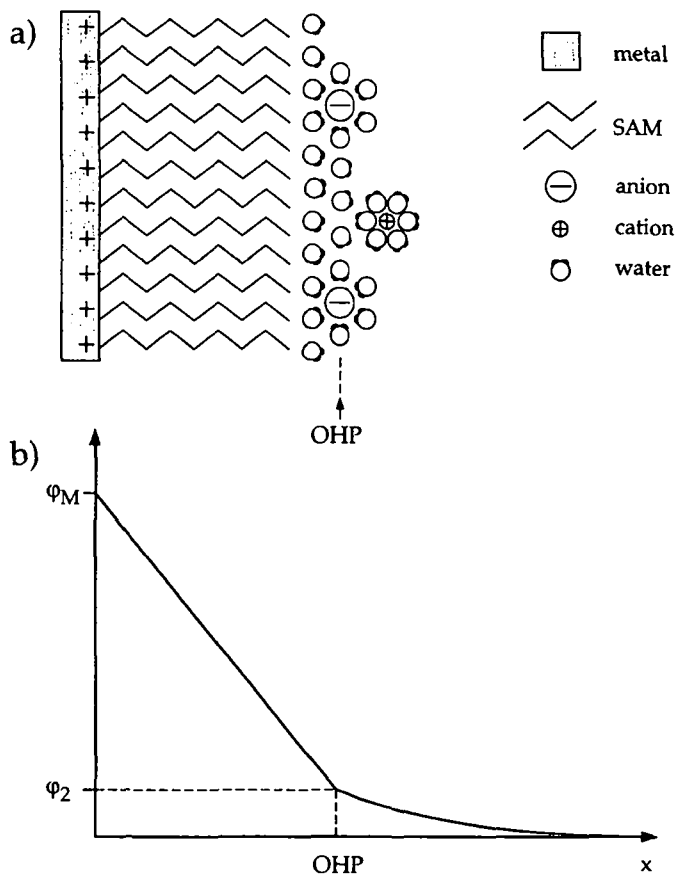


Fig. 1.4 Schematic models of the ion (a) and potential (b) distribution across the metal/SAM/electrolyte interface.

interface whose investigations date back to the studies of Helmholtz one century ago [Hel79]. A number of studies has been performed in the last years to investigate the behavior of these systems in the electrochemical environment and some basic results have been established (e.g. the blocking properties of the organic layer or the influence of the film thickness on the blocking behavior), but several points (e.g. charge transfer across the layer: pure

tunneling or contributions from pinhole defects?) are still subject of debate. In the following a tentative model of such an interface is presented. The scheme in Fig. 1.4a shows a metal electrode covered by an organic layer (e.g. an alkanethiol monolayer) in contact with the electrolyte solution. The first point to be discussed is the presence and/or definition of the IHP for this interface. In the case of  $\text{CH}_3$  terminated thiol monolayers, because of the hydrophobicity of the monolayer outer interface, specific adsorption of ions is not likely to occur and so no IHP in the usual sense can be defined. An OHP, the plane of closest approach of solvated ions, as well as a diffuse layer can still be included in the model. In an electrochemical study of alkanethiol-modified gold electrodes [Son94A] a linear potential decay taking place within the monolayer and a diffuse charge developing at the electrolyte side of the interface have been proposed. Fig. 1.4b shows a qualitative potential profile corresponding to the above mentioned model. An essentially similar model has been proposed in the case of carboxyl terminated thiol monolayer [And94]. In that case, however, because of the presence of the ionizable acid end group, an IHP, defined as the plane of the terminal acid groups, has been included in the analysis. Another element has to be taken into account when building up a model of an organic layer/solution interface, especially in the case of a methyl terminated, i.e. hydrophobic, layer. It is known that the strong tendency of water molecules to form hydrogen bonds with each other influences their interaction with non-polar molecules, like alkanes, hydrocarbon or inert atoms, which are incapable of forming H bonds. When a non-polar molecule is immersed in water, if its size is not too large, water molecules can reorient themselves and pack around the molecule forming a cage (the so-called clathrate structure), in order to optimize their hydrogen bonds, a phenomenon often referred to as hydrophobic solvation [Isr91]. Obviously, the size and shape of the non-polar molecules are rather critical in determining the structure that water adopts around them. In the case of deposited monolayers

it is clear that no water cages form, but a restructuring of water molecules is likely to occur and a layer of water molecules hydrogen-bound to each other and very weakly interacting with the hydrophobic chains probably forms at the hydrocarbon/solution interface.



## Chapter 2

# Experimental

Scanning Tunneling Microscopy (STM) provides real space images of the surface structure on the micro- and mesoscopic scale. Its capability to operate not only in vacuum, but also in atmospheric conditions as well as in liquid environment, enables the study of real surfaces. The operation of STM in the electrochemical environment is a relatively new technique which allows to study in-situ the morphological changes at the electrode/electrolyte interface due to electrochemical reactions.

While variable temperature STM in vacuum is an already well developed technique [Mic91, Röd94], the use of variable temperature STM in atmospheric conditions and, even more interesting, in the liquid environment, is a new development. As explained below, this has been achieved by the use of a Peltier element coupled to the sample holder and, in the case of the measurements in liquid, by the choice of a proper electrolyte with a high boiling point in order to prevent liquid evaporation which is a major problem

with aqueous electrolytes because of the small volume of the STM electrochemical cells.

The STM measurements were carried out with a Besocke type STM [Bes87]. This "beetle" STM (Fig. 2.1) consists of a tripod formed by three piezoceramic tubes (the "legs") fixed to a metal head supporting the central scanning piezo tube which holds the STM tip. The microscope rests on an anodized aluminum ring with three ramps cut into it, each of them spanning an arc of  $120^\circ$  and having a height difference of 0.4 mm.

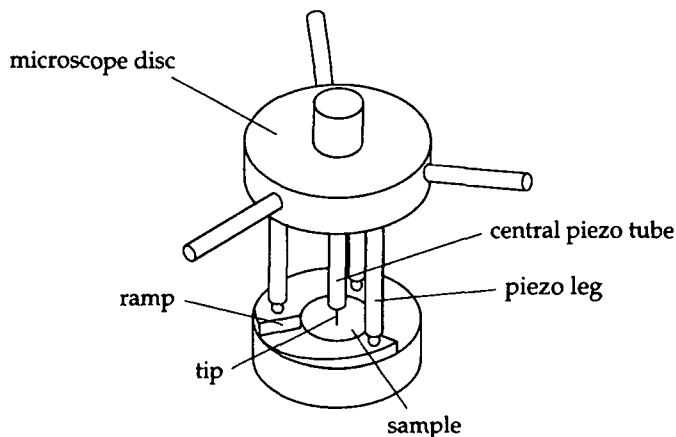


Fig. 2.1 Sketch of the "beetle-type" STM. The body of the STM is placed on a circular ramp. The coarse approach between the tip and the sample is achieved by a clockwise rotation of the STM over the circular ramp.

The coarse approach of the tip as well as the linear displacement of the microscope with respect to the sample are achieved by a collective motion of the legs which either rotates the head over the ramps (for the approach) or translates it (for the lateral transport). The tripod movement is the result of an inertial drive, i.e. a sawtooth signal is applied to the piezo electrodes, leading to

alternate bending and sliding over the ramps. A stick-and-slip motion of the tripod is thus achieved. Scanning is performed by the inner piezo which, due to the electrode arrangement [Bin86], can accomplish x-y scanning and z movement, i.e. control of the tip-to-sample distance. This design is particularly well suited for variable temperature measurements because of its internal drift compensation due to the fact that, to a first order, the thermal expansion and contraction of the three outer piezos which support the STM and of the inner scanning piezo cancel each other.

In the course of the thesis work, the original STM head has been substituted with a new one which preserves the beetle concept, but presents some modifications motivated by the analysis of the vibration of the beetle-type STM. It was found that the vibrational modes with the lowest eigenfrequencies are those corresponding to a bending of the piezo tubes. By using tubes with a diameter of 6.4 mm, instead of 3.2 mm as in the original STM, the lowest eigenfrequency of the microscope could be increased from 2 kHz to 5.5 kHz [Gas96]. To increase the STM rigidity, the possibility to damp the piezos' vibrations by means of a metal disk fixed at the tripod and clamping the piezos at their lower extremity has been introduced. Moreover, in view of the STM measurements under electrolyte, the piezos have been covered with a two component solvent based polyurethane coating (HumiSeal, Concoat Limited, Frimley Road, Camberley, Surrey GU 15 2PL, UK) in order to protect them from humidity which can cause some coupling between the different electrodes on uncoated piezos.

In order to reduce noise due to external vibrations, the microscope is mounted on a two stage damping system. As shown in Fig. 2.2, the sample holder is fixed onto a stack of three brass plates with high frequency damping viton spacers in between. To damp low frequency excitations, the stack is then placed on a granite stone mounted on three pneumatic isolators which cut-off



frequencies above 1 Hz. A plexiglass box covering the STM allows a fast thermal equilibration and provides for acoustic isolation. To obtain further stability, the whole set up is placed on a very heavy granite stone (400 Kg) lying on sand. This damping concept has been recently replaced by a different system which is found to yield a better stability and consists in placing stack and microscope on a large aluminum plate suspended by elastic ropes.

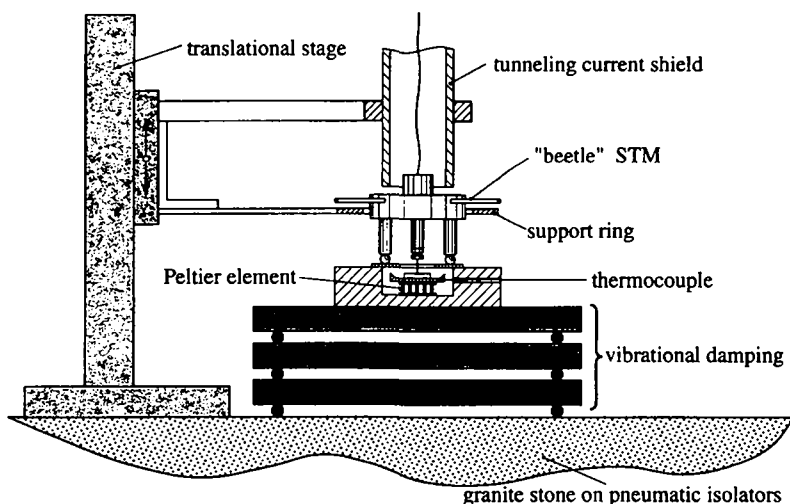


Fig. 2.2 Schematic view of the experimental set-up. The STM is lifted from the sample with the help of a support ring fixed to a translational stage.

The electronics used to control the STM is a home-built unit similar to the original Besocke beetle-type system (Besocke-Delta-Phi-Elektronik, Postfach 2243, 52428 Jülich, Germany). Images were acquired in the constant current mode, which means that the  $z$  position of the tip (i.e. the tip-to-sample distance) is adjusted during the scan in order to keep the tunneling current constant. Images were recorded either in the absolute height mode, with the gray scale reflecting the tip  $z$  position (black = bottom, white = top), or in a

differential mode which means that a high pass filter with a cut-off frequency of 33 Hz is applied to the data before representation and storage. In this mode a signal proportional to the derivative  $\partial z/\partial x$  is recorded. This procedure emphasizes the relative changes in height between neighboring points and the images appear as if the surface was illuminated from the left. Highly oriented pyrolytic graphite (HOPG) (Advanced Ceramics Corporation, P.O. Box 94924, Cleveland OH 44101, USA) and Au(111) surfaces have been used to calibrate the scanner piezo.

For the measurements performed in air, a metal sample holder has been used. It was coupled to a Peltier element which allowed temperature variation from 270 up to 390 K. The temperature of the sample was measured by a NiCr/CuNi thermocouple fixed to the border of the sample holder just below the sample. For all experiments, the STM was covered by a plexiglass box which allowed a faster thermal equilibration and created an isolated compartment which could be filled with dry nitrogen gas. Actually all the measurements at elevated temperature not performed in liquid were done in nitrogen atmosphere.

For the electrochemical experiments, an electrochemical cell adapted to the STM was built. A schematic view of the cell is reported in Fig. 2.3a. It is made of two polychlorotrifluoroethylene PCTFE disks screwed to each other with the sample fixed in between. A viton o-ring prevents electrolyte leakage. The lower plate acts simply as a support while the upper part is the proper electrochemical cell. To perform measurements at elevated temperature (up to 360 K) a modified lower disk carrying a Peltier element has been used (Fig. 2.3b). The Peltier cell was in contact with the brass plate of the damping stage on the lower side while on the upper side a thin Cu disk was placed in between sample and Peltier element for a more uniform heat transfer.

The electrochemical cell is a three electrode cell. For the STM measurements it was filled with about 1 ml of electrolyte. (111) textured gold films epitaxially grown on mica (see below) were used as working electrode (WE). The area exposed to the electrolyte was about  $0.3 \text{ cm}^2$ . A ring made from a Pt wire was used as counter electrode (CE). A polished Cu wire, etched in  $\text{HNO}_3$  and rinsed with  $\text{H}_2\text{O}$  shortly before use, served as reference electrode (RE). For the measurements in electrolytes containing no Cu, an Ag/AgCl electrode was used as reference.

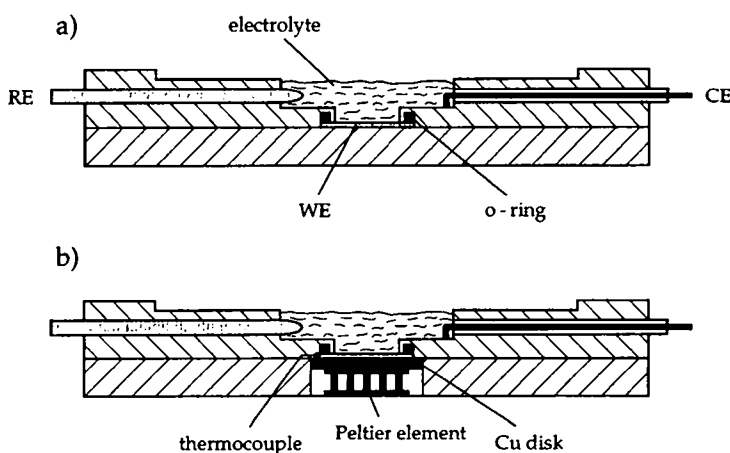


Fig. 2.3 Sketch of the STM electrochemical cell for room temperature (a) and variable temperature measurements (b).

The system was potentiostated with a PAR Model 400 EC detector (EG&G Princeton Applied Research, P.O. Box 2565, Princeton, NJ 08543-2565, USA). It could operate in a single or in a bipotentiostat configuration. In the first case the potential of the working electrode was controlled vs. the reference electrode while the tip was biased vs. the sample. In this way the tunneling bias is kept constant while the tip follows the potential of the working electrode. This mode

of operation has the advantage of a constant bias, which can be important when studying surfaces covered with organic layers. However, faradaic currents at the tip can occur, especially in the case of poorly insulated tips, when the tip potential is moved away from the ideally polarizable region<sup>1</sup>. In the bipotentiostat configuration the tip acts as a fourth electrode, controlled by the potentiostat vs. the reference electrode, with the tunneling bias resulting from the difference between tip and working electrode potentials. In this way the tip potential can be fixed in a region of low electrochemical current at the tip.

Actually the preparation of tips for the measurements under electrolyte needs some more care when compared to the experiments in air. For imaging in air mechanically cut 0.25 mm diameter Pt/Ir (80:20) wires were used as tips. For the application in liquid, insulated tips were used in order to minimize faradaic currents. They were prepared by electrochemical etching and successive coating of Pt/Ir wire. Etching was performed in a 6 M NaCN + 1 M NaOH bath by applying a 10 V dc voltage between the Pt/Ir wire (anode) and a second Pt wire (cathode). In order to coat them, the etched tips were dipped into an electrophoretic paint (Glassphor ZQ84-3211, BASF, Postfach 6123, 48136 Münster, Germany) and polarized at +10 V vs. a Pt wire acting as cathode for 2 min. The tips were then cured for 5 min in an oven at 200°C. This method produces an even, well insulating and electro-inactive coating layer, with only the extreme apex of the tip being uncovered [Bac93].

Compared to measurements in air, imaging under electrolyte not only requires a more careful tip preparation, but also imposes some restrictions on the choice

---

<sup>1</sup> The ideally polarizable region is the potential range in which only double layer charging current is observed ([Bar80], p.6)

of the tunneling parameters. To investigate thiol layers in air relatively high tunneling impedances (compared to the imaging of metal surfaces), i.e. large biases, up to 1 V, and low currents, tenths of nA, were used in order to minimize molecule/tip interactions. Different parameters had to be used in the electrochemical environment. In particular, large tunneling biases were avoided in order to prevent possible local perturbations of the working electrode potential due to the proximity of the tip. Moreover, large tunneling biases, i.e. tip potentials far from the ideally polarizable region, can induce faradaic currents at the tip. For these reasons, imaging in liquid was usually performed with tunneling biases lower than 0.2 V.

Gold films epitaxially grown on mica were used as samples. They were prepared by vacuum evaporation of 1200 Å gold (99.99% purity) onto cleaved, pre-heated round mica sheets 12 mm in diameter. (Care has to be taken in cleaving the mica in order to obtain step-free surfaces when samples destined for electrochemical measurements are prepared; gold films evaporated on densely stepped mica substrates can, in fact, easily detach when put in contact with the electrolyte). The evaporations were carried out at a base pressure of  $2 \times 10^{-6}$  mbar, at substrate temperatures of 550-570 K. The evaporations were followed by three hours of annealing in vacuum at 620 K. Before use, the gold films were flame annealed in a butane or reducing (oxygen poor) hydrogen flame to red glow and then quenched in ethanol. Following this preparation method, gold surfaces having a (111) texture with 100-200 nm large atomically flat terraces were produced. As an example, (111) terraces exhibiting the  $(22 \times \sqrt{3})$  reconstruction [Bar90] can be observed in Fig. 2.4. The image was recorded in the above mentioned differential mode which means that black (white) lines represent descending (ascending) steps when running through the image from left to right.

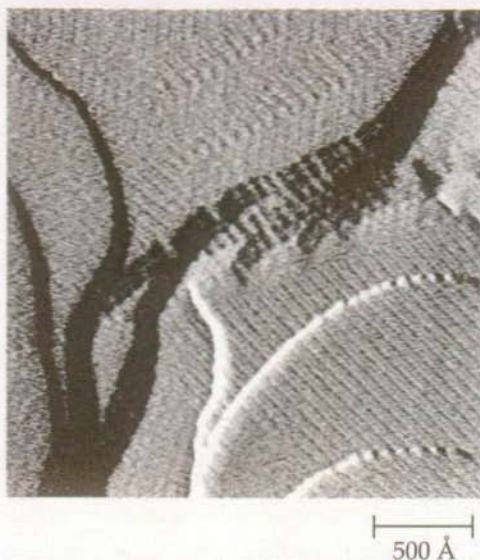


Fig. 2.4 STM image of the surface of a flame annealed gold film on mica. Terraces exhibit the  $(22 \times \sqrt{3})$  reconstruction. Tunneling parameters:  $I = 1.5 \text{ nA}$ ,  $V = 0.1 \text{ V}$ .

For the electrochemical measurements on bare gold, after flame annealing and subsequent quench in ethanol, the gold films were rinsed with deionized water (MilliQ system from Millipore Intertech, 397 Williams Street, Marlborough, MA 01752-9162, USA) and immediately transferred into the electrolyte.

The gold substrates destined to be covered with the thiol layers were flame annealed, quenched in ethanol and, while still covered by an ethanol drop, transferred into the ethanolic thiol solutions. Hexanethiol ( $\text{CH}_3(\text{CH}_2)_5\text{SH}$ ), decanethiol ( $\text{CH}_3(\text{CH}_2)_9\text{SH}$ ), dodecanethiol ( $\text{CH}_3(\text{CH}_2)_{11}\text{SH}$ ), hexadecanethiol ( $\text{CH}_3(\text{CH}_2)_{15}\text{SH}$ ) and octadecanethiol ( $\text{CH}_3(\text{CH}_2)_{17}\text{SH}$ ) (Fluka) were used as received to prepare  $10 \mu\text{M}$  solutions in absolute ethanol (p.a. Fluka). The gold samples were kept in the thiol solutions for at least 24 hours up to a few days. In the case of the thiol layers used for the electrochemical experiments, after 2-3 hours of self-assembly at room temperature the samples were kept at  $50^\circ\text{C}$  for

the rest of the assembly. They were then taken away from the solution, thoroughly rinsed with ethanol and dried, either in air or in a stream of argon. The thiol-covered samples were then transferred to the STM for imaging in air or mounted in the electrochemical cell. It should be noted that alkanethiol monolayers are stable in air for several days and they actually protect the gold surface from adsorption of atmospheric contaminants. XPS, e.g., detects the same amount of oxygen before and after prolonged (a few days) exposure of the samples to air.

As reported in the following chapters, some sample-to-sample variability in the monolayer quality was found, especially when the electrochemical behavior of the thiol-covered electrodes was tested. It should be mentioned that a similar variability in the molecular structure as well as in the thermal and electrochemical behavior of alkanethiol SAMs has been reported in other studies [Cam94, Cam97, Son94B, Son95B].

The electrochemical deposition of Cu at room temperature was performed in a 50 mM  $\text{H}_2\text{SO}_4$  + 1 mM  $\text{CuSO}_4$  electrolyte. For the measurements at elevated temperature a 2:1 mixture of ethylene glycol ( $\text{OHCH}_2\text{CH}_2\text{OH}$ ):water was used as solvent in order to increase the boiling point of the electrolyte. All potentials are reported vs. the Cu/Cu<sup>++</sup> reference electrode. The measurements with the redox couple were performed in 1 M KCl + 1 mM  $\text{K}_3\text{Fe}(\text{CN})_6$  in 2:1 ethylene glycol:water using an Ag/AgCl reference electrode. All glassware coming in contact with the solutions as well as the PCTFE cell itself were cleaned in a 7:3 mixture of  $\text{H}_2\text{SO}_4$ :30%  $\text{H}_2\text{O}_2$  or in a Nochromix (Thomas Scientific, High Hill Road 99, P.O. Box 99, Swedesboro NJ 08085-0099, USA) oxidizing solution. MilliQ water (resistivity 18.2 M $\Omega$ cm) was used to prepare all electrolytes. The chemicals used were analytical grade (Fluka).

## Chapter 3

# The alkanethiol/Au(111) interface

### 3.1 Introduction

Among self-assembled monolayers (SAMs), alkanethiols on Au(111) are the most studied and best characterized system. Because of their relatively simple structure (compared to more complex functionalized SAMs), they are appropriate systems for studying the basic mechanisms involved in the self-assembly and for understanding the interplay of the main interactions that determine the monolayer structure. Since the properties of the SAMs ultimately derive from the molecular structure, the understanding of the monolayer ordering at the nanometer scale is of crucial importance. The information obtained about the structure of the alkanethiol monolayers represents an extremely useful basis for the study of more complex functionalized thiol monolayers which are the object of an increasing interest. By varying the functionality of chain terminal group it is possible to control the surface properties of the thiol-covered substrate. The possibility of tailoring the surface



properties explains the increasing interest in these SAMs as it opens the way to a wide variety of applications.

The description of the structure of the alkanethiol/Au(111) interface will focus on two particular aspects. The first point concerns the presence of characteristic depressions at the SAM/substrate interface which could be identified as monolayer deep vacancy islands in the substrate. Having established the nature of these pits, the attention will thereafter be focused on the molecular order at the thiol/gold interface.

## 3.2 The “holes” at the alkanethiol/Au(111) surface

Alkanethiol self-assembled monolayers have been the object of intense investigation by means of diffraction methods as well as by local probe microscopies. Although diffraction studies have revealed in detail the crystalline packing of the molecules, these spatially averaging structural tools are less suited to investigate the presence and distribution of surface defects. To this end, local probe microscopies, like STM and AFM, have proven to be the methods of choice.

A typical STM image of a decanethiol/Au(111) interface is shown in Fig. 3.1. Two major differences can be observed when comparing a gold surface before (Fig. 2.4) and after (Fig. 3.1) the monolayer deposition: the thiol chemisorption induces the formation of a high density of small pits accompanied by the lifting of the Au(111) reconstruction. The depressions, a few nanometers in diameter, one gold layer in depth, are randomly distributed over the surface. They are present on the alkanethiol/Au(111) surface independently of the thiol chain length and of the concentration of the thiol solution used for the self-assembly



Fig. 3.1 STM image of a decanethiol-covered Au(111) sample at room temperature. A high pit density characterizes the surface. Tunneling parameters:  $I = 0.5$  nA,  $V = 1.0$  V.

(from undiluted thiol down to  $\mu$ M solutions [Son94B]). The pits are also present at thiol/gold interfaces prepared by gas phase deposition in vacuum [Cha93A, Poi96] and by microcontact printing [Lar97].

Different hypothesis have been proposed to explain the nature of these holes. Early STM studies attributed the observation of the depressions to the presence of holes in the monolayer (the "missing molecules" model shown in Fig 3.2a) or to regions of poorly ordered alkanethiols (Fig. 3.2b) [Han94, Kim92, Str94, Sun91]. A third proposed explanation took into account an electronic artifact of the STM contrast mechanism [Ans93]. Actually, the results of several independent measurements [Buc94A, Edi93, McC93, McD95, Poi94B, Son94B], corroborated and expanded by this work, indicate that the holes are vacancy islands in the topmost layer of the gold substrate according to the model

shown in Fig. 3.2c. In the following the observations that prove this model are presented.

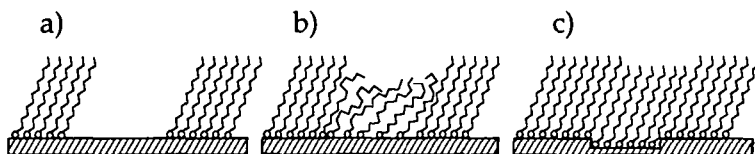


Fig. 3.2 Three possible models to explain the origin of the pits: a) missing molecules, b) disordered molecules, c) vacancy islands in the substrate (the correct model).

A first observation which would account for the substrate origin of the depressions (even if not conclusive by itself) comes from the measurement of their depth. Fig. 3.3a shows an absolute image of a hexanethiol covered gold surface. Monoatomic gold steps ( $2.4 \text{ \AA}$  in height) as well as depressions can be observed. Fig. 3.3b shows the  $z$  profile obtained by a vertical section of the image in Fig 3.3a along the marked white line. By analysis of the  $z$  profile it is possible to measure the hole depth and compare it to the gold monoatomic step. Fig. 3.3b shows that the hole depth is indistinguishable from the gold monoatomic step and that it is smaller than the thickness of the hexanethiol layer. Ellipsometric measurements of the thickness of alkanethiol monolayers on gold show an almost linear increase of the monolayer thickness from about  $7 \text{ \AA}$  for hexanethiol up to  $25 \text{ \AA}$  for octadecanethiol [Bai89B]. In this work, the hole depth has been measured on samples of different thiol chain length, from 6 up to 18 carbon atoms, and it has been found to be independent of the chain length and always corresponding to a gold monoatomic step. Occasionally depths smaller than  $2.4 \text{ \AA}$  can be found in the case of very small holes, but this is due to an imaging artifact related to the finite size of the STM tip which can

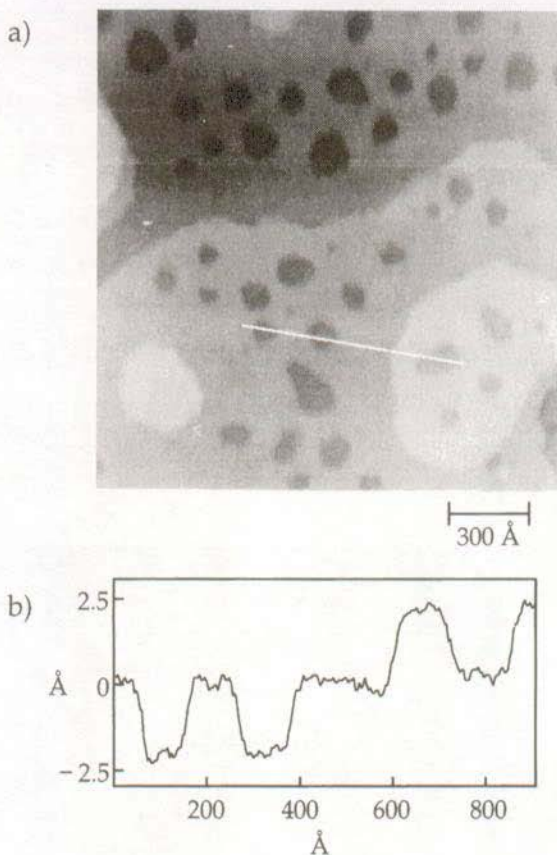


Fig. 3.3 a) Absolute STM image of a hexanethiol-covered Au(111) surface. Tunneling parameters:  $I = 0.6$  nA,  $V = 1.0$  V. b)  $z$  profile obtained by a vertical section along the white line in (a): the pit depth corresponds to the gold monoatomic step height.

not correctly probe the bottom of very small and deep depressions (a precise value for the limiting vertical/horizontal dimensions ratio which allows a correct imaging of a pit is difficult to estimate because it strongly depends on the individual tip profile which is not controllable). By itself, the observation that the pit depth corresponds to a gold monoatomic step is still not conclusive

because one could explain it in terms of the "missing molecules" model (Fig. 3.2a) making the hypothesis that the STM tip scans the surface somewhere inside the chains in such a way that the difference in the tip  $z$  position between a region covered with molecules and a bare region corresponds to 2.4 Å.

A strong support in favor of the substrate nature of the holes can be obtained by a closer inspection of the pits. Fig. 3.4 shows a molecular resolution image of a decanethiol/Au(111) surface, with the central part of the image being occupied by a hole. The image was acquired in the differential mode, which means that the black and white vertical bands correspond to descending and ascending steps, respectively.



Fig. 3.4 STM image of a decanethiol-covered Au(111) sample. The central part of the imaged region is occupied by a pit. Ordered molecular domains are present inside the hole as well as on the surrounding terrace. Tunneling parameters:  $I = 0.4$  nA,  $V = 1.1$  V.

The details of the molecular order at the thiol/gold interface will be discussed in the next section, but it can be clearly seen that ordered molecular domains are present inside the hole as well as on the surrounding terrace. The presence of regularly packed molecules inside the holes further corroborates the model in Fig. 3.2c.

In order to study the behavior of thiol covered gold surfaces at higher temperature (up to about 380 K) annealing experiments have been performed. The results of these measurements will be discussed in the next chapter, but it is interesting to anticipate at this point some of the observations as they add useful information to the present discussion. Annealing the monolayer induces a reorganization at the thiol/gold interface which ends with the complete healing of the depressions. This process happens via vacancy island coarsening (early stage) followed by coalescence and annihilation at steps (later stage).



Fig. 3.5 Octadecanethiol-covered Au(111) sample imaged at room temperature after two hours of annealing at 350 K. Pits disappear when they merge with gold steps. Tunneling parameters:  $I = 0.6$  nA,  $V = 1.1$  V.

The image in Fig. 3.5 pertains to an octadecanethiol/Au(111) monolayer annealed at 350K for 2 hours. Migration of pits towards terrace edges has already set in and some holes have been annihilated at steps as can be inferred from the irregular profile of some of them. The fact that holes completely disappear when they merge with a step, with their bottom being indistinguishable from the lower gold terrace, is a clear proof that they are vacancy islands in the upper substrate layer.

A final confirmation to this interpretation comes from the experiments related to the electrochemical deposition of copper on thiol-covered gold electrodes which are described in Chapter 5. If the depressions were pinholes in the monolayer, one would expect to observe a preferential deposition of Cu on bare gold regions, the holes, because elsewhere the blocking nature of the organic layer [Fin96, Por87] would almost prevent any deposition. On the contrary no preferential deposition inside the holes is observed and as shown in Fig. 3.6, which refers to Cu deposition on a decanethiol/Au(111) electrode, a random distribution of two-dimensional Cu islands characterizes the surface with some Cu islands being deposited inside the larger holes.

So far, the nature of the holes has been discussed and their substrate origin has been demonstrated. After the debates which accompanied the first STM studies, this model is now generally accepted.

While the nature of the holes is well understood, the mechanism of their formation is less clear. A first idea, which was suggested by the observation of dissolved gold in the thiol solution [Edi93], attributed the hole formation to an etching process of the gold substrate during the adsorption of the thiol molecules. This hypothesis was confirmed by other studies in which monolayers prepared from millimolar solutions were compared with monolayers deposited from undiluted thiols [Son94B]. In the latter case the

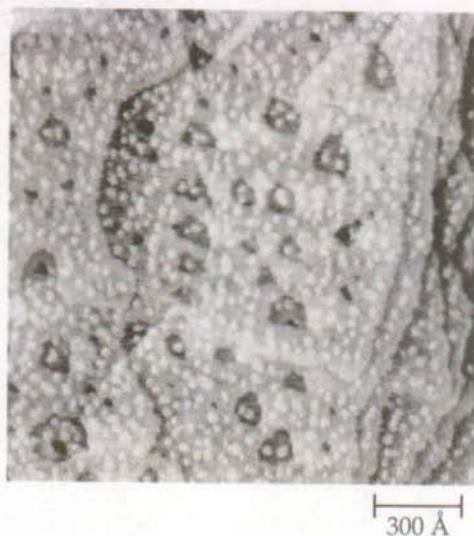


Fig. 3.6 In-situ STM image of 2D Cu islands electrodeposited on a decanethiol-covered Au(111) electrode. A random island distribution characterizes the surface, no preferential Cu deposition inside the hole is observed. Electrolyte: 50 mM  $\text{H}_2\text{SO}_4$  + 1 mM  $\text{CuSO}_4$ . Electrode potential: 50 mV vs.  $\text{Cu}/\text{Cu}^{++}$ . Tunneling parameters:  $I = 0.6$  nA,  $V = 0.05$  V.

surfaces appear more heavily etched (the hole coverage is about 30% vs. 5-10% for mM prepared layers) and higher amounts of gold are found in the self-assembling bath (5% of a monolayer vs. 2% in the former case). Etching is probably one of the processes operative in the holes formation, but it cannot be the only mechanism responsible for the pits as the amount of gold found in the solution is always smaller than the total hole area. Some other processes, like a reorganization of the surface Au atoms, must play a role. The presence of mechanisms other than etching has been demonstrated by the observation that monolayers with the same characteristics of monolayers deposited from solutions can be prepared by gas phase dosing in UHV [Cha93A, Poi96]. In this case holes cannot be attributed to gold etching.



An important aspect must be taken into consideration when discussing experiments performed in vacuum: the Au(111) surface in UHV exhibits the herringbone reconstruction [Bar90]. Au(111) can be reconstructed also after preparation in air (see Fig. 2.4) but this depends on sample preparation and is not always the case. An important change at the gold surface which accompanies the thiol chemisorption on Au(111) surfaces exhibiting the reconstruction is the lifting of the reconstruction. A recent UHV STM study [Poi97] suggests that, at least in the case of monolayers prepared in vacuum by gas phase dosing, the two processes, pit formation and lifting of the reconstruction, would be related and the pit formation would be a consequence of the relaxation of the herringbone reconstruction. According to the model proposed in that study, two atoms per  $(22 \times \sqrt{3})$  primitive unit cell would be ejected onto a terrace, thereby creating one net vacancy per  $(22 \times \sqrt{3})$  unit cell. Because of the faster diffusion of adatoms with respect to vacancies, the adatoms would diffuse rapidly to ascending step edges, while the vacancies would nucleate vacancy islands in the terraces. As the reconstructed Au(111) surface is compressed by 4.4% relative to the bulk, ejecting two atoms per unit cell would result in a total vacancy island area of 4.4% of a monolayer, which, again, cannot account for the total observed hole area.

A correlation between the hole formation and the symmetry of the gold surface emerges also in the case of SAMs prepared by microcontact printing [Lar97]. By controlling the concentration of the thiol solution used to ink the stamp, monolayers can be produced in which the holes are aligned along high symmetry directions of the underlying Au(111) substrate.

A further strong indication of the relation between hole formation and surface symmetry comes from a recent study of methanethiol monolayers adsorbed from the gas phase [Dis97]. This study shows that, at low dosing, the pits are

not only aligned, but their alignment follows the pattern of the herringbone reconstruction.

The two mechanisms, the chemical etching and the restructuring of the gold surface, are involved in the vacancy island formation, but further investigations will be necessary in order to obtain a comprehensive picture of the mechanism of modification of the gold morphology accompanying the thiol deposition and its relation to the SAM preparation method. However, important results have been established about the alkanethiol/Au(111) interface: the thiol layer uniformly covers the whole surface and vacancy island defects, which are structurally equivalent to step defects, unavoidable on real surfaces, do not diminish the physical and charge transfer blocking properties of the interface. The latter is an important point to retain not only in view of the discussion of the molecular order of these SAMs, but also in relation to the metal electrodeposition as described in chapter 5.

### **3.3 Molecular order at the alkanethiol/Au(111) interface**

This paragraph presents the results concerning the molecular order at the alkanethiol/Au(111) interface. As will result from the discussion, the molecular ordering of the SAM is determined by the delicate balance between the covalent bonding at the adsorbate/substrate interface and the intermolecular chain interactions (of the van der Waals type) within the monolayer. Before presenting the results of the STM measurements, the information about the molecular order recently obtained by different studies are briefly reviewed to supply the necessary basis for the interpretation of the STM results. The knowledge of the molecular structure of these monolayers derives from a

variety of experimental studies, employing vibrational spectroscopy, electron, thermal helium and X-ray diffraction as well as real space microscopy.

The consensus from these studies is that the molecules are ordered in a high-density crystal-like packing with the alkyl-chain axis canted. The parameters defining the orientation of a thiol molecule are shown in the model in Fig. 3.7 which schematically represents a decanethiol molecule in the *all-trans* conformation. The orientation of the molecule is defined by the molecular tilt  $\theta_m$ , the angle of twist of the C-C-C plane about the molecular axis  $\phi_t$  and the angle of precession of the molecular axis around the surface normal  $\chi$  which determines the direction of the tilt.

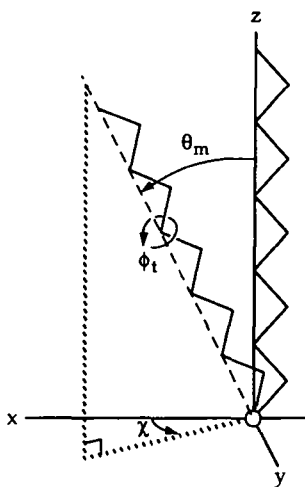
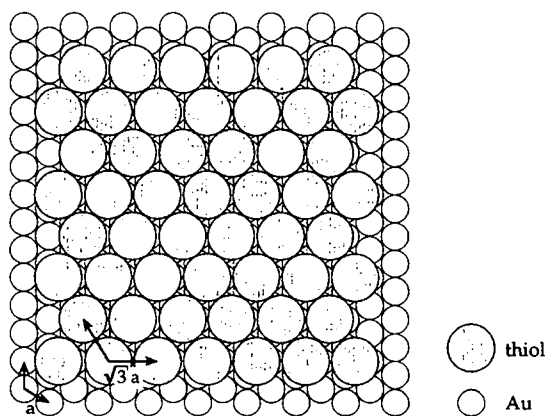


Fig. 3.7 Angles defining the orientation of a thiol molecule on a surface:  $\theta_m$  is the tilt angle,  $\phi_t$  is the twist angle of the C-C-C plane, and  $\chi$  is the precession angle of the molecular axis around the surface normal.

The analysis of the vibrational spectra indicates that the alkyl-chains are in the *all-trans* conformation and the average tilt of the molecules is  $\theta_m \approx 30^\circ$  [Por87]. A sulfur-substrate bond adopting a commensurate  $(\sqrt{3} \times \sqrt{3})R30^\circ$  structure

(Fig. 3.8) with identical adsorption sites has been proposed [Chi89, Str93, Wid91A]. X-ray diffraction measurements determine a tilt direction of the hydrocarbon chains roughly midway between the nearest-neighbor (NN) and the next-nearest-neighbor (NNN) directions [Fen93]. Recent X-ray diffraction [Fen94], nonlinear optical studies [Yeg95] and photoelectron spectroscopy measurements [Zub95] questioned this simple interfacial ordering. The authors of the diffraction study rather suggested the occupation of two inequivalent sites and a tendency towards disulfide bonding. Such a model seemed to be in accord with the observation of two sulfur species revealed by XPS [Zub95]. However, a new investigation of the damages induced in alkanethiol monolayers by exposure to X-rays and low energy electrons has shown that the second sulfur species (which was interpreted as an indication of the disulfide existence) is actually due to beam damage [Jäg97]. Alkanethiol monolayers are found to exhibit an unexpectedly high cross section for X-ray induced damage that is caused by the secondary electrons resulting from the photoemission process.



**Fig. 3.8** Top view model of the  $(\sqrt{3} \times \sqrt{3})R30^\circ$  adlayer structure of thiols on Au(111) ( $a = 2.88 \text{ \AA}$  is the lattice parameter of Au(111)).

Furthermore, He-diffraction [Cam93A], that probes selectively the methyl end group, has shown that the competition of chemisorption and van-der-Waals energy leads to a further super-molecular ordering with four molecules per unit cell. The diffraction signatures were associated with a  $c(4 \times 2)$  superstructure with respect to the  $(\sqrt{3} \times \sqrt{3})R30^\circ$  lattice (which can also be described as a  $(3 \times 2\sqrt{3})$  superlattice in terms of the Au(1x1) structure). These measurements were interpreted in terms of a patterned arrangement of different twist angles of the alkyl chains, similar in nature to the molecular chain packing found in bulk alkane crystals. This super-molecular ordering was observed only for chain lengths  $n \geq 10$  and temperatures  $T < 100$  K, which was ascribed to thermal disordering of the methyl groups at higher temperatures. Infrared spectroscopy studies [Nuz90B], that probe the order of the entire chain, confirmed the existence of superstructures; they did, however, reveal the superstructure up to temperatures higher than the values observed in the He diffraction study. Fig. 3.9 reports infrared spectra of a docosanethiol ( $\text{CH}_3(\text{CH}_2)_{21}\text{SH}$ ) monolayer in the low-frequency region at different temperatures (from [Nuz90B]). The vibration mode centered at about  $1467 \text{ cm}^{-1}$  (spectrum at 300 K) is assigned to the methylene scissors deformation, while the mode at  $1383 \text{ cm}^{-1}$  is attributed to the symmetric methyl deformation. The comparison of the spectra at different temperatures reveals that the methylene scissors deformation peak splits upon cooling. By decreasing the thiol chain length, the same transition to a split band structure is observed, but the temperature range in which this occurs shifts downwards with decreasing chain length: decanethiol monolayers present such a band splitting only up to 200 K. By the analysis of the peak splitting, the relative setting angle of the molecular carbon planes in the superstructure has been estimated to be  $90^\circ$  whereas the absolute angles could not be determined [Dub93].

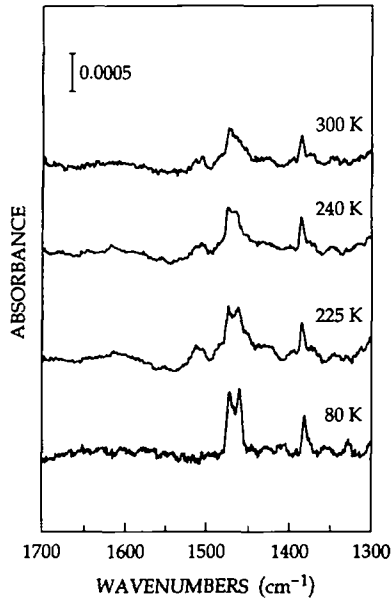


Fig. 3.9 Infrared spectra showing the peak-splitting of the methylene scissors deformation (at about  $1467\text{ cm}^{-1}$ ) on cooling (from [Nuz90B]).

The observed thermal behavior of the chain ordering is in accord with the idea of a propagation of molecular defects from the outer methyl group to the inner methylene groups with increasing temperature [Ulm91B]. In agreement with these observations, molecular dynamics simulations indicate a progressive disordering of the monolayer structure when temperature is increased [Bha97A, Hau90]. The transition towards disorder occurs via a progressive unlocking of the tilt direction accompanied by a decreasing of the tilt as well as by an increasing population of *gauche* conformations starting from the chain ends.

STM measurements, on the other hand, detected the super-molecular ordering even at room temperature. As will become clear in the following, the observation of the molecular ordering at 300 K is not too surprising because the

STM image contrast, at least at the tunneling impedance of about  $1\text{ G}\Omega$  used in this study, is dominated by the interfacial bonding of the sulfur head group.

In the following the results of the STM investigation of the molecular ordering of hexane- and decanethiol monolayers on Au(111) are discussed. Hexanethiol and decanethiol have been chosen as examples of short chain and intermediate/long chain monolayers. Because of the poorly conducting nature of the alkyl groups, long chain thiol monolayers are less suited for STM investigations and experiments aimed to obtain molecularly resolved images on octadecanethiol were unsuccessful. For this reason, most of the STM molecular structure investigations reported in literature, either at low or high gap impedance, have studied thiol monolayers formed by molecules with no more than 12 carbon atoms in the chain [Ans94, Buc94B, Del94A, Poi94A, Poi94B, Sch95].

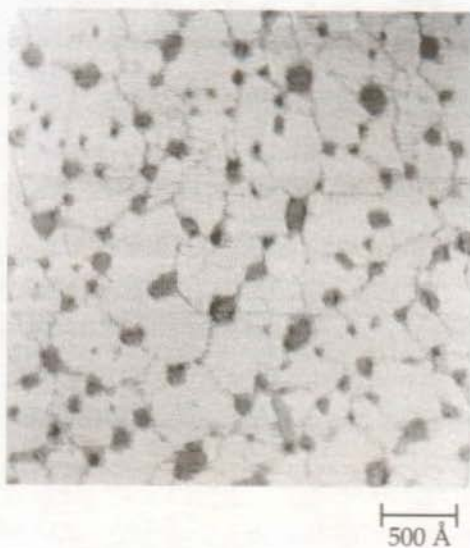


Fig. 3.10 STM image of a decanethiol-covered Au(111) surface. Domain boundaries pinned by the vacancy islands can be observed. Tunneling parameters:  $I = 0.3\text{ nA}$ ,  $V = 0.9\text{ V}$ .

A typical STM image of a decanethiol monolayer on the Au(111) surface is shown in Fig. 3.10. The sample has been annealed at 320 K for 60 hours during self-assembly. Together with the characteristic holes, lines, imaged as depressions, can be observed. The lines, which are boundaries between different molecular domains, are pinned by the vacancy islands. This suggests that the domain size is somehow related to the hole density. As discussed in the next chapter, the results of the annealing experiments confirm the existence of a relationship between domain size and pit density: annealing induces a reorganization at the thiol/gold interface which results in the increase of the domain size as well as in the decrease of the hole density. A higher resolution image of a decanethiol/Au(111) interface is shown in Fig. 3.11 which illustrates the multi-domain molecular ordering of the monolayer.



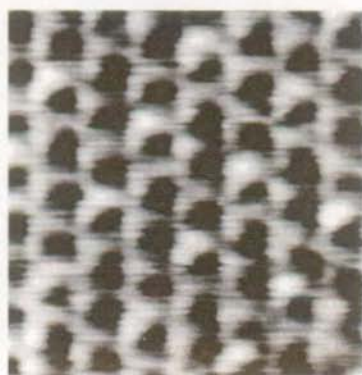
Fig. 3.11 High resolution image of a decanethiol-covered Au(111) surface. Two different types of molecular domains, denoted A and B (see text), coexist on the surface. Tunneling parameters:  $I = 0.8 \text{ nA}$ ,  $V = 1.4 \text{ V}$ .



The sample had been prepared by self-assembly at room temperature, but before imaging at 300 K it was annealed for about 30 min at 350 K. A nice patchwork of molecular domains with sizes of the order of 100-300 Å is observed. The majority of domain boundaries are running along the high symmetry directions of the trigonal substrate. Some of the domain boundaries are imaged as very narrow lines (less than 10 Å in width) while others have a considerable image width of 20-30 Å. One might speculate about the different origin of the two types of boundaries. Thin boundaries can be thought of as "light" domain walls associated with stacking faults or phase shift in the chain tilt direction while the thick boundaries are more likely associated with missing rows of molecules [Sch95].

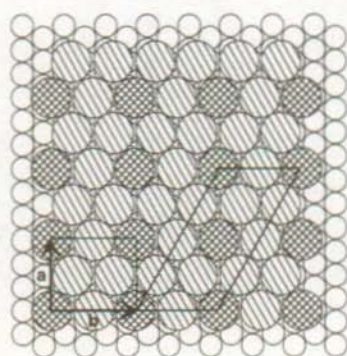
In the decanethiol monolayer two particular structures, assigned A and B, occupy the majority of the surface. These domains have four molecules per unit cell. In Fig. 3.12a,c, two STM images with high magnification reveal the details of the molecular ordering. Both domains form  $c(4 \times 2)$  superstructures with respect to a  $(\sqrt{3} \times \sqrt{3})R30^\circ$  lattice. As shown in the models in Fig. 3.12b,d, in the "pinwheel" structure of domain A three of the four molecules per unit cell are equivalent (in the sense that they have the same orientation) whereas in the "zig-zag" structure of domain B two molecules in the unit cell are equivalent. The zig-zag structure of domain B coincides with the  $c(4 \times 2)$  super-molecular ordering postulated on the basis of He diffraction measurements [Cam93A]. Besides the dominant A and B domains a further  $c(4 \times 2)$  structure which is the inverted pinwheel pattern, a central dark spot surrounded by a hexagonal arrangement of bright spots, has sometimes been imaged. These domain structures have been observed in STM studies of dodecanethiol monolayers at room temperature [Ans94, Del94A] and have been explained in terms of the Camillone model [Cam93A] which assigns the order to a patterned rotation of the molecular chains. In some other STM studies [Poi94A, Sch95]  $c(4 \times 2)$

a)  
c(4x2) pinwheel superstructure



5 Å

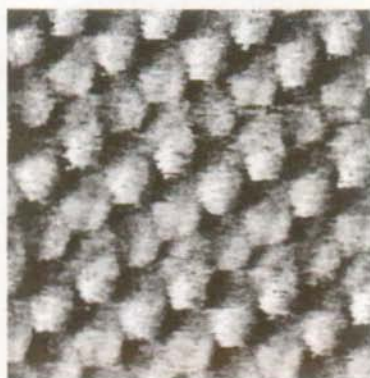
b)



$a = 8.68 \text{ \AA}$   
 $b = 10.02 \text{ \AA}$

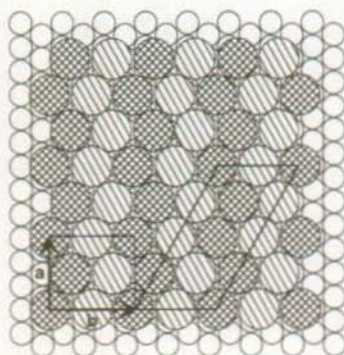
5 Å

c)  
c(4x2) zig-zag superstructure



5 Å

d)



$a = 8.68 \text{ \AA}$   
 $b = 10.02 \text{ \AA}$

5 Å

Fig. 3.12 Molecular resolution STM image (a) and model (b) of the c(4x2) pinwheel superstructure on a decanethiol/Au(111) surface. (c) and (d) the same for the c(4x2) zig-zag superstructure. Tunneling parameters: in (a)  $I = 1.0 \text{ nA}$ ,  $V = 1.0 \text{ V}$ ; in (c)  $I = 0.6 \text{ nA}$ ,  $V = 1.0 \text{ V}$ .

supermolecular order has been reported, but only the zig-zag pattern has been observed.

The interpretation of the high resolution STM images of decanethiol monolayers on Au(111) is now discussed in the context of the structural data available for long-chain thiol monolayers. The difference in the temperature dependence of the molecular ordering observed with the three different experimental techniques, He-scattering, IR-spectroscopy and STM, results from their selective sampling depth. Due to its thermal energy (14 meV in [Cam93A]) the probing He beam does not penetrate the thiol monolayer. He diffraction is thus exclusively sensitive to the ordering of the outermost part of the molecular layer, i.e. the methyl tail groups. According to the He diffraction data the  $c(4 \times 2)$  ordering of the tail groups disappears at 100 K. IR spectroscopy, on the other hand, probes the ordering of the entire alkyl chain. With this technique the orientational ordering of the methylene groups is found to persist up to 200 K [Nuz90B]. In the present study, STM experiments detected super-molecular ordering up to 310 K. As it is generally accepted that disordering of the alkyl chains propagates from the external to the internal interface with increasing temperature it is natural to conclude that the sensitivity of the tunneling microscopy is associated with the orientational order at the interfacial sulfur-gold bonding.

The STM sensitivity to the substrate-monolayer interface is also supported by a calculation of the electronic density for a hexanethiol molecule on a cluster of 3 gold atoms [Reu]. The calculation is based on the density-functional theory and is carried out within the local-spin-density approximation. The contribution to the local electronic density due to the orbitals with an energy level lying in a window of about 1.5 eV below the Fermi level has been calculated. Fig. 3.13 shows the contours from 0.000 to 0.003 electron/(a.u.)<sup>3</sup> of the integrated local electronic density in the plane of symmetry of the molecule. One can observe



Fig. 3.13 Local electronic density of a hexanethiol molecule on a cluster of three Au atoms integrated in an energy window of 1.5 eV below the Fermi level. Contours from 0.000 to 0.003 electron/(a.u.)<sup>3</sup> (1 a.u. = 0.53 Å) in the plane of symmetry of the molecule (from [Reu]).

that the electronic density at the sulfur-metal bond is much higher than respective values of the alkyl chain and is therefore expected to give the major contribution to the tunneling current.

Further support for this interpretation comes from the fact that, in the present study, the super-molecular ordering was imaged with conventional tunneling parameters at tunneling biases of about 1 V and currents of about 1 nA (i.e. an impedance of only 1 GΩ) which would probably level out small corrugations of the monolayer by mechanical contact with the tip. The occurrence of elastic deformation of the monolayer during the tip scanning has been proposed on the basis of the analysis of the interaction force gradient between tip and sample during scanning [Dür93]. The same conclusion results from a Monte

Carlo simulation of the mechanical relaxation of a thiol monolayer subjected to tip loading (approaching)/unloading (retracting) cycles [Sie93].

It has to be mentioned that in order to minimize the tip/monolayer interaction, most of recent STM investigations in air as well as in UHV have been performed at a very high tunneling resistance of several hundred G $\Omega$ . Two different explanations of the origin of the STM image contrast have been proposed in the case of high tunneling impedance imaging. The first interpretation, based on the chain rotational disorder at room temperature and the insulating nature of the alkyl chains, attributes the STM contrast to the sulfur/gold interfacial structure [Sch95]. On the other hand, based on the capability of high impedance STM to distinguish between thiol molecules having different chain terminal groups, a second interpretation has been proposed, according to which, at high tunneling resistance, the dominating contribution to the STM signal comes from the tail groups [Del96, Tak95].

However, on the basis of the discussion above, in the case of conventional tunneling imaging performed in the present study, the major contribution to the STM contrast comes from the sulfur/gold interface.

Based on all available data, the most straightforward explanation of the two dominating domain structures A and B, which is also in accord with the IR-data, is the model shown in Fig. 3.14. The superstructure unit cells contain four inequivalent molecules collectively tilted along non-symmetry directions of the substrate (midway between the NN and the NNN directions as inferred from X-ray data [Fen93]). The c(4x2) superstructures are the result of a patterned rotation of the alkyl chains about their molecular axes. It should be noted that, at room temperature, this orientational order of the molecules is mainly localized at the substrate/head group interface (Au-S-C structure) because of the thermal disordering of the chains. In the pinwheel structure one chain is

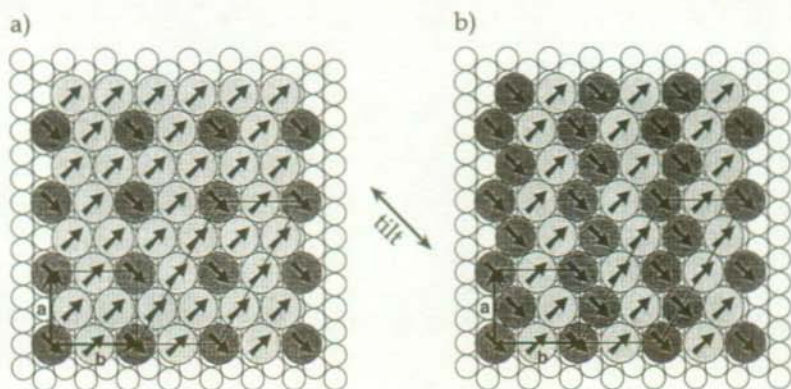


Fig. 3.14 The pinwheel (a) and the zig-zag (b)  $c(4 \times 2)$  superstructures result from a patterned orientation of the molecule carbon planes (indicated by the arrows). The relative setting angle of the carbon planes is  $90^\circ$  (whereas the absolute angle is not determined). Because of the tilt along a non-high symmetry direction, molecules with differently oriented backbones become inequivalent.

twisted clockwise and three are twisted counterclockwise, while in the zig-zag structure two chains are twisted clockwise and two are twisted counterclockwise. Due to tilting along a non-symmetry direction, differently twisted chains become symmetrically inequivalent owing to their different environment.

The important role of the head group/substrate interaction in the subtle interplay of the different forces responsible for the monolayer order is confirmed by the comparison of the molecular order of thiol SAMs prepared on different substrates. A low-temperature He diffraction study of docosanethiol monolayers on Au(111), Au(110) and Au(100) revealed a dependence of the unit cell of the SAMs structure on the substrate symmetry [Cam93B]. Moreover, thiol monolayers chemisorbed on Ag(111) are found to adopt a

molecular tilt  $\theta_m$  of about  $12^\circ$  [Lai91]. An even stronger modification of the SAM structure is observed when the crystalline substrate is substituted by a disordered one. A recent X-ray study of long chain alkanethiol monolayers on mercury [Mag96] reveals that no in-plane long-range order is present in the layer. This is explained by the dominating role of the strong interaction of the sulfur group with the underlying disordered liquid over the order-promoting interactions of the alkyl chains.

So far the molecular ordering of long-thiol monolayers with ten or more carbon atoms prepared by self-assembly in solution and annealed at temperatures below 370 K has been discussed. As will be clear from the following, the deposition and annealing protocols have to be carefully considered when investigating the molecular order because a rich variety of structures is observed depending on the sample history.

The attention will now be focused on short-chain monolayers, which turn out to have an even richer molecular ordering behavior. This is demonstrated in Fig. 3.15 which shows a high resolution STM image of a hexanethiol monolayer on Au(111). Similar to the long-chain monolayers, hexanethiol on Au(111) is characterized by a multi-domain ordering with the coexistence of several distinct molecular superstructures. In the STM image in Fig. 3.15 three different structures can easily be identified. As in the case of decanethiol, the  $c(4 \times 2)$  molecular ordering with the pinwheel structure (again marked A) and with the zig-zag structure (again marked B) can be observed. In addition a third dominant structure marked C is present at the interface. The ratio between areas covered by the  $c(4 \times 2)$  and by the striped superstructure C strongly depends on each sample, as shown for instance by the image in Fig. 5.16 in which the stripes cover about 50% of the surface. This uniaxial pattern has been observed to be the dominant one or, on some samples, even the only one present. Its structure is characterized by parallel stripes having a width of



Fig. 3.15 High resolution image of a hexanethiol-covered Au(111) surface. In addition to the A and B structures observed also on decanethiol, a further striped pattern, denoted C, characterizes the surface. Tunneling parameters:  $I = 1.0 \text{ nA}$ ,  $V = 1.4 \text{ V}$ .

about  $22 \text{ \AA}$ , running along the next-nearest-neighbor directions of the Au(111) substrates. A higher magnification image of this structure is reported in Fig. 3.17 which shows each stripe as formed by four molecular rows, three appearing brighter and the fourth being darker. A possible explanation for the observation of the striped pattern takes into account the presence of stacking faults in the molecular packing giving rise to an increased intermolecular distance, and consequently to a lower molecular density, in the direction normal to the stripes. Based on the observation that a stripe, containing four molecular rows, has a width of about  $22 \text{ \AA}$  (a stripe of  $22 \text{ \AA}$  would accommodate five rows of molecules in the case of the  $(\sqrt{3} \times \sqrt{3})R30^\circ$  structure), one can postulate a coverage of 80% compared to the "full" density monolayer.





Fig. 3.16 Large uniaxial domains on a hexanethiol-covered Au(111) surface. The percentage of the surface occupied by the striped pattern strongly depends on individual samples. Tunneling parameters:  $I = 0.3$  nA,  $V = 0.8$  V.

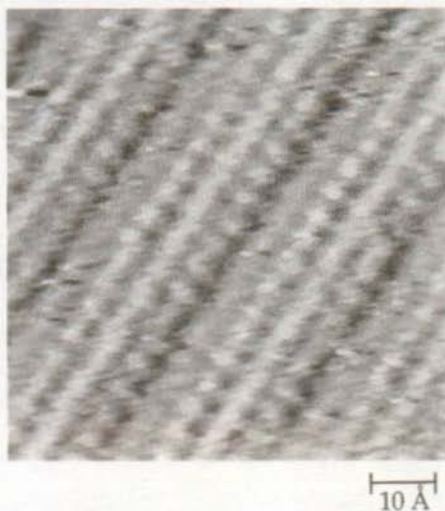


Fig. 3.17 Molecular resolution image of the uniaxial structure on a hexanethiol-covered Au(111) surface. The intermolecular distance along the stripes corresponds to the nearest-neighbor distance of the  $(\sqrt{3} \times \sqrt{3})R30^\circ$  adlayer, while normal to the stripes the distance between adjacent rows of molecules is expanded by 20% compared to the inter-row distance of the  $(\sqrt{3} \times \sqrt{3})R30^\circ$  structure. Tunneling parameters:  $I = 0.5$  nA,  $V = 1.0$  V.

Similar uniaxial structures have been observed in another STM study on short chain monolayers deposited from solution [Poi94B].

Together with chain length, the thermal treatment of the sample turns out to be a crucial parameter for the molecular order of the resulting monolayer. This has been observed for decanethiol monolayers: annealing at about 370 K induces a phase transition in the monolayer order from the  $c(4 \times 2)$  to the uniaxial structure as shown in Fig. 3.18 which refers to a decanethiol monolayer after annealing at 370 K. The surface is characterized by the striped pattern which has never been observed on solution prepared decanethiol monolayers before annealing at 370 K. The same phase transition has been observed by Camillone et al. [Cam94] who, by STM and low energy He diffraction, detected the striped structure on annealed decanethiol monolayers. The beginning of a desorption process could be at the origin of the transformation from the  $c(4 \times 2)$  to the striped structure.



Fig. 3.18 After annealing at 370 K, a transition from the  $c(4 \times 2)$  to the striped structure is observed on decanethiol-covered Au(111) surfaces. Tunneling parameters:  $I = 0.5$  nA,  $V = 0.95$  V.

Another important element which influences the monolayer structure is the deposition method. Striped structures have been obtained also in the case of monolayers prepared by molecular beam deposition in UHV [Cam96, Dub93, Him97]. Dosing in vacuum, however, has shown that different kinds of striped patterns (see Fig. 3.19a-c) can be obtained depending on the thiol coverage. In particular, very low density monolayers characterized by molecules lying flat on the substrate can be prepared in UHV. This results from He diffraction investigations [Cam96] of the striped structures on low coverage short chain monolayers prepared by gas phase dosing in vacuum. These measurements showed a linear scaling of the distance between rows with the length of the molecules, with the stripe width being almost two times the thiol length. This observation has been interpreted in terms of a "flat molecule" model. A similar interpretation has been proposed to explain the results of a LEED and XPS study of heptanethiol ( $\text{CH}_3(\text{CH}_2)_6\text{SH}$ ) monolayers prepared by gas phase dosing in UHV [Him97]. A recent LEED study has shown that, by increasing the thiol dosing, it is possible to manipulate the monolayer structure from the "flat molecule" configuration to monolayers of increasing density which are characterized by stripes of decreasing width and by decreasing tilt angles of the molecular axis [Ger97]. This study is in agreement with a UHV STM investigation [Poi96] of short chain monolayers prepared by gas phase in vacuum. The STM showed how, once a saturation coverage of the low density striped structure is reached, further dosing results in the transition to the denser phase with a molecular axis realignment.

The possibility to prepare monolayers with different molecular density and, consequently, different molecular structure has been demonstrated also by the use of the microcontact printing technique [Lar97]: by varying the concentration of the thiol solution used to ink the elastomeric stamp, it is possible to control the monolayer structure at the molecular level.

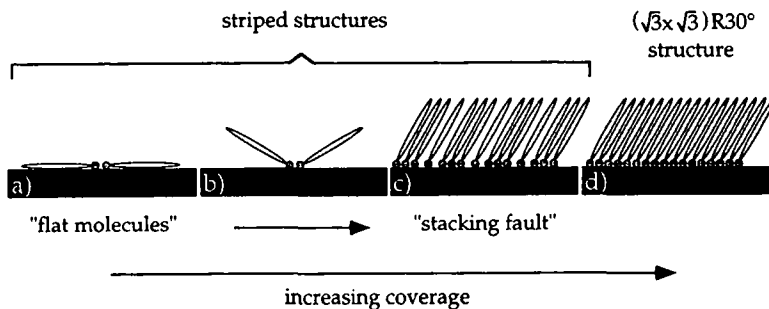


Fig. 3.19 Schematic representation of the different types of molecular structures obtained by varying the deposition procedure, the thermal treatment and the chain length.

All together these studies indicate that the preparation method has a profound influence on the structure of the SAM. They show that the striped patterns, generally referred to as  $p \times \sqrt{3}$  superstructures with  $p$  varying from 7.5 to 13, cannot be explained by a unique model since different kinds of striped monolayers can be obtained depending on thiol chain length and preparation procedure.

The most reasonable picture which can be drawn on the basis of the different observations accounts for a rich coverage-dependent and chain length-dependent phase behavior which is schematically summarized in Fig. 3.19. In the case of very low coverage obtained with well controlled deposition flux by gas phase dosing, the lowest "full" coverage monolayers with molecules lying almost flat on the surface are produced [Cam96, Him97]. Increasing the coverage, which means monolayers prepared by higher dosing in vacuum, by microcontact printing through a careful control of the "ink" concentration, by solution deposition of short chain thiols or by thermal treatment of high density monolayers, striped structures with smaller periodicity and progressively smaller chain tilt are formed until the full coverage with  $30^\circ$  tilt is reached.

The richness in molecular structures obtained by varying thiol chain length as well as sample preparation conditions reveals the extreme complexity of the assembly process which results from the balance of different interactions.

Numerous theoretical studies have been performed to establish the molecular ordering of thiol monolayers on Au(111). The applied techniques include static energy calculations, Monte Carlo simulations and molecular dynamics. Most theoretical calculations failed to predict the  $c(4 \times 2)$  molecular ordering and proposed a  $(2 \times 1)$  herringbone arrangement, similar to that observed in the packing of bulk alkane crystals, as minimum-energy structure [Mar94]. The weak points in all these studies are certainly the interaction potentials, and in particular the Au-S potential. As it has usually been assumed that the inter-chain interactions are at the origin of the molecular ordering, much less effort has been put in a sophisticated modeling of the interfacial bonding of the sulfur head group. Recently, molecular dynamics simulations have been performed, in which the sulfur head group and the substrate gold atoms were allowed to move [Bha97B]. The interesting result of this more flexible modeling of the gold/sulfur interface is the prediction of four possible low energy  $c(4 \times 2)$  superstructures with four molecules per unit cell.

Of particular importance for the comparison with theoretical studies is the observation of the multi-domain ordering. As discussed above, several molecular superstructures have been observed to coexist at room temperature. In particular the two dominating  $c(4 \times 2)$  domain structures have been found with nearly equal probability at the decanethiol/gold surface. From the thermodynamic point of view this suggests that they are very close in total energy.

### 3.4 Conclusions

The structure of the alkanethiol/Au(111) interface has been investigated by STM. At the mesoscopic scale, the interface is characterized by a high density of small depressions, one monoatomic layer deep, which are found to be vacancy islands in the topmost gold layer formed during the thiol chemisorption. At the microscopic scale, the molecular order of decanethiol and hexanethiol monolayers on Au(111) has been investigated. Several ordered molecular domains have been found to coexist at room temperature. Molecular resolution images reveal some characteristic differences between the two observed monolayers. In the case of decanethiol, the STM data are strongly in favor of the usually accepted  $(\sqrt{3} \times \sqrt{3})R30^\circ$  ordering of the sulfur head groups modulated by a patterned rotation of the hydrocarbon chains about their molecular axes which results in two coexisting  $c(4 \times 2)$  superstructures. Hexanethiol monolayers show an additional striped  $p \times \sqrt{3}$  structure which can be attributed to less dense packing of the molecules. Interestingly, decanethiol monolayers (characterized by the  $(\sqrt{3} \times \sqrt{3})R30^\circ$  order) undergo a transition to the  $p \times \sqrt{3}$  structure upon annealing.



## Chapter 4

# Thermal mass transport at the alkanethiol/Au(111) interface

### 4.1 Introduction

In recent years, several techniques have been employed to characterize thiol monolayers on gold, but, despite the great amount of studies, the attention has generally been focused on the molecular structure of the monolayer which, once formed, has been viewed as largely immobile. Only a few investigations have been done to study the stability of the monolayer, e.g. collective properties and mass transport in these systems after chemisorption.

In this chapter the results of thermal annealing experiments on the thiol/gold interface will be described. The structural changes characterizing the interface on the mesoscopic scale during a thermal treatment are discussed. As reported in chapter 3, the interface is characterized by vacancy islands in the topmost gold layer which are a direct consequence of the thiol chemisorption. The major



change induced by the annealing up to 350-370 K is the healing of these defects. As discussed in the following, different mechanisms are operative in the hole healing: in the initial stage at 320-360 K, the average vacancy island radius increases with a coarsening kinetics which is found to be consistent with an Ostwald ripening mechanism. In a later stage, coalescence and annihilation of holes at steps allow the complete healing of the defects, leaving perfectly flat depression-free interfaces. On the molecular scale, annealing induces a reorganization of the monolayer which results in the increase of the average molecular domain size. Upon further heating of the monolayer (up to temperatures which depend on the thiol chain length and, to some extent, on each individual sample), the thiol desorption sets in.

## 4.2 Initial stage of the annealing: the Ostwald ripening mechanism

Following the classical approach of Lifshitz and Slyozov [Lif61] and Wagner [Wag61] for the growth of three-dimensional clusters in solution, the kinetics of mass flow accompanying the growth of two-dimensional clusters on a surface can be described in a similar way as the result of mainly two processes: the adsorption/desorption of an adatom at the edge of an island and the two-dimensional diffusion of the adatoms on the terraces [Wyn75]. The same model can also be applied to the mass transport accompanying the growth of two-dimensional vacancy islands on a surface. According to this approach, two basic elements have to be considered. First, the curvature of a pit's edge enhances the concentration of monovacancies around the pit with respect to the monovacancy density near a straight step. According to the Gibbs-Thomson relation, the equilibrium concentration of monovacancies at the edge of a pit depends on the pit radius  $r$  as:

$$c_{eq}(r) = c_{\infty} e^{\gamma\Omega/rk_B T}$$

where  $c_{\infty}$  is the equilibrium concentration of vacancies near a straight step edge,  $\gamma$  is the step edge free energy,  $\Omega$  is the area of the surface occupied by a monovacancy,  $k_B$  is the Boltzmann constant and  $T$  is the temperature. The Gibbs-Thomson relation implies that the equilibrium concentration is greater near the edge of a small pit than at the edge of a larger one. As a consequence the evaporation rate of monovacancies will be faster at the edge of small holes than at the edge of large ones, which explains the growth of large vacancies at the expense of smaller ones. The second process to be considered is the two-dimensional, concentration gradient driven diffusion of monovacancies away from high curvature pit boundaries towards less curved step edges where the monovacancies concentration is lower. The relative rates at which monovacancies desorb from the vacancy border and at which they diffuse over the surface determine the monovacancy concentration near a pit edge. If the rate of monovacancy detachment is very low, surface diffusion easily disperses these monovacancies among the background concentration due to straight steps and the concentration near curved edges is only slightly higher than near straight edges. On the other side, if the monovacancies desorb from the pit edge faster than the diffusion can disperse them, the concentration near the hole edge approaches the equilibrium value given by the Gibbs-Thomson relation. Each of these two processes has its proper activation barrier and for each examined system the resulting kinetic behavior depends on the energetic balance between the two processes at the microscopic level.

The balance between the rates of the two processes plays an important role in the mass flow because it determines the exponent of the scaling law  $r \propto t^n$  which describes the increase of the average pit radius as a function of time [Zin92]. If the evaporation rate of vacancies from the pit edge is faster than the diffusion rate, then surface diffusion is the limiting step in the mass flow and

$n = 1/3$ . On the other hand, if the detachment rate of vacancies is the limiting process in the mass transport, the exponent is  $1/2$ .

It should be mentioned that a different interpretation for the two possible cases,  $n = 1/2$  and  $n = 1/3$ , has recently been proposed in a theoretical study of the temporal decay of a single cluster [Ros]. In the ideal situation of an isolated cluster, the time dependence of its decay is found to be related to the cluster environment, with  $n = 1/2$  describing the case of an adatom island on top of a larger adatom island and  $n = 1/3$  describing the case of an adatom island inside a larger vacancy island. The system investigated in the present study, however, is hardly interpretable in the framework of the above mentioned model because of the high vacancy island density.

According to the model presented above, the mass transport is the result of two processes, the adsorption/desorption of monovacancies at the vacancy island edges and the diffusion of monovacancies on the surface. This approach implicitly assumes that the mass transfer happens via exclusive intralayer diffusion of monovacancies detaching from smaller holes and reabsorbing at larger ones. A priori, a second mechanism should be considered: a mass transport mediated via diffusing Au adatoms at the upper terrace which are emitted through uphill interlayer diffusion at the larger holes and reincorporated (downhill interlayer diffusion) at the edge of smaller ones. However, in the temperature range in which the vacancy islands ripening is observed ( $T < 350$  K), the latter possibility can be excluded because the emission channel will not be populated due to the high energy barrier for the uphill interlayer diffusion [Kel94A]. This leads to the conclusion that the hole coarsening process is the result of intralayer diffusion of vacancies.

A second basic assumption present in the previous analysis is the fact that vacancies are neither generated (which means zero flux deposition in the

reversed cluster ripening case) nor eliminated during the process. As no extra vacancies form after the completion of the thiol monolayer, the first condition is fulfilled. Regarding the elimination of vacancies, it may happen that, in regions near the steps, some pits are lost because they merge with the step edges. These events can be neglected by excluding regions with steps from the analysis. In these conditions, the requirement of the conservation of the total vacancy islands area is guaranteed.

The thermal behavior of alkanethiol monolayers on gold was studied by performing isothermal STM measurements at elevated temperatures (320-360 K). These experiments were done under controlled atmosphere by continuously flushing the microscope compartment with dry nitrogen gas. Three different chain length thiols, hexanethiol, decanethiol and octadecanethiol, have been examined.

Fig. 4.1 shows a time-lapse sequence of STM images characterizing the initial healing of a decanethiol-covered Au(111) surface. The sample was heated in-situ to 345 K and the images were acquired at that temperature. Fig. 4.1a,b,c, show the same area of the surface 31, 43 and 52 min after raising the temperature. The images were recorded in the differential mode, which means that the derivative of the line of constant current is recorded. Typical tunneling parameters were 1 V and 0.5 nA. As can be inferred from the comparison between the three images, the number of vacancy islands decreases with time, while the average hole size increases. In the absence of annihilation at steps the total defect area remains constant as can be shown by an analysis on sufficiently large terraces far away from substrate steps (Fig. 4.1). Similar sequences of images have been obtained on hexanethiol and octadecanethiol monolayers. It should be noted that the observed mass transport is not an artifact caused by tip scanning as indicated by the fact that regions

a)  $t = 31$  minb)  $t = 43$  minc)  $t = 52$  min

Fig. 4.1 Temporal development of the morphology of a decanethiol-covered Au(111) surface during annealing at 345 K. Tunneling parameters:  $I = 0.5$  nA,  $V = 1.0$  V.

which have not been subjected to repeated imaging show the same behavior.

In the following the results of a quantitative analysis of the vacancy island growth kinetics for Au(111) surfaces covered with hexane-, decane- and octadecanethiol monolayers are presented. All the data were taken from surface regions where no annihilation of defects occurred. The graph of Fig. 4.2a refers to data obtained on a hexanethiol monolayer and reports, in logarithmic scale, the average vacancy island area  $A$ , in arbitrary units, vs. the observation time (in min), whose origin is chosen at the moment of the temperature raising. The dependence of  $\ln(A)$  on  $\ln(t)$  is linear with a unitary angular coefficient. This means that the average pit size scales with time according to the power law  $r \propto t^n$ , with  $n=0.48\pm 0.10$ . The same analysis performed on different hexanethiol-samples gave results in the range 0.4-0.6. Analogous results were obtained on decane- and octadecanethiol monolayers. The graphs in Fig. 4.2b and c contain the data obtained from two series of images of decane- and octadecanethiol covered Au(111), yielding exponents of  $n=0.52\pm 0.07$  and  $0.49\pm 0.08$ , respectively.

On the basis of the above-mentioned model, the observed growth kinetics with exponent  $n=1/2$  suggests that, independently of the chain length, the intralayer mass transport of the vacancy islands at thiol covered Au(111) surfaces is a process governed by the adsorption/desorption rate of monovacancies at the pit edges. It is interesting to note that an analogous behavior was found for the coarsening of clusters of adatoms and vacancies created on a Au(111) surface by applying tip voltage pulses in moderate vacuum conditions or in air [Pea92]. Also in that system the adsorption/desorption rate of adatoms (vacancies) at the cluster (hole) edges was found to be the rate determining process.

So far, the kinetics of the hole ripening has been analyzed and it is found to be the same for the different thiol chain lengths examined.

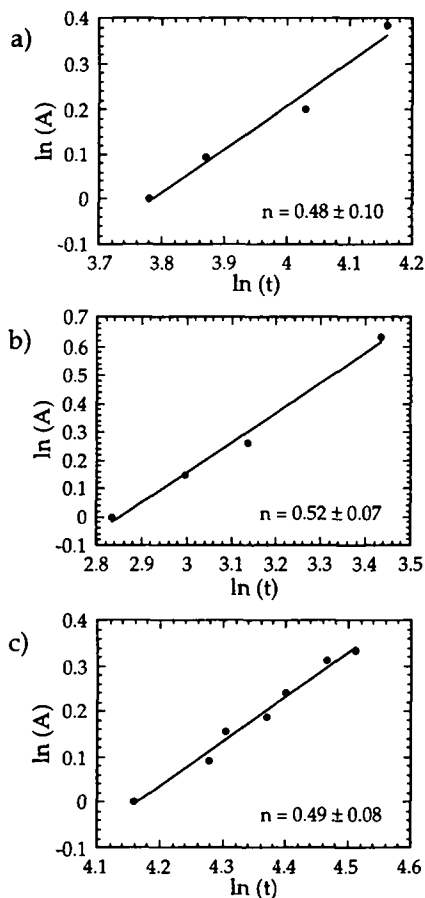
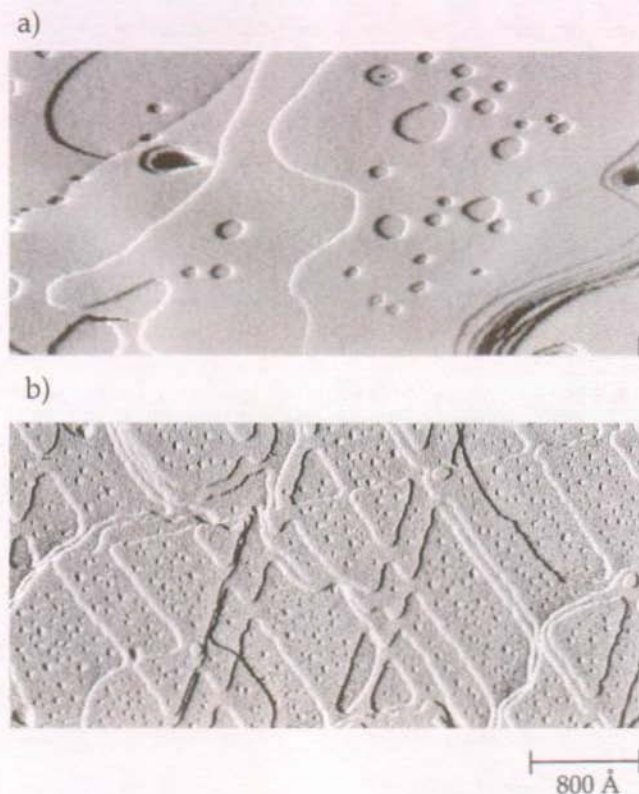


Fig. 4.2 Temporal variation of the average vacancy island area of alkanethiol-covered Au(111). a) hexanethiol, annealing temperature 325 K, b) decanethiol, annealing temperature 350 K, c) octadecanethiol, annealing temperature 345 K.

Although the kinetic law of the vacancy islands growth does not depend on the thiol chain length, the mass flow rate has been found to be chain length dependent. Fig. 4.3 shows a hexanethiol- (Fig. 4.3a) and an octadecanethiol- (Fig. 4.3b) covered Au(111) surface, which have been annealed at the same temperature (345 K) for the same time (60 min). As can be easily inferred from the comparison of the two images, which are equal in size, the healing process



**Fig. 4.3** Morphology of a hexanethiol- (a) and octadecanethiol- (b) covered Au(111) surface after 60 min of annealing at 345 K. Faster mass transport is observed on Au(111) surfaces covered by shorter chain monolayers. Tunneling parameters: a)  $I = 0.5$  nA,  $V = 1.0$  V; b)  $I = 0.4$  nA,  $V = 1.2$  V.

has been faster on the hexanethiol than on the octadecanethiol covered gold surface. In Fig. 4.3a the growth of the vacancy islands has already largely developed and the surface presents a low density of large pits, while in Fig. 4.3b the surface is still characterized by a high density of small pits. This shows that the mass transport is faster on gold surfaces covered with shorter chain monolayers. This observation is confirmed by an UHV STM study [Poi95] of butanethiol-covered Au(111) surfaces. With these very short chain



monolayers, the surface mobility is even higher and a vacancy island coarsening consistent with an Ostwald ripening mechanism is observed already at room temperature with time scales of hours. In the present study no pit motion has been observed at room temperature on octadecanethiol samples over several hours, while some minor changes have occasionally been observed on hexanethiol modified surfaces. In the UHV work [Poi95] the vacancy island coarsening is found to be related to the order in the monolayer: the growth of larger holes at the expense of smaller ones which eventually disappear is accompanied by the increase of the fractional area of the surface occupied by ordered molecular domains (it should be noted that the coexistence of poorly ordered regions with well organized domains has been reported for short chain thiol monolayers [Poi94B]).

An increase of the monolayer order is observed also during annealing. Fig. 4.4 shows two images of the same region of a decanethiol monolayer which were acquired while keeping the sample at 360 K. The image in Fig. 4.4b has been recorded 20 minutes after the one in Fig. 4.4a. In both images, boundaries between different adjacent molecular domains, which are imaged as depressed darker lines, are easily identified. As inferred from the comparison of the two pictures, domain walls are highly mobile at this temperature and during the annealing some boundaries disappear giving rise to larger molecular domains. While the average domain size had initially (Fig. 4.4a) been of the order of 100-200 Å, it increased substantially upon annealing. In the final state (Fig. 4.4b) the domains reach sizes as large as 500-600 Å. The increase of the average domain size has been reported also in a x-ray diffraction study [Fen93] on the basis of the substantial reduction of the width of the  $(\sqrt{3}\times\sqrt{3})R30^\circ$  diffraction peaks of dodecanethiol monolayers after annealing.

The reorganization of the monolayer order which causes the increase of the molecular domain size is an important element to be considered when

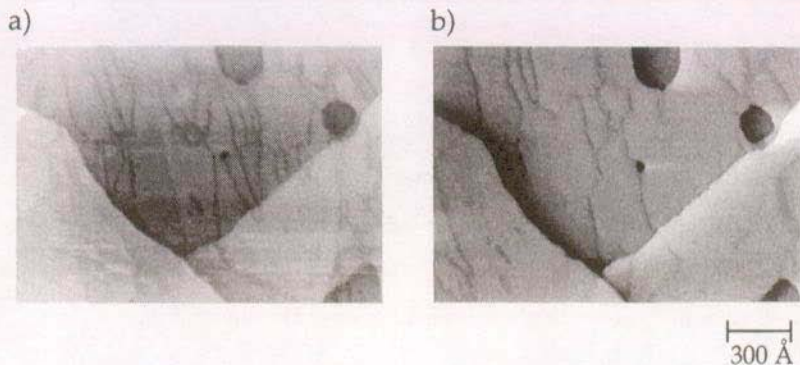


**Fig. 4.4** Mobility of domain boundaries of a decanethiol-covered Au(111) surface at 360 K. (b) was recorded 20 min after (a). Tunneling parameters:  $I = 0.1$  nA,  $V = 1.0$  V. The image in (a) was recorded in the absolute mode (i.e. the constant current line is recorded) whereas the image in (b) was recorded in the differential mode (i.e. the derivative of the constant current line is recorded).

discussing the molecular mechanism involved in the mass transport at the thiol/gold interface. Two different pictures can be figured out, namely a movement of the upper layer gold atoms underneath a static thiol monolayer or a migration of gold atoms accompanied by some thiol reorganization. The observed reorganization in the monolayer would account for the second scenario with a participation of molecules in the process. Such a picture additionally agrees with the observed dependence of the mass transport rate on the thiol chain length. Longer thiols are characterized by higher interchain van der Waals interactions which hinder the molecule displacement. As the mass transport depends on chain length and the adsorption/desorption of monovacancies at pit edges is the limiting factor of the mass flow, the monovacancy formation/elimination depends on the molecule length. This is a reasonable consequence of the rearrangement of thiols involved in the adsorption/desorption events which necessarily perturb the interchain interactions.

The occurrence of thiol displacement during the mass transport process is confirmed by a recent study on SAMs of asymmetric disulfides that contain hydrocarbon and fluorocarbon chains [Ish97]. Upon annealing at 370 K, these monolayers undergo a phase separation resulting in the formation of hydrocarbon domains and fluorocarbon domains. The observation of separated phases is evidence for the occurrence of disulfide cleavage (see also [Bie93]) as well as for the occurrence of molecule diffusion during the annealing.

The observation of mass transport at the thiol/gold interface in a temperature range in which no surface mobility is observed on bare gold in UHV together with the results of Peale et al. [Pea92], who analyze the mass transport process on clean and adsorbate covered gold surfaces, indicate that the presence of the monolayer increases the mobility at the gold surface. The increase of the self-diffusion coefficient on metal surfaces in the presence of adsorbates has been reported to be up to 4 orders of magnitude [Per67]. A higher surface mobility in the presence of adsorbates has also been observed in the electrochemical environment [Gao93, Mól95, Tre89]. In this case the mobility at the surface is related to the degree of adsorption of anions: more strongly adsorbed anions induce higher surface mobility. These observations are explained in terms of the weakening of substrate-substrate bonds due to the bonding of surface atoms to the adsorbate which results in an increased substrate mobility. This is not surprising in the case of thiol monolayers on gold because of the strong S-Au bond [Dub92]. More specifically, in the case of thiol/gold interfaces as well as in the case of "adsorbate contaminated" gold surfaces [Pea92], as the mass flow is limited by the monovacancy (adatoms) detachment rate, the adsorbate is likely to promote the creation of monovacancies (adatoms) at step edges. In the case of gold in air [Pea92] adsorbates were present on the surface because of the exposure to air, but their nature was not controlled. For thiol/gold interfaces, on the other hand, the adsorbate can be modified in a controlled way by varying the molecule chain length. This allows to point out the

presence of a second competing effect, the tendency of interchain van der Waals interactions to slow down the mass transport by promoting monolayer order and compactness.

### 4.3 Final stage of the annealing: coalescence and annihilation

The kinetic analysis presented above included only data obtained at annealing temperatures  $T \leq 350$  K and annealing times below about 90 min in order to minimize the influence of coalescence. Deviations are expected from the power-law coarsening kinetics when coalescence dominates or substantially contributes to the dynamics of the system. In the present experiments coalescence was found to be negligible in the initial healing stage. Only in the late stage, it became increasingly important. Indeed, it is only the dynamic coalescence and the dynamic annihilation of pits at preexisting steps which render the complete healing of the vacancy defects possible. This is illustrated in Fig. 4.5 for octadecanethiol covered Au(111). The two STM images show the late stage evolution of the film morphology after 90 min (a) and 110 min (b) of annealing at 370 K. On the left hand side (arrow 1) several vacancy islands on the topmost gold layer are annihilated at preexisting Au(111) step edges. On the low terrace on the right hand side (arrow 2) one can notice the coalescence of neighboring vacancy islands. Coalescence and annihilation events have usually been observed at temperatures above the temperatures at which the Ostwald ripening of vacancy islands was followed. Because of the variability between different samples no precise distinction between a temperature range characterized by the ripening mechanism and a temperature range characterized by coalescence and annihilation can be given. What has been observed is a general lowering of the temperature at which the different processes become operative when monolayers formed by progressively

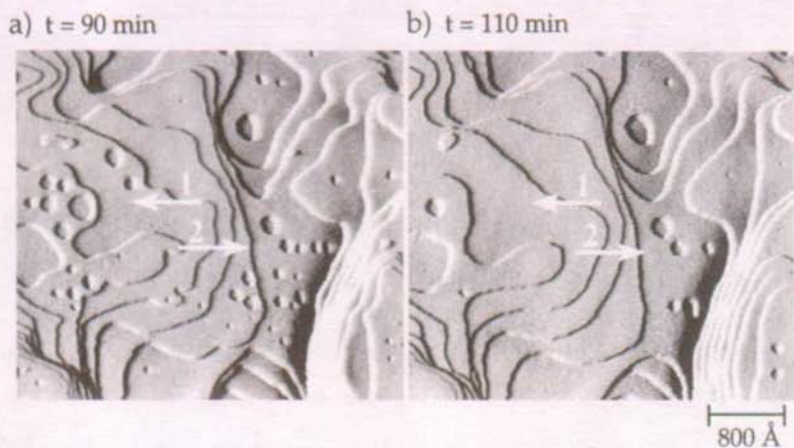


Fig. 4.5 Edge annihilation and coalescence in the late stage evolution of vacancy islands on an octadecanethiol-covered Au(111) sample during annealing at 370 K. The sample has been annealed for 90 min (a) and 110 min (b). Tunneling parameters:  $I = 0.5$  nA,  $V = 1.3$  V.

shorter chains are investigated. The sample-to-sample variability not only in the thermal behavior, but also in the structural properties of thiol monolayers, namely molecular structures and hole density/size, which has been observed in this study, appears to be a rather general characteristic of these monolayers which has been reported also by other groups [Cam94, Cam97, Son94B].

A general aspect which has to be taken into account when studying organic layers with STM is the possible influence of the tip on the structure of the layer. This problem becomes increasingly important at elevated temperatures: the higher the temperature, i.e. the higher the surface mobility, the stronger the influence of the tip. Particular attention has to be paid in the case of long chain monolayers which, because of the larger thickness, interact more strongly with the STM tip. An example of tip induced mobility on an octadecanethiol monolayer is shown in Fig. 4.6. Both images were acquired at 360 K. The image in Fig. 4.6a was recorded after repeated scans on the same region while the

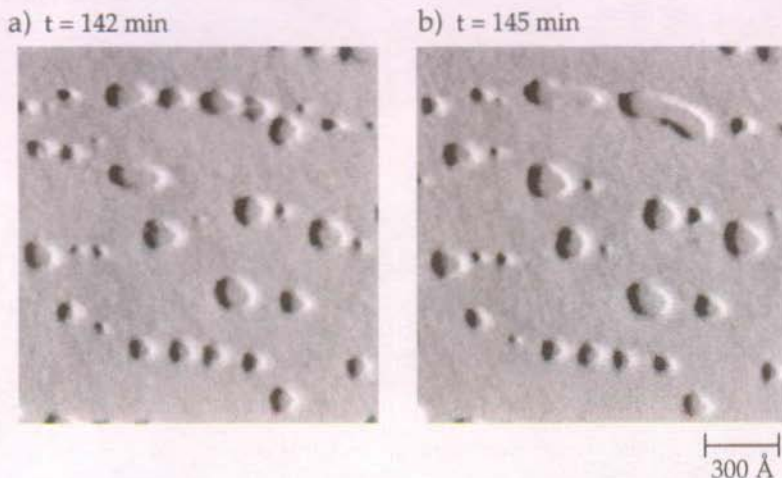


Fig. 4.6 Tip-induced mobility at an octadecanethiol-covered Au(111) surface at 360 K. Tunneling parameters:  $I = 1.0 \text{ nA}$ ,  $V = 0.9 \text{ V}$ .

image in Fig. 4.6b was recorded two images after the one in (a). In Fig. 4.6a it is possible to observe an alignment of the pits along the horizontal direction which is the fast scan direction of the STM tip as well as an elongation of some holes along the same direction. Fig. 4.6b shows two coalescence events which are again related to the tip induced surface mobility. Such situations have of course been excluded from all previous analyses.

#### 4.4 Towards desorption

So far the morphological transformations at the thiol/gold interface associated with the thermal annealing have been discussed. In the temperature range at which the experiments described above were performed no substantial evaporation of thiol molecules has been observed. Only in some cases, at about 370 K, as already discussed in chapter 3, a transformation from the full coverage  $c(4 \times 2)$  molecular structure to the less dense striped structure has been

observed on decanethiol monolayers. That kind of transformation resulted, however, in a less dense, but uniform monolayer covering the whole surface.

A more dramatic transformation of the thiol monolayers happens upon annealing at about 380-390 K: at these temperatures thiol desorption begins (in passing it has to be noted that the desorption product is unknown). The onset temperature for desorption depends on chain length, increasing with increasing length. As already mentioned, however, a certain variability between individual samples has been observed. Fig. 4.7 shows an image recorded at room temperature on a decanethiol-covered gold surface after annealing at 385 K for 8 hours. No more gold vacancy islands are present at the surface. The image interestingly shows that desorption does not occur uniformly at the surface, but proceeds in patches, with the surface being characterized by regions still covered by a compact molecular layer surrounded by regions of a highly disordered partially desorbed layer. Closer inspection of the compact areas showed the presence of the  $c(4 \times 2)$  structure: in this case the transition to the striped structure that, as discussed chapter 3, is usually observed in decanethiol monolayers after annealing at 370 K did not occur. This further illustrates the sample-to-sample variability observed in the thermal behavior of alkanethiol monolayers.

Together with domain boundaries, some small pits are visible in the compact layer patches, which likely represent the very initial stage in the "growth" of new regions of a partially evaporated monolayer. The fact that desorption happens in spreading patches is reasonably explained from the energetic point of view: the desorption of a molecule from a region of an already partially evaporated monolayer (i.e. weakened van der Waals interactions because of a not optimized chain packing) is energetically favored over the desorption of a molecule embedded in a well ordered and compact monolayer (i.e. optimized interchain interactions).



Fig. 4.7 Partially desorbed decanethiol monolayer after 8 hours of annealing at 385 K. Tunneling parameters:  $I = 0.2$  nA,  $V = 1.0$  V.

Further heating of the sample results in a surface characterized by a disordered molecular layer with no more compact areas as reported also by another STM study in air [Del94B]. Annealing at 573 K in UHV has been observed to result in complete thiol desorption, leaving a clean and reconstructed Au(111) surface [Cam94] (at this temperature the mobility even of the bare gold surface is sufficiently high to allow the formation of the reconstruction).

## 4.5 Conclusions

The growth kinetics of vacancy islands created during the self-assembly of thiol monolayers on Au(111) surfaces has been studied by performing isothermal STM measurements at elevated temperature. The observed growth kinetics is consistent with an Ostwald ripening mechanism governed by the adsorption/desorption of monovacancies at pit edges. While the growth law



(i.e. the growth mechanism) has been found to be independent of the thiol chain length, the actual growth rate is found to be chain length dependent, with faster mass transport being observed on surfaces covered by shorter chain monolayers. The lower mass transport rate observed on surfaces covered by long chain thiols can be explained by the more compact structure of long thiol monolayers due to the higher van der Waals interactions. In the latest stage of growth, hole coalescence is found to become increasingly important. At the molecular scale, annealing induces a reorganization in the monolayer order with a substantial increase of the ordered domain size. Further heating above 380-390 K triggers a desorption process.

## Chapter 5

# Cu electrodeposition on alkanethiol covered Au(111) electrodes

### 5.1 Introduction

Over the past years, there has been an increasing interest in developing methods for the precise control of the growth morphology of thin epitaxial films on the microscopic scale [Röd93, Ros95]. The basic goal of epitaxial film growth, in vacuum as well as in solution, is the growth of flat, defect-free films of specified crystallographic surface orientation. Several approaches have been developed to grow such films with smooth and abrupt interfaces. A particularly appealing method to manipulate the growth kinetics and to force a smooth layer-by-layer growth is the deliberate introduction of impurities, so-called surfactants or additives. While their use in molecular beam epitaxy has only recently been explored [Cop89], it has been for a long time common knowledge in the metal plating industry that certain organic compounds, there

known as leveling or brightness agents, added to the plating bath will favor smooth electrodeposition [Des83, Nic92].

In this chapter, an alternative approach for the microscopic control of the electrocrystallization of metals, based on the chemical modification of the electrode surface, is presented. Self-assembled monolayers (SAM) have been advantageously used in electrochemistry to obtain well ordered and defined electrochemical interfaces which have found applications in basic and applied research fields, from charge transfer to corrosion inhibition [Fin96]. Although the possibility to use these organic films to manipulate and control the electrocrystallization of metals on the electrode surface suggests itself, this aspect is almost unexplored.

Here, the knowledge gained about the structure and properties of thiol monolayers on Au(111) has been employed to prepare gold electrodes modified in a controlled way by varying the thiol chain length. Copper has been deposited on Au(111) electrodes covered with a thiol layer. The electrodeposition of Cu has been investigated by cyclic voltammetry (CV), an integral technique averaging over the whole sample, and by in-situ electrochemical scanning tunneling microscopy (STM), a local technique. In a first step, the process has been explored at room temperature. As will be clear from the presentation of the STM results, the systematic control of the electrode potential and SAM thickness enables to manipulate the growth morphology. In a second step, an additional control parameter, the temperature, has been introduced. Obviously, working in liquid does not allow to vary the temperature over the wide range usually explored in gas phase deposition in vacuum. Moreover, some technical problems, like electrolyte evaporation, have to be taken into account. This probably explains why very little fundamental research in this direction has been done up to now. In the present work, the choice of a proper electrolyte enabled to study the electrodeposition of Cu from

room temperature up to 350 K: a range wide enough, as will be shown later, to demonstrate the profound influence of temperature on the process.

After a brief introduction concerning the different regimes of thin film growth, the presentation of the results will start with a discussion of the electrochemical deposition of Cu on bare Au(111) electrodes. This serves as an important base of comparison in order to analyze the role of the thiol layer in controlling the deposition. The room temperature measurements of Cu electrodeposition on thiol/gold electrodes will then be presented. The organic layer substantially modifies the electrodeposition. The different growth scenarios obtained by varying chain length and electrode potential will be described. Finally, the results of the higher temperature experiments will be analyzed. To conclude this chapter, possible mechanistic and structural models for the Cu/thiol/gold system will be discussed.

## **5.2 Thin film growth: thermodynamics vs. kinetics**

In thermodynamic equilibrium, all atomic processes proceed in opposite directions at equal rates, as required by consideration of the "detailed balance" principle. This implies, for example, that deposition of atoms from the solution (or from the gas phase in the case of film growth in vacuum) and desorption of atoms as well as growth and decay of two-dimensional islands must occur at the same rates. As a consequence, there is no net growth at the surface. The system can be described by unchanging macroscopic parameters like coverage or surface roughness. Statistical fluctuations around these equilibrium quantities due to the various atomic processes characterize the system on the microscopic level. For growth to occur, the system must be more or less far away from equilibrium. Depending on how far from equilibrium growth

proceeds, the morphology of the deposited film will be determined by thermodynamic quantities, such as surface and interface free energies, or controlled by kinetics of the involved processes, e.g. adatom diffusion, nucleation and aggregation.

A criterion to distinguish between growth occurring close to a thermodynamic or in a kinetic regime is based on the evaluation of the adatom (or adion) surface diffusion coefficient  $D$  vs. the deposition rate  $R$ . Even if simplistic, it intuitively helps to understand the interplay between the different variables which govern growth. The higher the  $D/R$  ratio, the closer is the system to the thermodynamic regime (the diffusion coefficient  $D$  considered here includes all the diffusion events occurring at a surface like terrace, interlayer, exchange and edge diffusion). For a given system in vacuum,  $D$  is essentially determined by temperature. The situation is more complex in the electrochemical environment. In this case, the presence of coadsorbed ions or molecules play a role in determining the effective surface diffusion coefficient. Another important element to consider is the atom desorption and re-adsorption due to the exchange current<sup>1</sup> which affect the adion surface mobility. Either large values of the surface diffusion coefficient or high exchange current density (vs. the deposition rate) are a basic requirement for near equilibrium growth.

Based on thermodynamic arguments, thin film growth can be classified into three growth modes, as shown in Fig. 5.1. They result from the interplay between metal-metal (Me-Me) and metal-substrate (Me-S) interaction energies

---

<sup>1</sup> At equilibrium, the net current is zero, but an anodic  $i_a$  and a cathodic current  $i_c$  which balance each other exist at the electrode/electrolyte interface. This balanced faradaic activity can be expressed in terms of the exchange current  $i_0$ , which is equal in magnitude to either component current  $i_a$  or  $i_c$ .

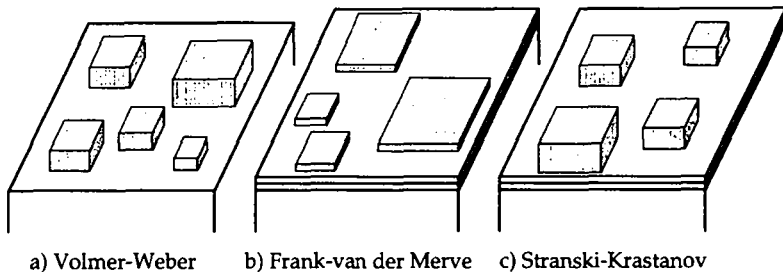


Fig. 5.1 Schematic representation of the three thermodynamic growth modes: a) three-dimensional growth, b) two-dimensional growth, c) hybrid case of three-dimensional island formation after layer-by-layer growth of one or several monolayers.

as well as strain energy due to metal-substrate crystallographic misfit. High Me-Me interaction energies, with respect to Me-S, and high Me-S lattice misfit favor the 3D island growth of Fig. 5.1a, which is an usually unwanted situation because it gives rise to rough and poorly defined interfaces. The opposite case, the layer-by-layer growth mode shown in Fig. 5.1b, is characteristic of strong interactions and low misfit between Me and substrate and results in smooth, abrupt interfaces. The intermediate case (Fig. 5.1c), island growth on pre-deposited mono-/multilayers, is usually encountered when the Me-S interaction is high compared to the Me-Me one, but metal and substrate have a non-negligible lattice misfit which, after one or a few monolayers, forces the metal to grow three-dimensionally. A further important element to be considered in the case of metal electrodeposition is coadsorption. Ions (usually anions) or even molecules can coadsorb on the surface. Hence, a further interaction, the metal/coadsorbate one, has to be considered. Depending on the strength of this interaction, the presence of coadsorbates can modify the metal growth mode.

The growth regime opposite to the nearly equilibrium scenario described above is encountered for low values of the D/R ratio. In high supersaturation conditions, growth is largely determined by kinetics. In this regime, through the control of the atomic processes occurring at the surface, one can manipulate the morphology of the thin film. Events like terrace, interlayer, exchange and edge diffusion are thermally activated processes. The possibility to activate or deactivate certain diffusion events by varying the substrate temperature has been exploited in molecular beam epitaxy (MBE) in vacuum to assemble nanostructures of controlled morphology [Röd93]. Working in electrolyte limits the range over which temperature can be varied, but prompts the use of an alternative method to control surface diffusion processes, i.e. the deliberate introduction of additives. The results presented in the following paragraphs show how the growth of thin metallic films can be manipulated also in the electrochemical environment when pre-adsorbed thiols act as additives.

As described in the next paragraph, at moderate deposition rates (i.e. low deposition currents), Cu growth on Au(111) occurs in a nearly thermodynamic regime and is characterized by a Stranski-Krastanov growth mode. This can be explained in term of the above-mentioned D/R criterion: because of the high exchange current for  $\text{Cu}/\text{Cu}^{++}$  <sup>1</sup> the effective surface mobility is high. Hence, the thermodynamic regime (high D/R ratio) is achieved. A different scenario characterizes the Cu deposition on thiol-covered electrodes. As will be discussed in paragraphs 5.4 and 5.5, the thiol layer strongly reduces the charge transfer across the interface. This is likely to limit the exchange current and, consequently, to reduce the effective Cu surface mobility. In these conditions, Cu growth is mainly governed by kinetics. It is quite remarkable that, as shown

---

<sup>1</sup> An exchange current  $i_0$  of  $500 \mu\text{A}/\text{cm}^2$  is found for  $\text{Cu}/\text{Cu}^{++}$  at equilibrium [Taf66].

in paragraphs 5.5 and 5.6, nucleation followed by diffusion limited aggregation and coalescence (the well known scenario for the kinetic growth regime in MBE in vacuum) characterizes the Cu electrocrystallization on covered electrodes. The similarity with epitaxial growth in vacuum can be rationalized by taking into account that, because of the low exchange current, copper adion desorption is likely to be negligible and an almost hit-and-stick mechanism, similar to the UHV scenario, is probably operative.

### 5.3 Cu electrodeposition on Au(111)

The electrodeposition of Cu on thiol covered Au(111) electrodes has been chosen because of the great amount of data available for the Cu/Au(111) system [Bor94, Hac91, Hai94, Höl94, Mag91, Nic91, Ton95] which represents a valuable base of comparison in order to point out the effect of the organic layer on the electrocrystallization.

When discussing the electrodeposition of a metal (Me) on a foreign metallic substrate (S) two different potential ranges can be distinguished, namely electrode potentials positive or negative of the equilibrium Nernst potential for the reduction/oxidation reaction:  $\text{Me}^{z+} + z e^- \leftrightarrow \text{Me}$ . Some Me/S systems are characterized by a metal deposition already at potentials positive of the equilibrium potential, a phenomenon known as underpotential deposition (UPD), explained by a Me-S interaction energy higher than the Me-Me one. On the other hand, a Me-S interaction weaker than the Me-Me one favors the occurrence of deposition at potentials negative of the Nernst potential, which is referred to as overpotential deposition (OPD).

Cu electrodeposition on the bare Au(111) surface is characterized by the Stranski-Krastanov growth mode (Fig. 5.1c). Underpotential deposition occurs and, as shown in the scheme in Fig. 5.2 which reports the Cu coverage vs. the



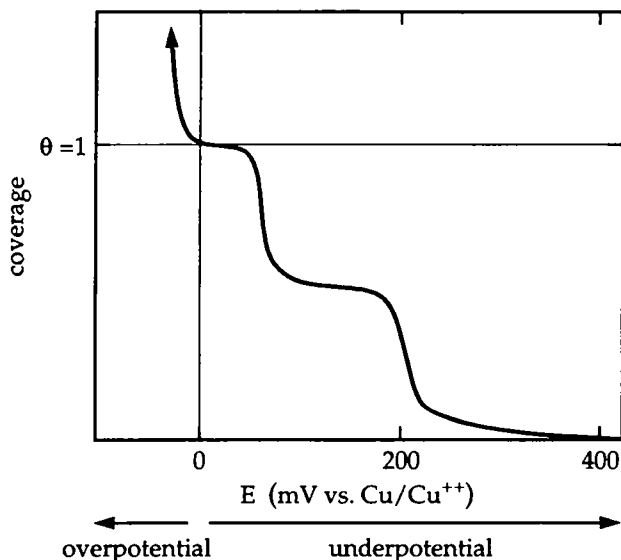


Fig. 5.2 Cu coverage as a function of the potential of the Au(111) electrode (from [Höl94]). One monolayer of Cu is deposited at potentials positive of the Nernst value. At negative potentials, bulk deposition of Cu occurs.

electrode potential, one monolayer of Cu is deposited at potentials positive of the Nernst value. The electrodeposition can be monitored by recording the electrochemical current during a potential sweep over the region of interest. Such a curve is reported in Fig. 5.3 for a Au(111) electrode in a Cu containing electrolyte (50 mM H<sub>2</sub>SO<sub>4</sub> + 1 mM CuSO<sub>4</sub>). The main feature of the cyclic voltammogram of Fig. 5.3 is the presence of four peaks, two corresponding to deposition (A and B) and two to desorption (A' and B') of Cu. The current at potentials positive of the first deposition peak A is the so-called double layer current which results from the charging of the double layer (see paragraph 1.2) due to the polarization of the electrode. In the decreasing (cathodic) potential scan different stages in the Cu deposition are encountered. In a 100 mV wide

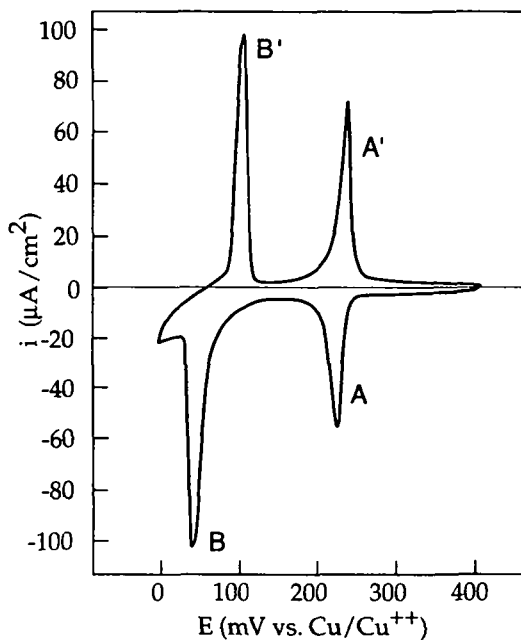


Fig. 5.3 Cyclic voltammogram for Au(111) in 50 mM  $\text{H}_2\text{SO}_4$  + 1 mM  $\text{CuSO}_4$  showing the UPD of Cu. Scan rate: 10 mV/s.

potential window positive of the first UPD peak, Cu is randomly adsorbed up to a limiting coverage of 15% of a monolayer [Höl94]. Proceeding in the cathodic scan, the first UPD peak, A, is passed at about 200 mV and corresponds to the transition from the randomly adsorbed Cu to a  $(\sqrt{3}\times\sqrt{3})\text{R}30^\circ$  adlayer. This honeycomb  $(\sqrt{3}\times\sqrt{3})\text{R}30^\circ$  Cu overlayer with coadsorbed sulfate ions in the centers (as shown in Fig. 5.4 [Ton95]) is stable in the potential region between peak A and B. The model in Fig. 5.4 agrees well with the adlayer structure observed by STM and AFM [Man91, Hac91, Hai94A, Hai94B, Mag91]. The second peak B corresponds to the transition from the

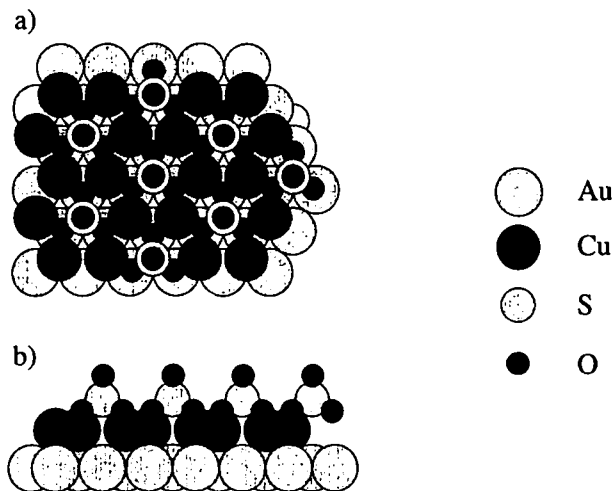
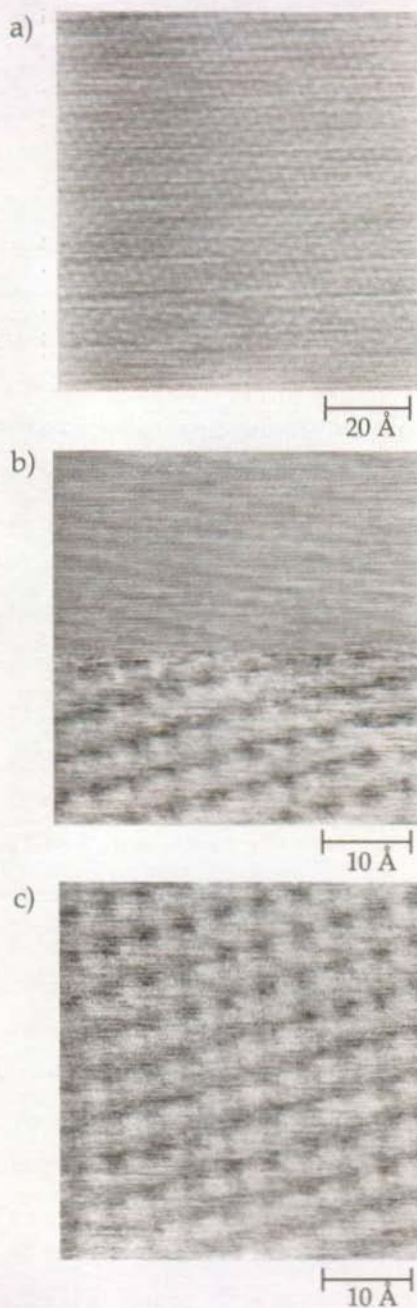


Fig. 5.4 Interfacial structure of Cu/Au(111) in the potential range between peaks A and B. a) Top view, b) Side view. Cu forms a  $(\sqrt{3}\times\sqrt{3})R30^\circ$  honeycomb adlayer with coadsorbed sulfate anions occupying the six-fold coordinated open sites of the honeycomb structure (from [Ton95]).

$(\sqrt{3}\times\sqrt{3})R30^\circ$  to a (1x1) overlayer. The presence of two distinct peaks clearly shows that the deposition takes place in two energetically well-separated steps. Reversing the scan direction, the two corresponding stripping peaks, B' and A', are observed. Decreasing the potential negative of the Nernst potential, a large current due to the bulk deposition of Cu builds up; returning to positive values, the bulk Cu is stripped in a rather narrow peak close to the Nernst potential.

In the present work, Cu UPD on Au(111) has been used as a reference in order to check the reliability of the experimental setup. Moreover, since for the electrochemical deposition at elevated temperatures, a non-standard electrolyte had to be used to prevent evaporation, the deposition of Cu on Au(111) in this

electrolyte has been studied in order to check if the process was influenced by the change in the solvent. No major changes are introduced by the new electrolyte and the usual behavior is observed by cyclic voltammetry as well as by STM. Fig. 5.5 refers to the Cu deposition on Au(111) in 50 mM  $\text{H}_2\text{SO}_4$  + 1 mM  $\text{CuSO}_4$ , with the solvent being a 2:1 mixture of  $\text{HOCH}_2\text{CH}_2\text{OH} : \text{H}_2\text{O}$ . Fig. 5.5a shows an atomic resolution image of the Au(111) surface at 400 mV vs. Cu/Cu<sup>++</sup>. No Cu is deposited on the surface at this potential and the gold lattice is imaged. Decreasing the potential below the first UPD peaks induces the formation of the  $(\sqrt{3}\times\sqrt{3})\text{R}30^\circ$  adlayer as shown in Fig. 5.5b. The image is downward-rastered with the electrode potential being stepped from 300 mV to 150 mV just below the middle of the image. As can be seen from the comparison of the two halves of the image a rapid formation of the  $(\sqrt{3}\times\sqrt{3})\text{R}30^\circ$  overlayer occurred. The subsequent scan is shown in Fig. 5.5c with the adlayer covering the whole surface. On the basis of the structural information obtained by X-ray diffraction [Ton95] and by the deposition charge evaluation [Höl94], the  $(\sqrt{3}\times\sqrt{3})\text{R}30^\circ$  structure imaged by STM can be interpreted as the results of the adlayer of coadsorbed sulfate anions occupying the six-fold coordinated central sites of the honeycomb structure with three of the oxygen atoms bonded to neighboring Cu atoms according to the model in Fig. 5.4. By increasing the electrode potential above the UPD peak, the gold lattice is imaged again. The transition from the random distribution of adsorbed Cu just above the UPD peak to the  $(\sqrt{3}\times\sqrt{3})\text{R}30^\circ$  adlayer happens in rapidly spreading islands [Hac91, Höl94, Mag93]. Because of this spreading mechanism different domains in the overlayer can form. An example of a stacking fault boundary between domains translated by one gold atomic distance is shown in Fig. 5.6 in which the domain in the left part of the image is shifted with respect to the domain occupying the major right portion of the image. Decreasing the potential below the second UPD peak induces the transition to the (1x1) phase. Also the transition at the second UPD peak



**Fig. 5.5** In-situ electrochemical STM image sequence showing the formation of the  $(\sqrt{3}\times\sqrt{3})R30^\circ$  honeycomb structure when the electrode potential is decreased below the first UPD peak. Tunneling parameters:  $I = 15$  nA,  $V = 0.01$  V. Electrolyte: 50 mM  $H_2SO_4$  + 1 mM  $CuSO_4$  with the solvent being a 2:1 mixture of  $HOCH_2CH_2OH : H_2O$ . a) Electrode potential: 400 mV vs.  $Cu/Cu^{++}$ . The gold lattice is imaged. b) The image was downward-rastered; the electrode potential was stepped from 300 mV (top) to 150 mV (bottom) vs.  $Cu/Cu^{++}$  just below the middle of the image. The  $(\sqrt{3}\times\sqrt{3})R30^\circ$  structure forms within a few seconds (the whole image was scanned in 30 s). c) Successive image showing a fully developed  $(\sqrt{3}\times\sqrt{3})R30^\circ$  adlayer. Electrode potential: 150 mV vs.  $Cu/Cu^{++}$ . The bright spots are due to coadsorbed sulfate anions according to the model in Fig. 5.4.

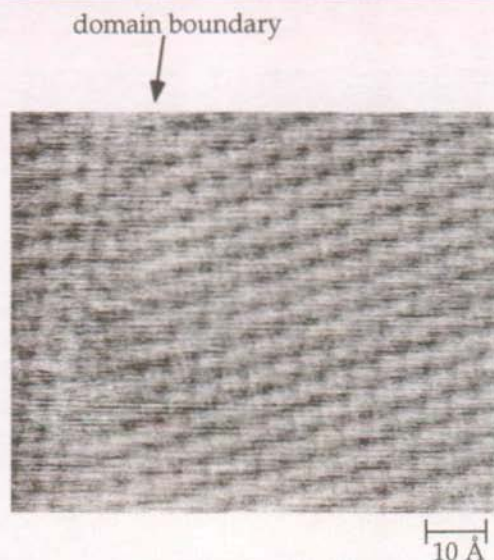


Fig. 5.6 In-situ electrochemical STM image showing a domain boundary between adjacent  $(\sqrt{3}\times\sqrt{3})R30^\circ$  domains. Electrolyte: 50 mM  $\text{H}_2\text{SO}_4$  + 1 mM  $\text{CuSO}_4$  with the solvent being a 2:1 mixture of  $\text{HOCH}_2\text{CH}_2\text{OH} : \text{H}_2\text{O}$ . Electrode potential: 150 mV vs.  $\text{Cu}/\text{Cu}^{++}$ . Tunneling parameters:  $I = 15$  nA,  $V = 0.01$  V.

proceeds via the formation of (1x1) islands spreading over the terraces [Mag93]. This is shown in the sequence of images reported in Fig. 5.7 which were taken along the second UPD adsorption peak on a Au(111) electrode immersed in the standard aqueous electrolyte. As the potential is stepped cathodically, the islands expand on the terraces to coalesce with other expanding islands. This observation is in agreement with the nucleation and growth scheme deduced by chronoamperometric (potential step) kinetic measurements of structural changes of the Cu UPD adlayer on Au(111) [Höl94]. Eventually, the transition is complete at 0 mV, near the threshold of bulk deposition (three dimensional growth). The STM contrast could arise from the presence of coadsorbed sulfate anions occupying positions on top of the Cu atoms in the (1x1) structure [Mel88] vs. their occupation of the open sites of the honeycomb adlayer in the  $(\sqrt{3}\times\sqrt{3})R30^\circ$  structure.

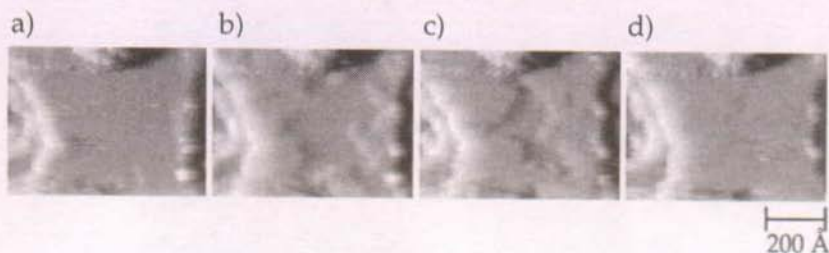


Fig. 5.7 In-situ electrochemical STM image sequence showing the transition from the  $(\sqrt{3}\times\sqrt{3})R30^\circ$  to the  $(1\times 1)$  phase of the Cu UPD on Au(111). Electrolyte: 50 mM  $\text{H}_2\text{SO}_4$  + 1 mM  $\text{CuSO}_4$ . Electrode potential: 50 mV (a), 40 mV (b), 10 mV (c) and 0 mV (d) vs.  $\text{Cu}/\text{Cu}^{++}$ . Tunneling parameters:  $I = 0.5$  nA,  $V = 0.05$  V.

After the completion of the first Cu monolayer, no further deposition occurs in the UPD range. Decreasing the potential below the Nernst equilibrium potential starts the bulk deposition of Cu. As shown in Fig. 5.8, a three-dimensional growth mode characterizes the OPD deposition of Cu on Au(111). Cu nuclei start to grow at step edges, dislocations and defects in the gold surface [Nic91, Nic92]. The large lattice misfit between Cu and Au (about 13%) favors the 3D growth mechanism.

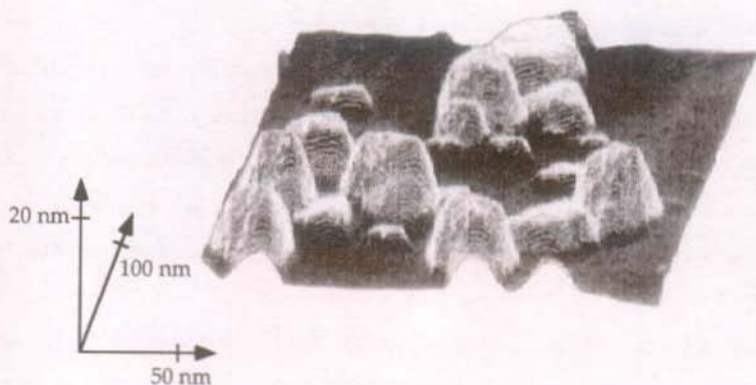


Fig. 5.8 In-situ electrochemical STM image showing the bulk copper deposition on Au(111). Electrolyte: 100 mM  $\text{H}_2\text{SO}_4$  + 1 mM  $\text{CuSO}_4$ . Electrode potential: -200 mV vs.  $\text{Cu}/\text{Cu}^{++}$ . Tunneling parameters:  $I = 10$  nA,  $V = 0.015$  V ([from [Nic92]).

So far the electrodeposition of Cu on Au(111) electrodes has been discussed. A Stranski-Krastanov growth mode, with one Cu monolayer deposited in the UPD region and 3D island formation in the OPD regime, is observed. The deposition process is found not to be affected by the use of the modified electrolyte employed in the higher temperature studies (see paragraph 5.6). The insight into the Cu/Au(111) behavior will serve in the following as a comparison to point out the effect of the thiol layer on the Cu electrocrystallization.

## **5.4 Cu electrodeposition on alkanethiol/Au(111) in the underpotential regime**

Modifying the electrode surface with an alkanethiol monolayer alters the deposition process completely as results from cyclic voltammetry as well as from STM measurements. Fig. 5.9 reports a current-potential curve for a Au(111) electrode covered by a decanethiol monolayer. It should be noted that some caution has to be used when referring to the potential of a metal electrode covered with a SAM. The presence of the organic layer renders the electrode/electrolyte interfacial structure more complicated because of the introduction of a new phase in between (see chapter 1.2). On the basis of double layer capacitance measurements on thiol covered gold electrodes, a potential drop across the layer linearly increasing with the chain length and depending on the chain terminal group has been proposed [Son94A, Son95B]. While the potential of the metal electrode is known and easily controlled, the actual potential at the thiol/electrolyte interface can only be roughly estimated. So all the potential values reported throughout this work are the potentials of the gold electrode. As can be inferred from the comparison with the cyclic voltammogram for bare gold given in Fig. 5.3, the thiol layer exhibits a



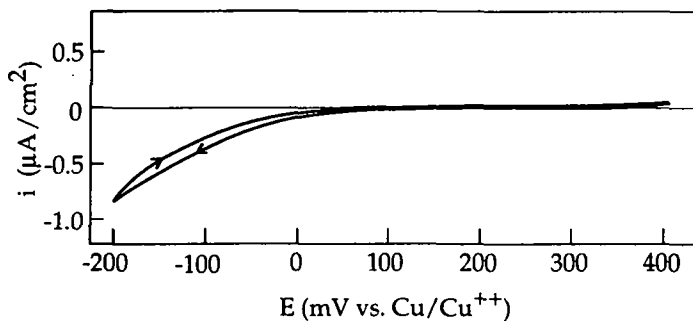


Fig. 5.9 Cyclic voltammogram for a decanethiol-covered Au(111) sample. Electrolyte: 50 mM  $\text{H}_2\text{SO}_4$  + 1 mM  $\text{CuSO}_4$ . Scan rate: 10 mV/s.

blocking behavior towards Cu deposition. There are two major differences between the two plots. Firstly, in the presence of the organic layer, the deposition and stripping peaks in the UPD region, which are characteristic of bare gold, disappear and, secondly, the measured electrochemical current in the double layer regime is one order of magnitude lower in the case of a covered electrode than for bare gold. These are general results which are valid independently of the thiol chain length, from hexanethiol up to octadecanethiol. More subtle differences in the CVs depending on the thiol chain length will be discussed in the next paragraph.

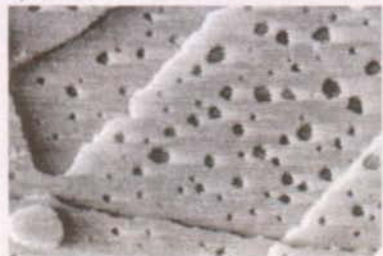
A first result has already been obtained from cyclic voltammetry: the thiol layer inhibits the deposition of copper. More structural information is given by the STM analysis. Fig. 5.10 shows the morphology of the decanethiol covered Au(111) surface at +50 mV vs.  $\text{Cu}/\text{Cu}^{2+}$ , i.e. just above the potential corresponding to the second UPD peak on bare gold. At this potential, in the absence of the thiol layer, a complete  $(\sqrt{3} \times \sqrt{3})R30^\circ$  honeycomb adlayer of Cu covers the electrode surface. In the presence of the thiol layer no complete Cu



Fig. 5.10 In-situ electrochemical STM image showing the 2D Cu island decoration on a decanethiol-covered Au(111) surface in the UPD potential range. Electrolyte: 50 mM  $\text{H}_2\text{SO}_4$  + 1 mM  $\text{CuSO}_4$ . Electrode potential: 50 mV vs.  $\text{Cu}/\text{Cu}^{++}$ . Tunneling parameters:  $I = 0.3$  nA,  $V = 0.1$  V.

monolayer develops and a distribution of Cu islands characterizes the electrode surface. Deposition proceeds via homogeneous nucleation of nanometer-sized islands on terraces, with no preferential growth occurring at steps. The STM image in Fig. 5.10 shows a typical fully developed Cu nanoparticle decoration. In Fig. 5.11, the nucleation kinetics has been followed in-situ. The STM sequence depicts a patch of clusters growing across the image field. In this sequence, the images are taken 49, 79, 96, and 130 min after the start of the polarization at +150 mV vs.  $\text{Cu}/\text{Cu}^{++}$ , which would correspond to the completion of the first adsorption peak on bare gold (cf. Fig. 5.3). The deposition appears as a slowly advancing front of a growing patch of islands, without apparent change in the clusters' positions or sizes once they are formed. Although the sequence in Fig. 5.11 is an example of what is typically

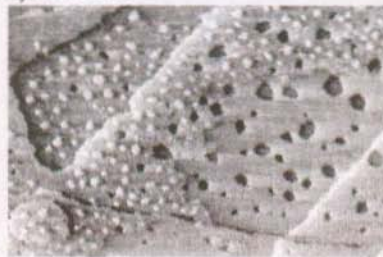
a) t=9 min



b) t=49 min



c) t=79 min



d) t=96 min



e) t=130 min



300Å

Fig. 5.11 In-situ electrochemical STM image sequence showing the development of the Cu island decoration on a decanethiol-covered Au(111) electrode. Electrolyte: 50 mM  $\text{H}_2\text{SO}_4$  + 1 mM  $\text{CuSO}_4$ . Electrode potential: 150 mV vs.  $\text{Cu}/\text{Cu}^{++}$ . Tunneling parameters:  $I = 0.6$  nA,  $V = 0.05$  V.

observed at the incipient phase of the deposition process with thiol layers present, the kinetics of the process depends on the potential. At more negative potentials the cluster decoration can develop more quickly. However, a threshold potential for the island deposition exists, as no cluster formation has ever been observed at potentials more positive than 200 mV.

When performing STM measurements in the electrochemical environment, one has to be aware that the STM tip could influence the electrochemical processes, in this case the electrodeposition, either by impeding the diffusion of ions or by influencing the electric field at the interface, a phenomenon already pointed out in electrochemical STM studies [Bre95, YLi95]. In order to check for such tip effects different areas of the surface a few millimeters apart have been sampled. What is found is that the cluster growth does not occur simultaneously all over the sample, but different regions are characterized by different stages in the cluster nucleation. However, no direct relation between growth stage and tip position has been observed. Random sampling over the electrode surface indicates that, after completion of the cluster decoration, both the size and spatial island distributions are virtually constant at all points. Another aspect to be mentioned is the fact that the spreading direction of the cluster patches (from the left to the right side in the sequence of images in Fig. 5.11) is not at all dependent on the scan direction. This is illustrated in the larger scan image of Fig. 5.12 which shows different cluster patches randomly distributed on the terraces.

Clusters preferentially grow on flat regions of the terraces, and almost always avoid steps or hole edges. Their formation proceeds in patches and it occurs abruptly in these patches. Once a threshold potential is surpassed, clusters nucleate at the advancing front of the patch and quickly attain their maximum size and spatial distribution in the UPD region. These remain fixed throughout the remainder of the UPD range and, depending on the thiol chain length (see next paragraph), also in the potential region of bulk deposition.

An analysis of the cluster size and density for the different chain lengths shows that they are independent of the thiol length. The graphs in Fig. 5.13 plot the average cluster area (a) and density (b) vs. the number of carbon atoms in the chain. Each point results from the average over five samples and error bars

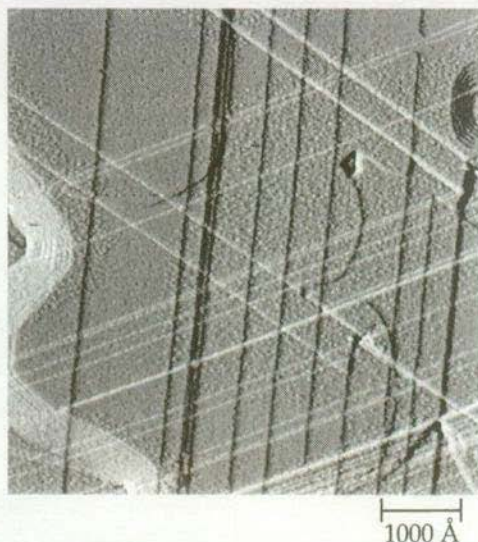


Fig. 5.12 In-situ electrochemical STM image showing different island patches randomly distributed on an octadecanethiol-covered Au(111) surface. Electrode potential: 100 mV vs. Cu/Cu<sup>++</sup>. Tunneling parameters:  $I = 0.3$  nA,  $V = 0.03$  V.

represent half of the difference between the maximum and the minimum of the obtained values. For each sample the island size and density have been measured in five different regions and then averaged. The plots show that the variations of the cluster area and density with the chain length are in the limit of the sample-to-sample variability. The average cluster area varies from 3 to 4 nm<sup>2</sup> while the density is about  $2 \times 10^{-2}$  clusters/nm<sup>2</sup>. Independent of coverage, the cluster height corresponds to the height of one monolayer of Cu.

It should be mentioned that Cu UPD onto octadecanethiol layers on Au(111) and subsequent ex-situ STM imaging of the deposits had been tried by Sun and Crooks [Sun91], but only as a means of imaging defects in *incomplete* thiol monolayers, assuming that UPD had taken place in pinholes and at other defect sites. In that study, the surface was pretreated by subjecting the thiol covered electrodes to large positive potential excursions in order to clean

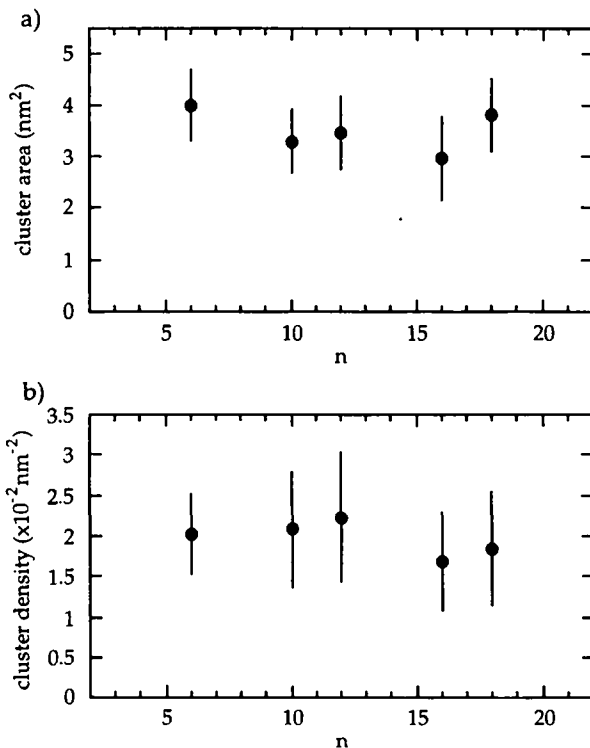


Fig. 5.13 Average Cu island area (a) and density (b) as a function of the number of C atoms in the alkyl chain.

supposed bare areas of the gold surface. It is known that such potential excursions can oxidatively desorb alkanethiols [Wid91B, Pan93]. In the present study, utmost care has been taken to leave the thiol layers intact avoiding any large excursion (i.e. above 500 mV vs.  $\text{Cu}/\text{Cu}^{++}$ ) of the electrode potential. The cyclic voltammogram in Fig. 5.9 for a decanethiol-covered electrode shows no peaks in the UPD region, thus the UPD deposition current is smaller than the double layer charging current (which is not the case for the pretreated

electrodes [Sun91]). In this work, the surface coverage of the clusters has been measured to be about 10-15%. If one would assume that 10-15% of the surface was exposed by pinholes, and that Cu deposited directly into the pinholes of the thiol layer, then peaks or plateaus should have been seen in the cyclic voltammogram, if the defect sites acted as ultramicroelectrodes [Cha93B]. For well formed layers, no peaks are seen. This leads to the conclusion that the deposition kinetics in the presence of a *complete* thiol monolayer must be too slow to permit observable currents to flow. From this evidence, as well as from the homogeneous nucleation observed by the STM, it is apparent that nanoparticles were not formed in pinholes or defects in the thiol layer. If, at first sight, the presence of the Cu islands could seem somehow surprising as no UPD peaks are seen in the cyclovoltammograms, one has to consider that, as shown by STM, Cu clusters exhibit a very slow growth kinetics (several tens of minutes are necessary to develop a full cluster decoration of the surface) which develops over a rather broad potential range. This behavior completely contrasts with the Cu UPD on bare gold which occurs abruptly in a narrow window of potential.

Before analyzing the evolution of the 2D Cu islands when the electrode potential is decreased in the OPD region, it is worthwhile to notice that the Cu islands prove to be tenacious and stable after emersion from the electrolyte. This results from emersion experiments performed in the following way: after the completion of the Cu island decoration, the samples were taken away from the electrolyte immediately after having switched off the potentiostatic control and then thoroughly rinsed with water. Subsequent STM imaging revealed that the Cu islands survive rinsing and are stable in air for at least a few days.

So far the electrodeposition of Cu on alkanethiol covered Au(111) electrodes in the underpotential regime has been discussed. This growth scenario (the instantaneous nucleation of patches of Cu nanoparticles spreading on the surface

until a full cluster decoration is achieved) characterizes the deposition process independently of the thiol chain length, from hexanethiol up to octadecanethiol.

## 5.5 Cu electrodeposition on alkanethiol/Au(111) in the overpotential regime

Although no dependence on the thiol chain length is observed in the UPD region, a different behavior is found when the electrode potential is decreased below the equilibrium Nernst potential.

The electrical blocking nature of self-assembled alkyl thiol layers on gold electrodes has been thoroughly investigated by electrochemical methods [Chi90, Por87, Son94A, Son95A]. From these studies, which used mainly indifferent electrolytes or redox couples (i.e.,  $\text{Ru}(\text{NH}_3)_6^{2+/3+}$ ,  $\text{Fe}(\text{CN})_6^{4-/3-}$ ,  $\text{Fe}(\text{H}_2\text{O})_6^{2+/3+}$ ) as probes to understand the blocking behavior, it has become clear that the blocking efficiency improves with alkyl chain length. The same chain length dependent response is observed for the Cu deposition process when the overpotential regime is explored. Again cyclic voltammetry and in-situ STM give complementary information to gain insight into the process. The dependence of the voltammetric behavior of thiol-covered Au(111) electrodes on the thiol chain length is illustrated in Fig. 5.14. Fig. 5.14a shows a current-voltage curve recorded on a hexanethiol-covered surface, while Fig. 5.14b refers to an octadecanethiol-covered electrode. As already discussed in reference to the CV for a decanethiol-covered electrode (see Fig. 5.9), the absence of the UPD peaks as well as the low electrochemical current reveal the blocking character of the organic layer. Now, the comparison of the two plots adds some new information: long chain monolayers block Cu deposition more efficiently



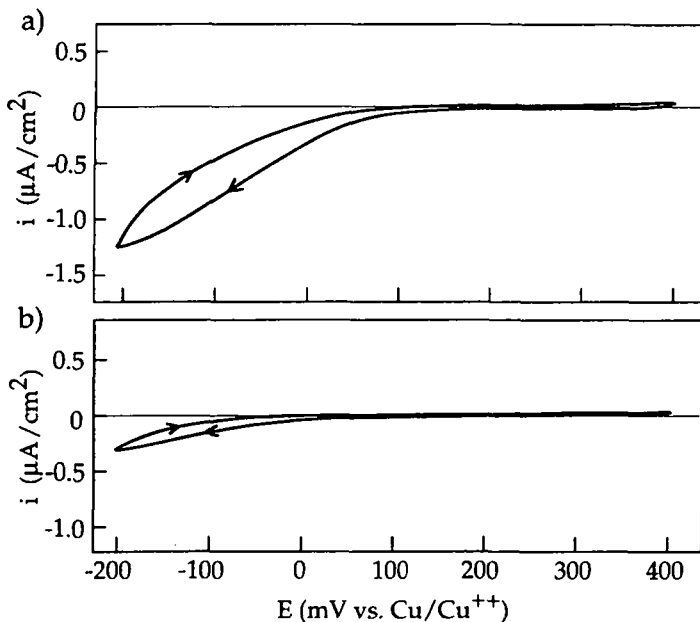


Fig. 5.14 Cyclic voltammograms for hexanethiol- (a) and octadecanethiol- (b) covered Au(111) showing the chain length dependent blocking behavior of thiol layers towards Cu deposition. Electrolyte: 50 mM  $\text{H}_2\text{SO}_4$  + 1 mM  $\text{CuSO}_4$ . Scan rate: 10 mV/s.

than short chain ones. This is the average trend resulting from the systematic analysis of many electrodes covered by different chain length thiols, but some variability from sample to sample has been observed also on electrodes covered with thiol layers of the same chain length (as reported also in [Son95B]).

The chain length dependent inhibitory behavior is revealed also by the STM measurements. In the overpotential range, the nanocluster morphology is stable on surfaces covered by long chain monolayers. An example is reported

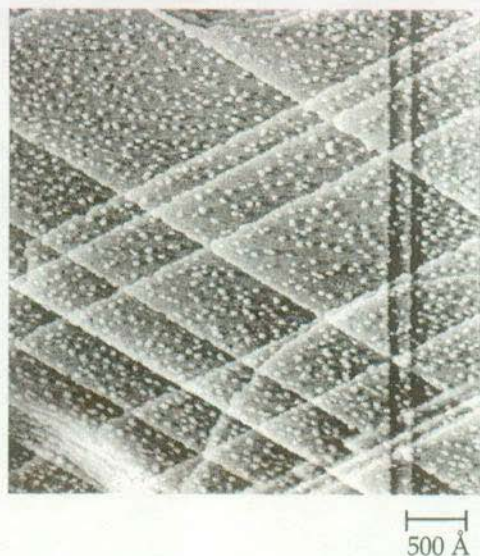
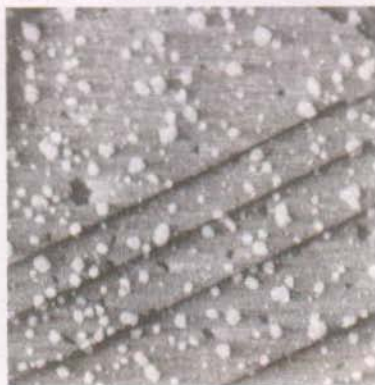


Fig. 5.15 In-situ electrochemical STM image showing no further change in the fully developed UPD cluster coverage on an octadecanethiol-covered Au(111) electrode after 3 hours of polarization at  $-150$  mV vs.  $\text{Cu}/\text{Cu}^{++}$ . Electrode potential:  $-150$  mV vs.  $\text{Cu}/\text{Cu}^{++}$ . Electrolyte:  $50$  mM  $\text{H}_2\text{SO}_4$  +  $1$  mM  $\text{CuSO}_4$ . Tunneling parameters:  $I = 0.3$  nA,  $V = 0.17$  V.

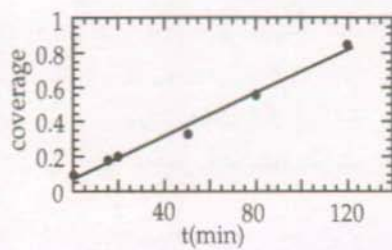
in Fig. 5.15 which shows an octadecanethiol-covered Au(111) surface after three hours of polarization at  $-150$  mV. The two-dimensional Cu clusters formed in the UPD regime are stable on the time scale of hours and no further deposition of Cu is observed. To see if this lack of growth was due to  $\text{Cu}^{++}$  diffusion inhibition caused by the close proximity of the STM tip to the surface, as has been reported in STM studies of Cu electrodeposition [Bit97, Bre95], various locations on the same sample separated by macroscopic distances were randomly sampled; this confirmed that indeed no overpotential deposition occurs anywhere on the electrode surface.

While for long chain monolayers ( $n > 13$ ) no further growth occurs even at potentials as negative as  $-200$  mV after the initial stage of UPD cluster

a)  $t=0$  minb)  $t=20$  minc)  $t=50$  mind)  $t=80$  mine)  $t=120$  min

400 Å

f)



formation, electrode surfaces covered by short chain monolayers ( $n \leq 12$ ) exhibit a two-dimensional layer growth in the OPD regime. As an example, Fig. 5.16 shows the time evolution of two-dimensional Cu growth on a hexanethiol layer while keeping the surface potential at  $-110$  mV vs.  $\text{Cu}/\text{Cu}^{++}$ . Cluster nucleation in the UPD region is the initial phase of Cu layer growth. At overpotentials essentially no further nuclei are formed but the existing Cu clusters grow laterally, i.e. the nucleation is instantaneous and not progressive. At this stage the island density is high enough that each Cu atom has sufficient mobility to reach existing islands with a higher probability than to meet a second mobile atom and to form a new nucleus [Bru94A]. As can be seen from the STM images island growth leads to ramification of the islands. In analogy to vapor phase epitaxial growth the "fractal" island shape can be ascribed to the low perimeter mobility for attaching atoms [Bru94B, Hwa91]. Upon further increase of the coverage, island coalescence sets in, finally completing the first monolayer. The formation of the second monolayer starts only when the first one is almost completed. Fig. 5.16f shows a plot of the coverage vs. time. This plot is linear, demonstrating that the electrodeposition flux was constant, and, based on a charge of  $0.44 \text{ mC}/\text{cm}^2$  for a full  $(1 \times 1)$  Cu monolayer on Au(111) [Hac91], equivalent to a deposition current of  $45 \text{ nA}/\text{cm}^2$ . The image in Fig. 5.17 was acquired after three hours of polarization at  $-110$  mV and shows the formation of the second monolayer, which again grows two-dimensionally. Some third layer islands, however, have nucleated on top of the second monolayer.

**Fig. 5.16** (a)-(e) In-situ electrochemical STM image sequence of Cu electrocrystallization on a hexanethiol-covered Au(111) electrode in the OPD regime. Electrode potential:  $-110$  mV vs.  $\text{Cu}/\text{Cu}^{++}$ . Electrolyte:  $50 \text{ mM H}_2\text{SO}_4 + 1 \text{ mM CuSO}_4$ . Tunneling parameters:  $I = 0.5 \text{ nA}$ ,  $V = 0.12 \text{ V}$ . (f) Plot of Cu coverage vs. time.

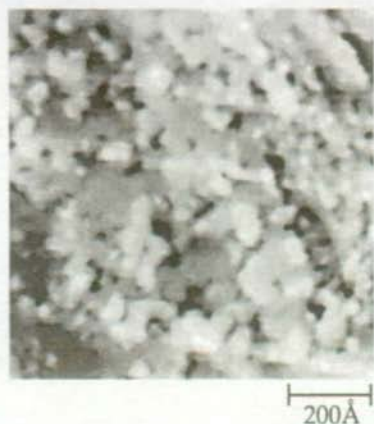


Fig. 5.17 In-situ electrochemical STM image depicting the multilayer coverage on a hexanethiol-covered Au(111) electrode after three hours of polarization at  $-110$  mV vs. Cu/Cu<sup>++</sup>. Electrolyte: 50 mM H<sub>2</sub>SO<sub>4</sub> + 1 mM CuSO<sub>4</sub>. Tunneling parameters:  $I = 0.5$  nA,  $V = 0.12$  V.

It is quite remarkable that the evolution of the Cu monolayer on the hexanethiol covered Au surface resembles very much the growth scenario of vapor phase epitaxy in the kinetic growth regime. Homogeneous nucleation followed by diffusion limited aggregation and coalescence is the well documented scenario for metal-on-metal growth at low temperatures [Bru94A, Bru94B, Hwa91, Ven84]. This electrocrystallization mechanism strongly contrasts with the usual behavior of Cu electrodeposition on bare Au(111) with the heterogeneous nucleation of large 3D clusters [Nic91]. For the alkanethiol covered gold surfaces 3D bulk copper nodules could be only occasionally deposited at potentials lower than  $-200$  mV. At these negative surface potentials the sudden growth of such nodules is possibly due to a breakdown of the thiol layer. In fact, CVs recorded on samples that have been subjected to prolonged polarization at these negative potentials usually show a degraded blocking property. A similar decrease of the blocking efficiency of thiol monolayers have been observed after cycling to very positive or negative potentials [Chi90, Mil91].

A situation similar to the deposition of bulk copper nodules has been found in the two other studies concerning Cu electrodeposition on thiol-covered electrodes that had been published prior to the present work. Those studies investigated the bulk deposition of Cu at very negative potentials, without analyzing the initial stage of the process in the UPD region and at moderate overpotentials. In the first work [Son95B], the presence of big hemispherical Cu nodules was observed by ex-situ scanning electron microscopy after polarization of the gold electrode at potentials well below the Nernst potential. In a recent work [Eli97], XPS and in-situ AFM have been used to study the morphology of the deposited Cu. In that study, however, Cu has been deposited galvanostatically which means that the deposition current and not the electrode potential has been fixed in each experiment. In this way bulk deposition of Cu was achieved, but during deposition potential excursions down to -700 mV vs. Cu/Cu<sup>2+</sup> have been recorded. Such negative excursions are capable of desorbing thiols [Pan93] and could thus have damaged the thiol layers.

On bare gold electrodes, overpotential (bulk) electrodeposition of Cu on Au(111) occurs by three-dimensional growth of islands on a UPD monolayer of Cu. Nucleation of 3D islands normally occurs at surface defects, such as step edges and kink sites of the UPD-Cu covered gold surface. The introduction of organic additives in the electrolyte can influence the deposition process. Studies of Cu electrodeposition in the presence of "levelers" such as crystal violet or other organic molecules [Nic92, Nic93] have shown that these additives favor Cu morphologies that are much smoother compared to those observed in the absence of additives. This "surfactant" effect has been tentatively attributed to the adsorption of the additives on the electrode surface and, in particular, to their preferential adsorption on top of the growing Cu crystallites which would block their vertical growth and promote their lateral

expansion. Another possible element favoring the smoother growth is the slower Cu growth rate. In those studies Cu clusters are still found to nucleate at substrate step edges and no additive effects in the UPD regime are detected. A situation much more resembling the one studied in this work has been found in the case of Cu deposition in a thiourea containing electrolyte [Höl95]. Thiourea adsorbs (with its S atom) more strongly to the gold surface preventing the full development of the UPD process and promoting the formation of 2D islands similar to the ones observed in the present study. But thiourea does not form a complete layer on the gold surface and peaks, even if small and broad, can still be observed in the UPD region of the cyclic voltammograms. A second difference compared to the alkanethiol covered electrodes is the Cu growth mode in the overpotential regime. In the presence of thiourea, UPD islands act as nucleation centers for the Cu deposition playing the role of gold step edges in additive free electrolytes, but no layer-by-layer growth is observed. Hence, even if thiourea influences the process by adsorbing on Au(111), its effect is not sufficiently strong to change the Cu growth mode from three-dimensional to almost two-dimensional.

To summarize, the chain length dependent blocking properties of alkanethiol SAMs have been exploited to control the growth mode of electrodeposited Cu in the OPD regime. In the case of short chain monolayers, UPD Cu islands act as aggregation centers for the further OPD Cu deposition which follows a layer-by-layer growth mode. On the other hand, long chain thiols block the process so efficiently that no further Cu deposition is observed in the OPD region (at least above -200mV). After polarization at potentials lower than -200 mV vs. Cu/Cu<sup>++</sup>, the growth of 3D Cu clusters can occur.

The next paragraph shows how a new control parameter, the temperature, can be introduced, even in the electrochemical environment, to modify the behavior of the system.

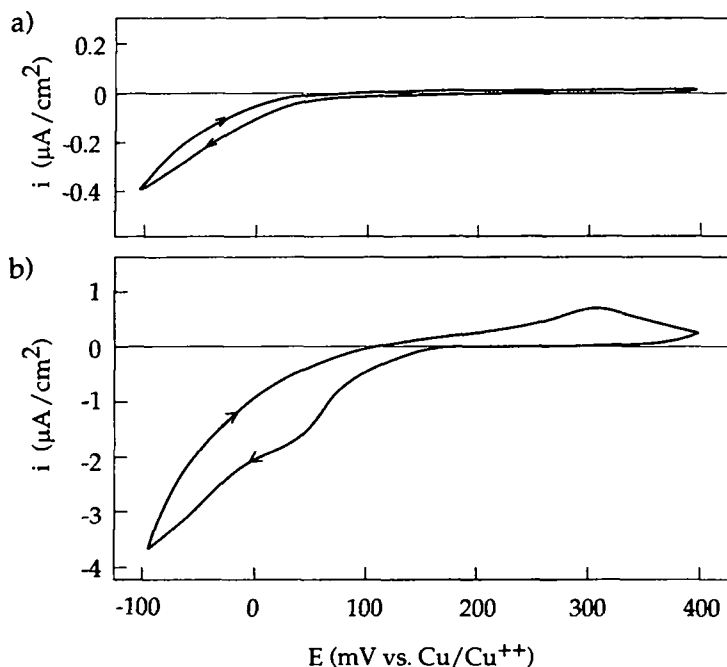
## 5.6 Cu electrodeposition at elevated temperature

As already mentioned before, in order to be able to perform isothermal STM measurement at elevated temperatures (up to 350 K) it has been necessary to use a non-standard electrolyte to prevent evaporation. As a consequence, a series of measurements have been performed at room temperature to look for eventual changes in the Cu electrodeposition process due to the new electrolyte. As discussed in paragraph 5.3 the use of ethylene glycol in the electrolyte does not influence the Cu/Au(111) system. Also the Cu deposition on alkanethiol covered Au(111) electrodes is found not to be affected by the introduction of ethylene glycol at room temperature. Measurements performed at room temperature in the new electrolyte with different chain length thiols showed that the usual 2D cluster growth is observed in the UPD region as well as the chain length dependent behavior (layer-by-layer growth for short chains and deposition suppression for long chains) in the OPD regime.

Now, increasing the temperature introduces some changes in the process. A first effect of temperature on the behavior of the system is revealed by cyclic voltammetry. Fig. 5.18 shows the current-potential curves for a decanethiol-covered Au(111) electrode at 300 K and 335 K. As can be easily inferred from the comparison of the two cycles, increasing the temperature somehow influences the system reducing the blocking properties of the thiol layer.

This first indication for a reduced blocking behavior is confirmed by the STM measurements. In the UPD region, the usual deposition of two dimensional clusters is observed, but at high temperatures (315-350 K) the process is faster and patches decorated with clusters now spread on the surface on the time scale of minutes rather than tens of minutes as observed at room temperature. But the major change induced by increasing the temperature occurs in the OPD region.

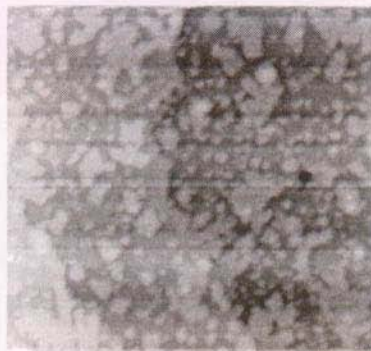
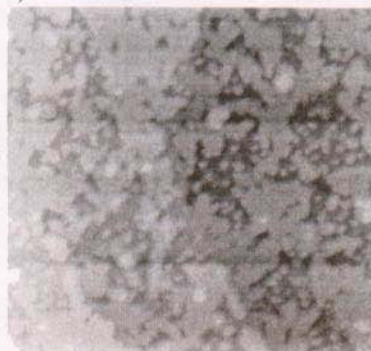
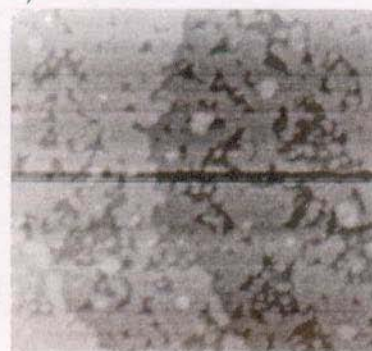
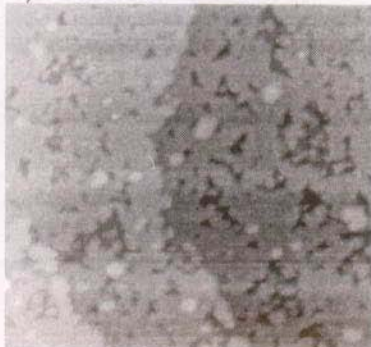
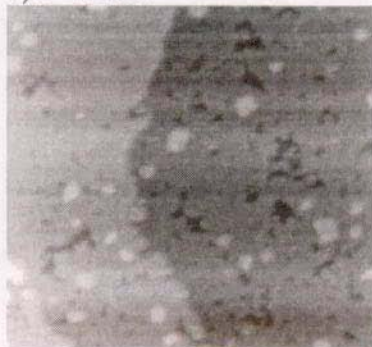




**Fig. 5.18** Cyclic voltammograms for a decanethiol-covered Au(111) at 300 K (a) and 335 K (b) showing the temperature dependent blocking behavior of thiol layers towards Cu deposition. Electrolyte: 50 mM  $\text{H}_2\text{SO}_4$  + 1 mM  $\text{CuSO}_4$  with the solvent being a 2:1 mixture of  $\text{HOCH}_2\text{CH}_2\text{OH} : \text{H}_2\text{O}$ . Scan rate: 10 mV/s.

Cu deposition is now greatly enhanced and a layer-by-layer growth is observed on *all* chain length thiols up to octadecanethiol. As observed on short chain monolayers at room temperature, two-dimensional Cu islands deposited in the UPD region act as aggregation centers for the further Cu deposition. An example of the multilayer growth of Cu on an octadecanethiol-covered Au(111) surface at 345 K is reported in Fig. 5.19.

**Fig. 5.19** In-situ electrochemical STM image sequence of Cu layer-by-layer growth on an octadecanethiol-covered Au(111) electrode at 345 K. Electrode potential: -50 mV vs.  $\text{Cu}/\text{Cu}^{++}$ . Electrolyte: 50 mM  $\text{H}_2\text{SO}_4$  + 1 mM  $\text{CuSO}_4$  with the solvent being a 2:1 mixture of  $\text{HOCH}_2\text{CH}_2\text{OH} : \text{H}_2\text{O}$ . Tunneling parameters:  $I = 0.7$  nA,  $V = 0.10$  V.

a)  $t = 30$  minb)  $t = 32$  minc)  $t = 34$  mind)  $t = 36$  mine)  $t = 38$  minf)  $t = 44$  minA horizontal scale bar with vertical end caps, indicating a length of 300 Å.

300 Å

The figure shows a sequence of images recorded 30, 32, 34, 36, 38 and 44 minutes after the beginning of the polarization at  $-50$  mV vs. Cu/Cu<sup>++</sup>. The sequence illustrates the aggregation and coalescence of Cu islands of the first layer as well as the completion of the layer and the nucleation of some second layer islands. The imaged region contains three different terraces of the gold substrate separated by monoatomic steps with the lower terrace occupying the right side of the image and the higher terrace occupying the lower left corner of the scanned area. In Fig. 5.19a several large first layer Cu islands resulting from coalescence as well as several still isolated clusters are visible. Coalescence develops through the sequence of images until an almost complete monolayer of Cu is deposited and some second layer islands nucleate (Fig. 5.19e,f). Cu growth is observed to proceed by the same two-dimensional mechanism for the next few layers.

Increasing the temperature not only promotes a multilayer Cu growth also on long chain thiols, but, as can be inferred from the comparison with the time scale of the layer-by-layer growth observed at room temperature on short chain monolayers (Fig. 5.16), the higher temperature enhances the deposition rate.

A second difference is observed in the overpotential necessary to achieve multilayer deposition. At room temperature potentials of about  $-100$  mV are necessary to start the aggregation and coalescence processes (at least to be able to observe them on the time scale of a few hours). At higher temperature these processes become operative already at potentials of about  $-50$  mV.

Different elements have to be taken into account in the analysis of the elevated temperature measurements. First, the increased surface mobility can affect the diffusion of Cu ions after their reduction to neutral adatoms influencing for instance the shape of the Cu islands. Cu islands grown above 320 K generally exhibit a more compact and round morphology which can be ascribed to an

enhanced perimeter mobility for attached atoms. A second phenomenon occurring at these temperatures is the increase of the mobility at the thiol/gold interface. As discussed in chapter 4, the interface undergoes a reorganization resulting in the healing of the vacancy island formed during the self-assembly. However, the process which has the main influence on the deposition rate is the temperature induced disorder in the alkanethiol chains. As already discussed in chapter 3, the disordering of the alkyl chains with increasing temperature is a well known phenomenon confirmed by experimental investigations as well as theoretical studies [Ulm91B]. Infrared spectroscopy measurements [Nuz90B] show that rising the temperature induces a decreasing and broadening of the peaks in the infrared spectra, ascribed to an increased population of gauche conformations, a similar behavior to that observed for crystalline alkanes prior to melting [Kim89]. Recently, chain melting proceeding from the exterior to the interior of the chain has been observed at about 320 K on self-assembled alkanethiol monolayers on gold nanoparticles [Bad97]. The same scenario of increasing disorder with increasing temperature results from molecular dynamics simulations [Bha97A, Hau90]. They suggest a transition from an orientationally ordered, low temperature state to a high temperature regime in which the molecular planes undergo reorientational motion associated with the appearance of gauche conformational defects.

Such disordered monolayers present a less efficient blocking behavior. This has been verified not only in the case of Cu deposition, but also by the use of a redox couple ( $\text{K}_3\text{Fe}(\text{CN})_6$ ) as a probe to monitor the charge transfer across the monolayer. Increasing the temperature induces a development of the redox reaction of the  $\text{Fe}(\text{CN})_6^{4-/3-}$  couple, normally hindered at room temperature. Fig. 5.20 reports cyclic voltammograms for a bare Au(111) electrode at room temperature (a), a hexadecanethiol-covered Au(111) surface at room temperature (b) and at 335 K (c) in 1 M KCl/1 mM  $\text{K}_3\text{Fe}(\text{CN})_6$ , with the solvent

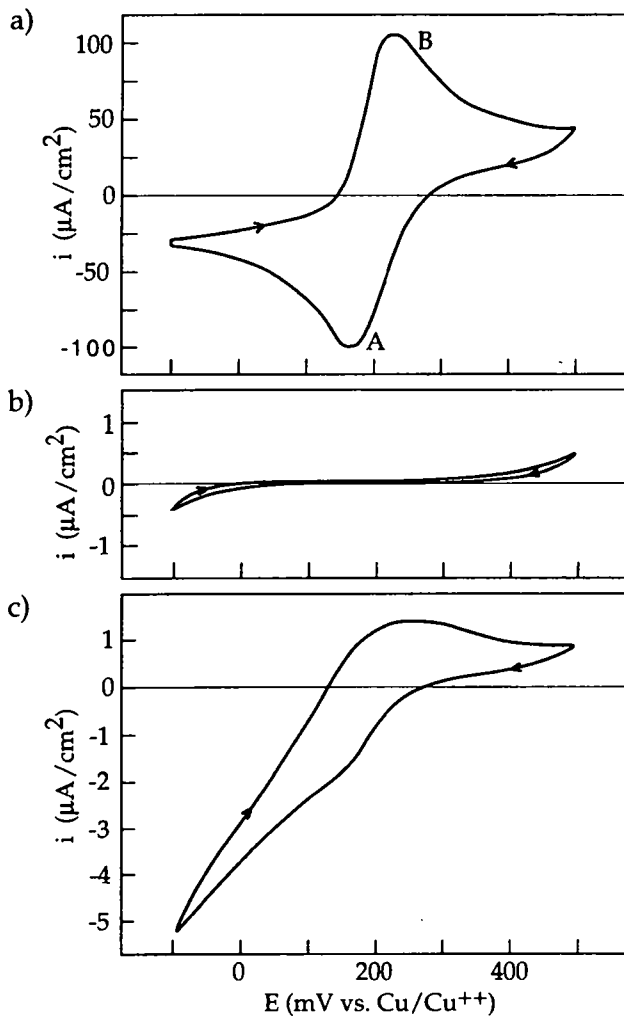


Fig. 5.20 Cyclic voltammograms for a Au(111) electrode at 300 K (a), for a hexadecanethiol-covered Au(111) electrode at 300 K (b) and at 335 K (c). Electrolyte: 1 M KCl + 1 mM  $\text{K}_3\text{Fe}(\text{CN})_6$  with the solvent being a 2:1 mixture of  $\text{HOCH}_2\text{CH}_2\text{OH} : \text{H}_2\text{O}$ . Scan rate: 50 mV/s. Potentials were measured vs. the Ag/AgCl electrode and are reported vs. a hypothetical  $\text{Cu}/\text{Cu}^{++}$  (1 mM) reference electrode for a simple comparison with the previously shown CVs.

being 1:2 water:ethylene glycol. The potential scan rate was 50 mV/s and potentials were measured vs. the Ag/AgCl electrode and are reported here vs. a hypothetical Cu/Cu<sup>++</sup> (1 mM) reference electrode to simplify the comparison with the previously shown CVs. In the case of bare gold, the usual reduction (A) and oxidation (B) peaks are visible which confirms once more that the use of ethylene glycol in the electrolyte does not introduce major changes in the behavior of the system. Pre-covering the electrode with a thiol layer (b) strongly reduces the electron transfer to the redox couple preventing the development of the redox peaks. The behavior of the hexadecanethiol-covered electrode changes when temperature increases. The curve in Fig. 5.20c shows some development of peaks at 335 K. Curves recorded at increasing temperature from 300 K up to 360 K indicate a continuous increase of the electrochemical current with the beginning of peak development at about 320 K. Upon cooling the sample, the peaks disappear, but currents higher than in (b) are measured. This deviation from reversibility is found to depend on individual samples with larger deviations observed for shorter chain monolayers. The presence of peaks at elevated temperatures can be interpreted in terms of the alkyl chain disorder which could allow an easier charge/discharge process of the redox couple through thermally induced defects in the monolayer (either because of an enhanced electron transfer or because of an increased ion permeability). An increase of the ion permeability due to the temperature-induced chain disorder has been advanced to explain the temperature-induced increase of the reduction current of [Fe(CN)<sub>6</sub>]<sup>3-</sup> measured at fixed overpotentials on gold electrodes covered by long chain thiol monolayers [Bad94].

A similar relationship between monolayer order and charge transfer to a redox couple has been observed on thiol covered gold electrodes that were incubated for different times in the thiol solution [Fru95]: short self-assembly times result

in full coverage, but poorly ordered films which do not block charge transfer efficiently and redox peaks are observed. Increasing the assembly time enhances the monolayer order resulting in well blocking layers which suppress the redox peaks.

## 5.7 Anodic Cu dissolution

So far, the different stages of Cu deposition on thiol-covered gold surfaces have been analyzed. The electrode polarization in the UPD region results in the deposition of two-dimensional Cu clusters, while polarizations in the OPD range induce, depending on thiol chain length and on temperature, a layer-by-layer Cu growth. At potentials lower than -200 mV the deposition of large three-dimensional Cu clusters can be observed.

Reversing the polarization of the electrode causes, as expected, the desorption of Cu. However, an interesting relationship between dissolution and deposition kinetics is found.

As previously discussed, 3D clusters can form at negative electrode potentials. When this 3D growth occurs, it is characterized by a relatively fast kinetics with Cu nodules a few hundreds of nanometers in size being deposited in a few minutes. An equally fast kinetics (well comparable to the copper deposition /dissolution on bare gold surfaces) characterizes the dissolution of these clusters at positive surface potentials.

On the other hand, two-dimensional Cu islands as well as layer-by-layer grown Cu films prove to have a more tenacious character and dissolve slowly with a rate comparable to their low deposition rate. In particular, Cu islands can withstand a few hours of polarization at +400 mV vs. Cu/Cu<sup>++</sup>. A general

trend which has been observed is that longer and/or lower cathodic polarizations result in a less facile dissolution of the 2D islands.

The relation between deposition and dissolution rate is confirmed by the measurements performed at elevated temperatures (320-350 K). As already mentioned in the previous paragraph, the deposition at higher temperature is faster compared to the deposition at room temperature. In a similar way, Cu dissolves more quickly at high than at room temperature.

In conclusion, the tenacious character of the Cu islands against anodic dissolution could suggest the occurrence of some passivation of the Cu islands (the inhibition of Cu corrosion due to a thiol layer has been reported in the case of thiol covered Cu surfaces in hydrochloric acid solution [Sch97]). On the basis of this observation and of the results presented in the previous paragraphs some mechanistic and structural models for the Cu/thiol/gold system will now be discussed.

## 5.8 Mechanistic and structural models

Cyclic voltammetry as well as in-situ STM show that self-assembled alkanethiol monolayers have a profound influence on the electrodeposition of Cu on Au and are able to modify the Cu growth mode. The 2D ramified Cu morphology is surprisingly similar to the diffusion limited aggregation patterns observed in molecular beam epitaxy in vacuum. An important factor allowing this growth mechanism to be operative is certainly the very slow growth kinetics on the alkanethiol modified electrodes. A second factor to be considered is the structural accommodation at the interface. A copper film growing pseudomorphically on the Au surface has a tensile strain of 13% as the Cu-Cu distance in bulk Cu is smaller than the Au-Au distance. It might be possible that the presence of the thiol layer permits the copper to grow close to



its natural lattice constant reducing Au-Cu misfit effects which would drive the system towards rough growth.

In the attempt to rationalize the behavior of the copper/thiol/gold system, different structural models of the interface can be envisaged. A first possibility, schematically shown in Fig. 5.21a, assumes the occurrence of a Cu electrocrystallization on top of the alkanethiol layer. The latter would act as a spacer layer through which electron tunneling must take place to pass charge across the interface with the electrolyte. In the second scenario (Fig. 5.21b), diffusion of Cu *through* the thiol layer - in the reduced or in a still partially ionized form with, eventually, a subsequent exchange between Au and Cu in the bond with the sulfur head group - would be the mechanism for a Cu electrocrystallization in contact with the gold surface. Finally, a third possibility (Fig. 5.21c) would explain the process in terms of an electrocrystallization of Cu on top of the thiol layer with Cu being in electrical contact with Au via some pinholes in the monolayers that would be filled with Cu.

As will result from the following discussion, an unequivocal model for the interfacial structure is difficult to propose.

A general consideration concerns the weak interaction between copper and a methyl group compared to the Cu-Cu one. As discussed at the beginning of this chapter, because of this weak interaction, a copper crystallization on top of the thiol layer should be characterized by a 3D growth mode.

Related to this consideration, an important element to be analyzed is the occurrence of Cu deposition in the UPD range. Metal UPD on bare metal surfaces is usually explained in terms of the high interaction between metal and substrate, an interaction even stronger than the metal-metal one. The weak interaction between Cu and methyl group (compared to the Cu-Cu one)

renders a UPD of Cu on top of the thiol layer difficult to explain. Hence, the occurrence of some contact between Cu and Au should be taken into account.

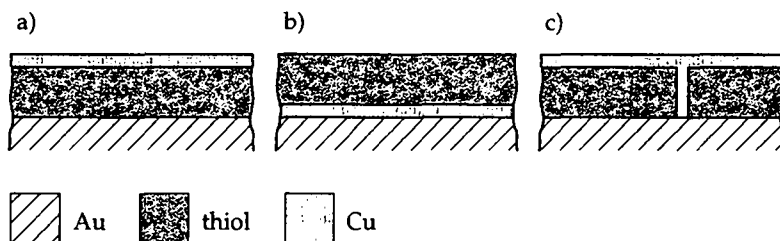


Fig. 5.21 Schematic representation of the possible structures of the Cu/thiol/gold interface.

One could assume a growth of UPD Cu islands occurring on top of the thiol layers, but in contact with the Au surface through some Cu "wires" (a situation similar to the model in Fig. 5.21c). This scenario, however, is ruled out by two observations. First, STM images the UPD clusters as monoatomic high islands. Even if one takes into account the possible ambiguities in the interpretation of the STM contrast when organic layers are present (see chapter 3), a T-shaped Cu cluster would surely not be imaged as a flat island of uniform height. Moreover, such UPD Cu clusters, exposed to the electrolyte and, at the same time, in electrical contact with the metal electrode would act as an extension of the electrode surface and would induce further Cu deposition in the OPD region (i.e. below 0 mV vs. Cu/Cu<sup>++</sup>) to form 3D clusters. This is not observed at least as long as the electrode potential is positive of -200 mV vs. Cu/Cu<sup>++</sup>. So the T-shaped model cannot explain the UPD Cu islands.

A more likely scenario to account for the deposition of Cu UPD islands is based on a possible Cu penetration through the thiol layer. The formation of a mixed layer of coadsorbed Cu atoms and thiol molecules at the gold surface or the

replacement of gold - thiol bonds with copper - thiol bonds can be envisaged (the formation of Cu thiolates has been reported in the case of thiol self-assembly on Cu [Kel94B]). It has to be mentioned that metal penetration into thiol self-assembled monolayers has been observed in vacuum in the case of evaporated metallic overlayers [Jun94, Jun96, Tar92]. The degree of metal penetration into the organic layer is found to depend on the thickness of the evaporated metal layer, on the strength of the interaction between the metal and the end group of the thiol chain and on temperature. Large amounts of deposited metal as well as weak interactions between metal and chain end group favor the penetration of metal in the layer. On the other side, decreasing the temperature prevents the penetration.

So far, the deposition of Cu islands in the UPD range has been discussed. From the arguments exposed above, penetration of Cu through the thiol layer would be the more likely mechanism to explain the formation of UPD islands.

Another important experimental observation to be discussed is the very slow growth kinetics that characterizes Cu deposition at potentials above -200 mV vs. Cu/Cu<sup>++</sup>. Different processes take part in the electrodeposition. First, Cu ions have to diffuse through the solution towards the surface to be reduced and deposited. An evaluation of the limitation of the Cu<sup>++</sup> reduction current due to Cu<sup>++</sup> diffusion can be obtained by the solution of the diffusion equation in the case of a planar electrode (Cottrell equation; [Bar80], p. 142). Under diffusion control, the current-time response following a step of the electrode potential decays with time as  $\alpha t^{-1/2}$ , where  $\alpha$  is a constant that depends on the diffusion coefficient, the solution concentration and the electrode area. In the experimental conditions used in this work, assuming a diffusion coefficient of  $5.7 \times 10^{-6} \text{ cm}^2/\text{s}$  [Tin68], the limiting current obtained under diffusion control would be two orders of magnitude larger than the measured current (even after one hour of polarization, a limiting current of about  $4 \mu\text{A}/\text{cm}^2$  is

calculated from the Cottrell equation while the current deduced from the STM images by the analysis of the Cu coverage vs. time is lower than  $50 \text{ nA/cm}^2$ ). Hence, ion diffusion through solution does not seem to be the rate-determining mechanism of the process.

In analogy to the treatment of  $\text{Cu}^{++}$  reduction on bare Au, a second step has to be considered: the ion reduction at the surface in the hypothesis of an unlimited number of ions available at the surface (i.e. without diffusional limitations). As a *lower limit* to this "pure reduction" current, one can consider the exchange current, i.e. the reduction and oxidation currents that pass through the interface at equilibrium and result in a net zero current. For the exchange current for  $\text{Cu}/\text{Cu}^{++}$  a value of  $500 \mu\text{A/cm}^2$  has been found [Dam66], again a limit much higher than the deposition currents measured in this work (one has to be aware that this value refers to a Cu surface in direct contact with  $\text{Cu}^{++}$  electrolyte).

In the case of thiol covered electrodes, the electron transfer to the Cu ions is likely to be a more complicated process. First of all, two possibilities can be envisaged: Cu ions, may be in a partially hydrated form, could diffuse through the layer (which is a process with a high activation energy because of the hydrophobic nature of the alkyl chains) and than be reduced at the gold surface, or electron transfer could occur through the layer with a Cu reduction at the thiol/solution interface. In the hypothesis of a Cu reduction on top of the thiol layer, electrons have to be transferred across the thiol layer. On the basis of the electron transfer rates through alkyl chains obtained from chronoamperometry studies on thiol SAMs functionalized with redox couples [Chi91A, Chi91B, Fin92], at the electrode potentials used in the present study, the charge necessary for the reduction of one monolayer of Cu would be transferred across the layer in several seconds, even in the case of the long

octadecanethiol molecule. This observation would suggest that the electron transfer through the thiol layer is not the limiting step of the deposition.

Some other processes should therefore be responsible for the slow deposition rate. As mentioned above, one possibility would be the occurrence of some penetration of Cu through the thiol layer. Diffusion of Cu through a well ordered thiol layer is likely to be a slow process, the slower the thicker and more compact the layer is. This could explain the slower kinetics observed in the case of longer thiols. Moreover, such a mechanism could also account for the higher deposition rate at elevated temperature. Less compact layers (due to chain tilt unlocking and higher population of *gauche* conformations, see chapter 3) are likely to offer a lower barrier to Cu penetration.

The slow anodic dissolution of Cu (deposited either in the UPD region or grown in a layer-by-layer mode in the OPD range) and the stability of the Cu islands upon exposure to atmospheric conditions could as well be explained by the occurrence of a Cu passivation due to a thiol encapsulation.

As already mentioned, together with the slow kinetics, a second element favoring a smooth growth can be identified in the release of Cu-Au lattice misfit strain due the presence of the thiol layer. A Cu film deposited on top of the "soft" thiol layer could grow close to its natural lattice without the tensile strain which characterizes a Cu layer growing pseudomorphically on Au. However, one can imagine that, even in the case of a Cu electrocrystallization below the thiol layer, the interaction with the surfactant thiol molecules should partially release the strain (note that thiols offer an effective way to release the strain of the reconstructed Au(111) surface, see chapter 3.2).

Different considerations apply to the Cu growth observed at potentials more negative than -200 mV. One could imagine a Cu growth occurring on top of the thiol layer, with a possible electrical contact with the metal electrode via defects

in the thiol layer caused by the polarization at negative potentials (a sort of "mushroom" structure). In this case the growing Cu would act as an extension of the electrode surface in direct contact with the electrolyte, which could explain the fast deposition and dissolution rates as well as the 3D growth mode (because of the high Cu-Cu interaction compared to the Cu-methyl one). Such a mechanism would be in agreement with the results of Eliadis et al. [Eli97] concerning the galvanostatic Cu deposition on thiol covered gold electrodes. By bulk deposition of Cu, accompanied by large negative potential excursions, they obtained a Cu growth shape which presents some similarities to the 3D clusters observed in the present study. In that work, XPS measurements showed an almost complete suppression of the sulfur signal after the Cu deposition, which was used to discard the model of thiol molecules behaving as surfactants sitting on top of the Cu deposit.

On the basis of the previous considerations an unambiguous scenario for the copper/thiol/gold interface is difficult to figure out. Some other investigation techniques could be advantageously employed to gain further insight into the process. X-ray reflectivity could be used to study in-situ the interfacial structure and should be able to give information about the relative position of Cu and thiol because of the different specular reflectivity curves obtained in the case of a) two metallic layers with high electronic density separated by a low electronic density film (the alkyl chains) or b) two adjacent metallic layers with the organic layer on top. However, care should be taken to avoid any damage of the thiol layer due to the beam exposure [Jäg97, JLi95]: the creation of defects in the monolayer would perturb the process enhancing Cu penetration into the layer. Other in-situ techniques which could be advantageously employed are sum frequency generation (SFG) or infrared spectroscopy (IR). By comparing the SFG and IR signals with and without Cu deposited on the thiol-covered electrode, information about the interfacial

structure could be obtained. In particular, the intensity and/or position of the peaks due to the  $\text{CH}_3$  vibrations are expected to be affected by the Cu deposition mainly if this happens on top of the thiol layer. Finally, X-ray photoelectron spectroscopy (XPS) could be used for the analysis, ex-situ, of the interface. Latest XPS measurements [Cav97] performed on octadecanethiol-covered electrodes after UPD deposition of Cu islands and subsequent water rinsing show a decrease of the Cu signal at grazing angle illumination (compared to normal illumination) which would suggest a copper penetration through the layer. Moreover, the comparison of the  $\text{CH}_3$  signal before and after the Cu deposition shows that it is almost unaffected by the presence of Cu.

## 5.9 Conclusions

Self-assembled alkanethiol monolayers have been used to prepare Au(111) electrodes modified with organic layers of controllable thickness. These monolayers exhibit a blocking behavior towards charge transfer which is found to depend on the molecule chain length as well as on temperature. These properties have been exploited to control the growth mode of Cu electrodeposited on these modified Au(111) electrodes. It has been shown how two-dimensional Cu islands, smooth layer-by-layer growth or three-dimensional Cu clusters can be achieved by controlling the chain length, the electrode potential and the temperature. An unequivocal model for the Cu/thiol/gold interface is difficult to propose, but Cu penetration through the thiol layer is likely to occur in the case of 2D islands as well as in the case of the layer-by-layer growth, while the subsequent 3D growth observed below  $-200$  mV (vs.  $\text{Cu}/\text{Cu}^{++}$ ) probably occurs at the thiol/electrolyte interface.

## Chapter 6

### Conclusion and outlook

The structure and the thermal stability of self-assembled alkanethiol monolayers (alkanethiol SAMs) on Au(111) have been investigated by variable temperature scanning tunneling microscopy (STM). The alkanethiol chemisorption results in the formation of ordered molecular domains characterized by different molecular patterns. These dense, well ordered monolayers can be used to modify the surface properties of the substrate.

In the present thesis, this opportunity has been exploited to control the electrochemical deposition of copper on thiol-modified gold electrodes. Varying the thickness of the organic layer, as well as the electrode potential and the temperature, allows to control the growth mode of the electrodeposited copper, as revealed by in-situ electrochemical STM.

The information obtained about the structure and properties of alkanethiol SAMs, the experience gained in using SAMs to prepare modified electrodes and in developing a variable temperature electrochemical STM represent a valuable base for the future development of this research. The next object of



investigation will concern the use of SAMs to control the deposition of magnetic nanostructures. The microcontact printing technique [Kum95] combined with the use of functionalized thiols is an interesting method to pattern the surface properties (like, e.g., hydrophilicity or chemical affinity) of thiol covered electrodes. Such patterned surfaces will be an interesting substrate for the selective deposition (by electrochemical as well as electroless deposition) of magnetic (e.g. cobalt or nickel) structures. In the framework of this project, a magneto-optical Kerr-effect measurement system allowing investigations in a liquid cell is under construction. In combination with STM, it will allow to obtain information about the structural and functional properties of the deposited thin magnetic films.

The idea behind this project is just one example of the many processes in which SAMs can be advantageously used to modify and control the properties of a surface. The design of chemical sensors and optoelectronic devices [Fuc91], the use of SAMs to prepare model systems for the study of cell membranes [Dus96] or to control the wettability and lubrication of a surface [McD97] are other examples of a fast developing interdisciplinary research area.

# Bibliography

- [And94] R. Andreu and W.R. Fawcett, *J. Phys. Chem.* **98** (1994), 12753
- [Ans93] D. Anselmetti, Ch. Gerber, B. Michel, H. Wolf, H.-J. Güntherodt, and H. Rohrer, *Europhys. Lett.* **23** (1993), 421
- [Ans94] D. Anselmetti, A. Baratoff, H.-J. Güntherodt, E. Delamarche, B. Michel, Ch. Gerber, H. Kang, H. Wolf, and H. Ringsdorf, *Europhys. Lett.* **27** (1994), 365
- [Bac93] C.E. Bach, R.J. Nichols, W. Beckmann, H. Meyer, A. Schulte, and J. Besenhard, *J. Electrochem. Soc.* **140** (1993), 1281
- [Bad94] A. Badia, R. Back, and R.B. Lennox, *Angew. Chem. Int. Ed. Engl.* **33** (1994), 2332
- [Bad97] A. Badia, L. Cuccia, L. Demers, F.G. Morin, R.B. Lennox, *J. Am. Chem. Soc.* **119** (1997), 2682
- [Bai89A] C.D. Bain, H.A. Biebuyck, and G.M. Whitesides, *Langmuir* **5** (1989), 723
- [Bai89B] C.D. Bain, E.B. Troughton, Y.-T. Tao, J. Evall, G.W. Whitesides, and R.G. Nuzzo, *J. Am. Chem. Soc.* **111** (1989), 321
- [Bar80] A.J. Bard and L.R. Faulkner, *Electrochemical Methods - Fundamentals and Applications*, John Wiley & Sons, New York (1980)
- [Bar90] J.V. Barth, H. Brune, G. Ertl, R.J. Behm, *Phys. Rev. B* **42** (1990), 9307

- [Bes87] K. Besocke, *Surf. Sci.* **181** (1987), 145
- [Bha97A] R. Bhatia and B.J. Garrison, *Langmuir* **13** (1997), 765
- [Bha97B] R. Bhatia and B.J. Garrison, *Langmuir* **13** (1997), 4038
- [Bie93] H.A. Biebuyck and G. Whitesides, *Langmuir* **9** (1993), 1766
- [Bin86] G. Binnig and D.P.E. Smith, *Rev. Sci. Instrum.* **57** (1986), 1688
- [Bit97] A.M. Bittner, J. Wintterlin, and G. Ertl, *Surf. Sci.* **376** (1997), 267
- [Boc70] J.O'M. Bockris and A.K.N. Reddy, *Modern Electrochemistry*, Plenum Press, New York (1970)
- [Bor94] G.L. Borges, K.K. Kanazawa, J.G. Gordon, K. Ashley, J. Richer, *J. Electroanal. Chem.* **364** (1994), 281
- [Bre95] N. Breuer, U. Stimming, and R. Vogel, *Electrochim. Acta* **40** (1995), 1401
- [Bru94A] H. Brune, H. Röder, C. Boragno, and K. Kern, *Phys. Rev. Lett.* **73** (1994), 1955
- [Bru94B] H. Brune, C. Romainczyk, H. Röder, and K. Kern, *Nature* **369** (1994), 469
- [Bry91] M.A. Bryant and J.E. Pemberton, *J. Am. Chem. Soc.* **113** (1991), 8284
- [Buc91] M. Buck, F. Eisert, J. Fischer, M. Grunze, and F. Träger, *Appl. Phys. A* **53** (1991), 552
- [Buc94A] J.-P. Bucher, L. Santesson, and K. Kern, *Langmuir* **10** (1994), 979
- [Buc94B] J.-P. Bucher, L. Santesson, and K. Kern, *Appl. Phys. A* **59** (1994), 135
- [Cam93A] N. Camillone, Ch.E.D. Chidsey, G.-Y. Liu, and G. Scoles, *J. Chem. Phys.* **98** (1993), 3503
- [Cam93B] N. Camillone, Ch.E.D. Chidsey, G.-Y. Liu, and G. Scoles, *J. Chem. Phys.* **98** (1993), 4234
- [Cam94] N. Camillone, P. Eisenberger, T.Y.B. Leung, P. Schwartz, G. Scoles, G.E. Poirier, M.J. Tarlov, *J. Chem. Phys.* **101** (1994), 11031
- [Cam96] N. Camillone, T.Y.B. Leung, P. Schwartz, P. Eisenberger, and G. Scoles, *Langmuir* **12** (1996), 2737

- [Cam97] N. Camillone, T.Y.B. Leung, G. Scoles, *Surf. Sci.* **373** (1997), 333
- [Cav97] O. Cavalleri, A.M. Bittner, T. Greber, H. Kind and K. Kern, *Z. Phys. Chem.*, submitted
- [Cha93A] O. Chailapakul, L. Sun, C. Xu, and R.M. Crooks, *J. Am. Chem. Soc.* **115** (1993), 12459
- [Cha93B] O. Chailapakul and R.M. Crooks, *Langmuir* **9** (1993), 884
- [Chi89] Ch.E.D. Chidsey, G.-Y. Liu, P. Rowntree, G. Scoles, *J. Chem. Phys.* **91** (1989), 4421
- [Chi90] Ch.E.D. Chidsey, D.N. Loiacono, *Langmuir* **6** (1990), 682
- [Chi91A] Ch.E.D. Chidsey, *Science* **251** (1991), 919
- [Chi91B] Ch.E.D. Chidsey, T.M. Putvinski, AT&T Bell Laboratories, Technical Memorandum, Document No. 11541-911120-85TM (1991)
- [Cop89] M. Copel, M.C. Reuter, E. Kaxiras, R.M. Tromp, *Phys. Rev. Lett.* **63** (1989), 632
- [Dam66] A. Damjanovic, T.H.V. Setty, and J.O'M. Bockris, *J. Electrochem. Soc.* **113** (1966), 429
- [Del94A] E. Delamarche, B. Michel, Ch. Gerber, D. Anselmetti, H.-J. Güntherodt, H. Wolf, H. Ringsdorf, *Langmuir* **10** (1994), 2869
- [Del94B] E. Delamarche, B. Michel, H. Kang, and Ch. Gerber, *Langmuir* **10** (1994), 4103
- [Del96] E. Delamarche, B. Michel, H.A. Biebuyck, and Ch. Gerber, *Adv. Mater.* **8** (1996), 719
- [Des83] A.R. Despic, in: *Comprehensive Treatise of Electrochemistry*, edited by B.E. Conway, J.O'M. Bockris, E. Yeager, R.E. White (Plenum Press, New York, 1983) vol. 7, p.451
- [Dis97] M.H. Dishner, J.C. Hemminger, and F.J. Feher, *Langmuir* **13** (1997), 2318
- [Dub92] L.H. Dubois, R.G. Nuzzo, *Annu. Rev. Phys. Chem.* **43** (1992), 437
- [Dub93] L.H. Dubois, B.-R. Zegarski, R.G. Nuzzo, *J. Chem. Phys.* **98** (1993), 678

- [Dür93] U. Dürig, O. Züger, B. Michel, L. Häussling, and H. Ringsdorf, *Phys. Rev. B* **48** (1993), 1711
- [Dus94] C. Duschl, M. Liley, G. Corradin, and H. Vogel, *Biophys. J.* **67** (1994), 1229
- [Dus96] C. Duschl, M. Liley, H. Lang, A. Ghandi, S.M. Zakeeruddin, H. Stahlberg, J. Dubochet, A. Nemetz, W. Knoll, H. Vogel, *Mater. Sci. Engin. C* **4** (1996), 7
- [Edi93] K. Edinger, A. Götzhäuser, K. Demota, Ch. Wöll, M. Grunze, *Langmuir* **9** (1993), 4
- [Eli97] E.D. Eliadis, R.G. Nuzzo, A.A. Gewirth, R.C. Alkire, *J. Electrochem. Soc.* **114** (1997), 96
- [Fen93] P. Fenter, P. Eisenberger, K.S. Liang, *Phys. Rev. Lett.* **70** (1993), 2447
- [Fen94] P. Fenter, A. Eberhardt, P. Eisenberger, *Science* **266** (1994), 1216
- [Fin92] H.O. Finklea and D.H. Hanshew, *J. Am. Chem. Soc.* **114** (1992), 3173
- [Fin96] H.O. Finklea, in: *Electroanalytical Chemistry*, edited by A.J. Bard and I. Rubinstein (Marcel Dekker, Inc. New York, 1996), vol. 19, p. 109
- [Fru95] Ch. Fruböse, Ph. D. Thesis, Freie Universität Berlin, Berlin 1995
- [Fuc91] H. Fuchs, *Adv. Mater.* **3** (1991), 10
- °[Gao93] X. Gao and M.J. Weaver, *J. Phys. Chem* **97** (1993), 8685
- [Gas96] B. Gasser, A. Menck, H. Brune, and K. Kern, *Rev. Sci. Instrum.* **67** (1996), 1925
- [Ger97] R. Gerlach, G. Polanski, and H.-G. Rubahn, *Appl. Phys. A* (1997), in press
- [Hac91] T. Hachiya, H. Honbo, and K. Itaya, *J. Electroanal. Chem.* **315** (1991), 275
- [Häh93] G. Hähner, Ch. Wöll, M. Buck, and M. Grunze, *Langmuir* **9** (1993), 1955
- [Hai94A] W. Haiss, Ph.D Thesis, Technischen Universität Berlin, Berlin 1994

- [Hai94B] W. Haiss, J.K. Sass, and M. van Heel, in: *Atomic Force Microscopy/Scanning Tunneling Microscopy*, edited by S.H. Cohen et al. (Plenum Press, New York,1994), p.423
- [Han94] T. Han and T.P. Beebe, *Langmuir* **10** (1994), 2705
- [Hau90] J. Hautman and M.L. Klein, *J. Chem. Phys.* **93** (1990), 7483
- [Hel79] H.L. von Helmholtz, *Ann. Phys. Chem. N.F.* **7** (1879), 337
- [Him97] H.-J. Himmel, Ch. Wöll, R. Gerlach, G. Polansky, and H.-G. Rubahn, *Langmuir* **13** (1997), 602
- [Höl94] M.H. Hölzle, U. Retter, and D.M. Kolb, *J. Electroanal. Chem.* **371** (1994), 101
- [Höl95] M.H. Hölzle, C.W. Apsel, T. Will, and D.M. Kolb, *J. Electrochem. Soc.* **142** (1995), 3741
- [Hwa91] R. Hwang, J. Schröder, C. Günther, and R.J. Behm, *Phys. Rev. Lett.* **67** (1991), 3279
- [Ish97] T. Ishida, S. Yamamoto, W. Mizutani, M. Motomatsu, H. Tokumoto, H. Hokari, H. Azehara, and M. Fujihira, *Langmuir* **13** (1997), 3261
- [Isr91] J.N. Israelachvili, *Intermolecular and Surface Forces*, 2nd ed. Academic Press, London (1991)
- [Jäg97] B. Jäger, H. Schürmann, H.U. Müller, H.-J. Himmel, M. Neumann, M. Grunze, and Ch. Wöll, *Z. Phys. Chem.* (1997), in press
- [JLi95] J. Li, K.S. Liang, G. Scoles, and A. Ulman, *Langmuir* **11** (1995), 4418
- [Jun94] D.R. Jung and A.W. Czanderna, *Crit. Rev. Solid State Mater. Sci.* **19** (1994), 1
- [Jun96] D.R. Jung, A.W. Czanderna, and G.C. Herdt, *J. Vac. Sci. Technol. A* **14** (1996), 1779
- [Kar94] D.S. Karpovich and G.J. Blanchard, *Langmuir* **10** (1994), 3315
- [Kel94A] G.L. Kellog, *Surf. Sci. Rep.* **21** (1994), 1
- [Kel94B] H. Keller, P. Simak, W. Schrepp, and J. Dembowski, *Thin Solid Films* **244** (1994), 799
- [Kim89] Y. Kim, H.L. Strauss, and R.G. Snyder, *J. Phys. Chem.* **93** (1989), 7520

- [Kim92] Y.-T. Kim, A.J. Bard, *Langmuir* **8** (1992), 1096
- [Kum95] A. Kumar, N.L. Abbott, E. Kim, H.A. Biebuyck, and G. Whitesides, *Acc. Chem. Res.* **28** (1995), 219
- [Lai91] P.E. Laibinis, G.M. Whitesides, D.L. Allara, Y.-T. Tao, A.N. Parikh, and R.G. Nuzzo, *J. Am. Chem. Soc.* **113** (1991), 7152
- [Lai92] P.E. Laibinis and G.M. Whitesides, *J. Am. Chem. Soc.* **114** (1992), 9022
- [Lar97] N.B. Larsen, H. Biebuyck, E. Delamarche, and B. Michel, *J. Am. Chem. Soc.* **119** (1997), 3017
- [Lee94] T.R. Lee, R.I. Carey, H.A. Biebuyck, and G.M. Whitesides, *Langmuir* **10** (1994), 741
- [Lif61] I.M. Lifshitz and V.V. Slyozov, *J. Phys. Chem. Solids* **19** (1961), 35
- [Mag91] O.M. Magnussen, J. Hotlos, G. Beitel, D.M. Kolb, R.J. Behm, *J. Vac. Sci. Technol. B* **9** (1991), 969
- [Mag93] O.M. Magnussen, Ph. D. Thesis, Universität Ulm, Ulm 1993
- [Mag96] O.M. Magnussen, B.M. Ocko, M. Deutsch, M.J. Regan, P.S. Pershan, D. Abernathy, G. Grübel, and J.-F. Legrand, *Nature* **383** (1996), 250
- [Man91] S. Manne, P.K. Hansma, J. Massie, V.B. Elings, A.A. Gewirth, *Science* **251** (1991), 183
- [Mar94] W. Mar and M.L. Klein, *Langmuir* **10** (1994), 188
- [McC93] R.L. McCarley, R.J. Dunaway, and R.J. Willicut, *Langmuir* **9** (1993), 2775
- [McD95] Ch.A. McDermott, M.T. McDermott, J.-B. Green, and M.D. Porter, *J. Phys. Chem.* **99** (1995), 13257
- [McD97] M.T. McDermott, J.-B.D. Green, and M.D. Porter, *Langmuir* **13** (1997), 2504
- [Mel88] O.R. Melroy, M.G. Samant, G.L. Borges, J.G. Gordon, L. Blum, J.H. White, M.J. Albarelli, M. McMillan, H.D. Abruña, *Langmuir* **4** (1988), 728
- [Mic91] T. Michely and G. Comsa, *Surf. Sci.* **256** (1991), 217
- [Mil91] C. Miller, P. Cuendet, and M. Grätzel, *J. Phys. Chem.* **95** (1991), 877

- [Möl95] F. Möller, O.M. Magnussen, and R.J. Behm, *Electrochim. Acta* **40** (1995), 1259
- [Nic91] R.J. Nichols, D.M. Kolb, R.J. Behm, *J. Electroanal. Chem.* **313** (1991), 109
- [Nic92] R.J. Nichols, W. Beckmann, H. Meyer, N. Batina, D.M. Kolb, *J. Electroanal. Chem.* **330** (1992), 381
- [Nic93] R.J. Nichols, C.E. Bach, and H. Meyer, *Ber. Bunsenges. Phys. Chem.* **97** (1993), 1012
- [Nuz87] R.G. Nuzzo, B.R. Zegarski, and H. Dubois, *J. Am. Chem. Soc.* **109** (1987), 733
- [Nuz90A] R.G. Nuzzo, L.H. Dubois, and D.L. Allara, *J. Am. Chem. Soc.* **112** (1990), 558
- [Nuz90B] R.G. Nuzzo, E.M. Korenic, and L.H. Dubois, *J. Chem. Phys.* **93** (1990), 767
- [Pan93] J. Pan, N. Tao and S.M. Lindsay, *Langmuir* **9** (1993), 1556
- [Pea92] D.R. Peale and B.H. Cooper, *J. Vac. Sci. Technol. A* **10** (1992), 2210
- [Fer67] J. Perdereau and G.E. Rhead, *Surf. Sci.* **7** (1967), 175
- [Pla93] A.L. Plant, *Langmuir* **9** (1993), 2764
- [Poi94A] G.E. Poirier and M.J. Tarlov, *Langmuir* **10** (1994), 2853
- [Poi94B] G.E. Poirier, M.J. Tarlov, and H.E. Rushmeier, *Langmuir* **10** (1994), 3383
- [Poi95] G.E. Poirier and M.J. Tarlov, *J. Phys. Chem.* **99** (1995), 10966
- [Poi96] G.E. Poirier and E.D. Pylant, *Science* **272** (1996), 1145
- [Poi97] G.E. Poirier, *Langmuir* **13** (1997), 2019
- [Por87] M.D. Porter, T.B. Bright, D.L. Allara, Ch.E.D. Chidsey, *J. Am. Chem. Soc.* **109** (1987), 3559
- [Reu] F. Reuse, private communication
- [Röd93] H. Röder, E. Hahn, H. Brune, J.P. Bucher, and K. Kern, *Nature* **366** (1993), 141



- [Röd94] H. Röder, Ph. D. Thesis, EPFL, Lausanne 1994
- [Ros] G. Rosenfeld, private communication
- [Ros95] G. Rosenfeld, N. Lipkin, W. Wulfhekel, J. Kliewer, K. Morgenstern, B. Poelsema, and G. Comsa, *Appl. Phys. A* **61** (1995), 455
- [Sch95] C. Schönenberger, J. Jorritsma, J.A.M. Sondag-Huethorst, and L.G.J. Fokkink, *J. Phys. Chem.* **99** (1995), 3259
- [Sch97] J. Scherer, M.R. Vogt, O.M. Magnussen, and R.J. Behm, submitted to *Langmuir*
- [Sie93] J.I. Siepmann and I.R. McDonald, *Phys. Rev. Lett* **70** (1993), 453
- [Son94A] J.A.M. Sondag-Huethorst and L.G.J. Fokkink, *J. Electroanal. Chem.* **367** (1994), 49
- [Son94B] J.A.M. Sondag-Huethorst, C. Schönenberger, and L.G.J. Fokkink, *J. Chem. Phys.* **98** (1994), 6826
- [Son95A] J.A.M. Sondag-Huethorst and L.G.J. Fokkink, *Langmuir* **11** (1995), 2237
- [Son95B] J.A.M. Sondag-Huethorst and L.G.J. Fokkink, *Langmuir* **11** (1995), 4823
- [Spi93] J. Spinke, M. Liley, H.-J. Guder, L. Angermaier, and Knoll, *Langmuir* **9** (1993), 1821
- [Str93] L. Strong, M. Whitesides, *Langmuir* **9** (1993), 1955
- [Str94] S.J. Stranick, M.M. Kamna, K.R. Krom, A.N. Parikh, D.L. Allara, and P.S. Weiss, *J. Vac. Sci. Technol. B* **12** (1994), 2004
- [Sun91] L. Sun and R. M. Crooks, *J. Electrochem. Soc.* **138** (1991), L23
- [Tak95] T. Takami, E. Delamarche, B. Michel, Ch. Gerber, H. Wolf, and H. Ringsdorf, *Langmuir* **11** (1995), 3876
- [Tar92] M.J. Tarlov, *Langmuir* **8** (1992), 80
- [Tin68] C.W. Tindall and S. Bruckenstein, *Anal. Chem.* **40** (1968), 1402
- [Ton95] M.F. Toney, J.N. Howard, J. Richer, G.L. Borges, J.G. Gordon, O.R. Melroy, D. Yee, L.B. Sorensen, *Phys. Rev. Lett.* **75** (1995), 4472

- [Tre89] D.J. Trevor, Ch.E.D. Chidsey, D. N. Loiacono, *Phys. Rev. Lett.* **62** (1989), 929
- [Ulm91A] A. Ulman, *An introduction to ultrathin organic films*, Academic Press, San Diego (1991)
- [Ulm91B] A. Ulman, *Adv. Mater.* **3** (1991), 298
- [Ven84] J.A. Venables, G.D.T. Spiller, and M. Hanbücken, *Rep. Prog. Phys.* **47** (1984), 399
- [Wag61] C. Wagner, *Z. Elektrochem.* **65** (1961), 581
- [Wid91A] C.A. Widrig, C.A. Alves, M.D. Porter, *J. Am. Chem. Soc.* **113** (1991), 2805
- [Wid91B] C.A. Widrig, C. Chung, M.D. Porter, *J. Electroanal. Chem.* **310** (1991), 335
- [Wil95] R.J. Willicut and R.L. McCarley, *Langmuir* **11** (1995), 296
- [Wyn75] P. Wynblatt and N.A. Gjostein, in: *Progress in Solid State Chemistry*, edited by J.O. McCaldin and G. Somorjai (Pergamon, Oxford, 1975), vol.9, p.21
- [Yeg95] M.S. Yeganeh, S.M. Dougal, R.S. Polizzotti, P. Rabinowitz, *Phys. Rev. Lett.* **74** (1995), 1811
- [YLi95] Y.-Q. Li, O. Chailapakul, R.M. Crooks, *J. Vac. Sci. Technol. B* **13** (1995), 1300
- [Zak93] J. Zak, H. Yuan, M. Ho, L.K. Woo, and M.D. Porter, *Langmuir* **9** (1993), 2772
- [Zin92] M. Zinke-Allmang, L.C. Feldman, and M.H. Grabow, *Surf. Sci. Rep.* **16** (1992), 377
- [Zub95] Ch. Zubrängel, C. Deuper, F. Schneider, M. Neumann, M. Grunze, A. Schertel, Ch. Wöll, *Chem. Phys. Lett.* **238** (1995), 308

## Publications

The research performed during this thesis led to the following publications:

- [1] O. Cavalleri, A. Hirstein, and K. Kern, "Ostwald ripening of vacancy islands at thiol covered Au(111)", *Surf. Sci.* **340** (1995) L960
- [2] O. Cavalleri, A. Hirstein, J.P. Bucher, and K. Kern, "Ordering processes at the decanethiol/Au(111) interface", *Thin Solid Films* **284-285** (1996) 392
- [3] S.E. Gilbert, O. Cavalleri, and K. Kern, "Electrodeposition of Cu-nanoparticles on decanethiol covered Au(111) surfaces - An in-situ STM investigation", *J. Phys. Chem.* **100** (1996) 12123
- [4] A. Hirstein, O. Cavalleri, J.P. Bucher, and K. Kern, "Interfacial ordering of self-assembled thiol monolayers on Au(111)", in: 6th European Conference on Applications of Surface and Interface Analysis (Montreux, Suisse, 1995), edited by H.J. Mathieu, B. Reihl and D. Briggs (Wiley, Chichester, 1996)
- [5] O. Cavalleri, S.E. Gilbert, and K. Kern, "Electrochemical Cu deposition on thiol covered Au(111) surfaces", *Surf. Sci.* **377-379** (1997) 931
- [6] O. Cavalleri, S.E. Gilbert, and K. Kern, "Growth manipulation in electrodeposition with self-assembled monolayers", *Chem Phys. Lett.* **269** (1997) 479
- [7] O. Cavalleri, H. Kind, A.M. Bittner, and K. Kern, "Thiolate layers in electrolytes at elevated temperature", submitted to *Langmuir*
- [8] O. Cavalleri, A.M. Bittner, T. Greber, H. Kind and K. Kern, "Copper electrodeposition on alkanethiolate layers", submitted to *Z. Phys. Chem.*

# Merci!

J'aimerais remercier en premier lieu le professeur Klaus Kern, mon directeur de thèse, pour m'avoir donné l'opportunité de réaliser ce travail en m'accueillant dans son groupe et pour son soutien pendant toute cette période.

J'aimerais ensuite remercier tous ceux qui, au cours de ces trois années, ont fait partie de l'équipe "STM à pression ambiante":

Andreas Hirstein pour avoir activement contribué à la première phase de ce travail en réalisant une partie des mesures sur les thiols "à l'air",

Scott Gilbert, pour m'avoir initiée à l'électrochimie et pour son aide et son encouragement pendant la période difficile de la mise au point du STM électrochimique,

Alexander Bittner, pour m'avoir beaucoup aidée, surtout pendant la rédaction de ce manuscrit, avec ses idées, ses conseils et ses critiques constructives,

Hannes Kind et Manuel Lonfat pour leur collaboration amicale.

Je voudrais également remercier:

François Reuse, qui à effectué les calculs de la densité électronique des thiols, pour sa gentillesse et sa disponibilité,

tous les membres des ateliers mécanique et électronique pour leur précieuse collaboration ainsi que Claire-Lise Bandelier qui a réalisé la plus part des figures de ce manuscrit,

les francophones du groupe pour avoir toujours répondu à mes questions linguistiques sans jamais s'énerver,

tous, enfin, à l'Institut de Physique Expérimentale, pour l'atmosphère amicale qui y regne.

Mes remerciements vont aussi à l'Université de Gênes et à la "Fondation pour des Bourses d'Etudes Italo-Suisses" de Lausanne pour leur soutien financier.

Ed infine un grazie grande grande a coloro che mi stanno piu' a cuore e che mi hanno sempre sostenuto, incoraggiato ( e sopportato) anche durante i periodi piu' difficili.

## Curriculum vitae

Name: Ornella Cavalleri

Date of birth: 20.08.1967 in Alassio (SV), Italy

1973-1978 Primary school in Albenga (SV), Italy

1978-1986 Secondary school in Albenga

1986-1991 Studies in Physics at the University of Genoa

1992 Diploma thesis:  
"Struttura molecolare di films organici rivelata mediante  
microscopia a sonda di scansione"  
(Molecular structure of organic films studied by scanning  
probe microscopy)  
performed in the Laboratory of Biophysics (Prof. A. Gliozzi)  
of the Department of Physics, University of Genoa

1993 Grant for post-graduate student at the Laboratory of  
Biophysics, Physics Department, University of Genoa

since 1994 Ph.D. student at the Ecole Polytechnique Fédérale de  
Lausanne, Institute of Experimental Physics, Prof. K. Kern